Optical Fiber Grating based Sensors

Michelsen, Susanne

Publication date:
2003

Document Version
Publisher's PDF, also known as Version of record

Optical fiber grating based sensors

Susanne Michelsen

Danish Institute of Fundamental Metrology
Research center COM, Technical University of Denmark
and
Koheras

Ph.D. Thesis, January 2003

Abstract

In this thesis different optical fiber gratings are used for sensor purposes.

If a fiber with a core concentricity error (CCE) is used, a directional dependent bend sensor can be produced. The CCE direction can be determined by means of diffraction. This makes it possible to produce long-period gratings in a fiber with a CCE direction parallel or perpendicular to the writing direction. The maximal bending sensitivity is independent on the writing direction, but the detailed bending response is different in the two cases.

A temperature and strain sensor, based on a long-period grating and two sampled gratings, was produced and investigated. It is based on the different temperature and strain response of these gratings. Both a transfer matrix method and an overlap calculation is performed to explain the sensor response.

Another type of sensor is based on tuning and modulation of a laser wavelength. It is shown that it is possible to tune and modulate a DFB fiber laser with both strain from a piezoelectric transducer, and by temperature through resistive heating of a metal film. Both a chemical deposited silver layer and an electron-beam evaporation technique has been investigated, to find the most reproducible method. Such a laser can be applied for gas monitoring and it can be stabilized by locking it to an absorption line. The locked laser has a stability of ~ 2 MHz, which makes it suitable as a wavelength standard in the 1.5 μm telecommunication band.

Resume

I denne Ph.D. afhandling har forskellige gitre i optiske fiber været brugt til sensor formål.

Hvis en fiber med en kerneforskydning anvendes, kan en retningsbestemt bøjningssensor produceres. Retningen af kerneforskydningen kan bestemmes ved hjælp af diffraktion. Det er derfor muligt at skrive langperiodiske gitre i fiber med kerneforskydningen parallel eller vinkelret på UV-strålen. Det maksimale bøjningsrespons er uafhængig af skriveretningen, men det totale bøjningsrespons er forskelligt i de to tilfælde.

En temperatur- og stræk-sensor, baseret på et langperiodisk gitter og to samplede gitre, blev produceret og undersøgt. Sensoren er baseret på de forskellige temperatur og stræk koefficienter for de to typer af gitre. Udregninger ved brug af overførsels-matricer og udregninger af overlappet mellem to reflektions spektra er udført for at forklare de målte data.

En anden type af sensore er baseret på tuning og modulation af laser-bølgelængden. Det er vist, at det er muligt at tune og modulere bølgelængden af en DFB fiber laser både via stræk fra en piezo og temperaturændringer via opvarmning af et metallag på fiberlaseren. For at finde den mest optimale metode til at producere et metallag er både kemisk udfældning af sølv og elektronstråle pådampning undersøgt. Sådan en laser kan anvendes til gas målinger, og den kan låses til en absorptionsline. En låst fiber laser har en stabilitet på $\sim$ 2 MHz, hvilket gør den anvendelig som bølgelængdenormal i 1.5 μm telekommunikationsområdet.

Acknowledgements

This industrial Ph.D. project has been a cooperation between the Danish Institute of Fundamental Metrology, research center COM and Koheras. It has been supported by the Danish Academy of Technical Sciences (ATV).

I would like to thank my supervisors, Jes Henningsen and Martin Kristensen for their help and encouragement during my PhD. work.

I would also like to thank Jens Engholm Pedersen, Poul Varming and their colleges at Koheras for their support and help to my project. Without this fruitful collaboration about the fiber lasers I would not have reached my goal of temperature modulation of the fiber lasers.

A special thanks goes to OFS Fitel Denmark (former Lucent) for supply of optical fibers for the experiments.

Furthermore for inspiration, practical help and good company I would like to thank all my colleges at DFM and at COM especially: Peter Borel, Maria Holmberg, Niels Kofod, Carl Johan Markmann, Jacob Rathje, Valentina Russova, Rune Shim and Henrik Rokkjær Sørensen.

Last but not least I want to thank Kåre Michelsen and my family for their support.

Contents

Chapter 1

Introduction

In the last decade there has been a dramatic development of optical fiber technology and laser technology in the telecommunication ranges 1.3 μm and 1.5 μm. This development has been driven by the desire of higher bandwidths. A spinoff is components, which can also be used for sensor purposes. It is especially the environmental, medical and the industrial sectors, which have a requirement for measuring physical parameters.

Optical fibers have the advantage over electrically based sensors, that they can be applied where there are risks of explosion or fire. They are very compact and flexible, and it is possible to produce sensors in materials which can stand high temperatures and are resistant to most chemicals.

One type of sensors is based on gratings in optical fibers. These gratings can be divided into two types, the active (i.e. fiber lasers) and the passive components. The passive components have two categories. The short period gratings with a period of the order of 1 μm (which have narrow reflection bands with high-resolution), and the long-period gratings with a period of the order of 100 μm. The last type of gratings couples light to the cladding modes. For telecommunication purposes the long-period gratings are used for gain flattening filters in erbium doped amplifiers [1]. A long-period grating can be used as a chemical sensor, since the resonance wavelengths depend on the refractive index in the cladding and in the surroundings [2].

When a long-period grating is bent the wavelength resonances split into two modes [3, 4, 5, 6]. Patrick *et al* observed an asymmetry when the long-period grating was bent in opposite directions [3]. From this effect a directional bending sensor was constructed [4] based on two gratings with opposite orientation. If the fiber has a core concentricity error the wavelength resonance is split without being bent. This effect has been

used for a direction dependent bend sensor [7, 8], since the splitting either increases or decreases depending on the direction of the bend.

The resonance wavelength of a long-period grating shifts when the temperature is changed. If the refractive index of the cladding is chosen correct, it is possible to produce a temperature insensitive long-period grating [9]. Bhatia *et al* [10] showed that it is possible to produce a temperature insensitive and a strain insensitive long-period grating sensor in a Corning flexcore fiber. In this case they chose the period long, so the material response and the wavelength response cancelled each other, and made the sensor strain insensitive. When a flexcore fiber is used, the temperature sensitivity is low, this gives a temperature insensitive sensor. Others have based a sensor on both a Bragg grating and a long-period grating, where the temperature response is measured with a detector [11]. Zhao and Claus [12] used a Bragg grating to demodulate the long-period grating response of temperature and strain. Fallon *et al* [13] used a Bragg grating as a sensor and a long-period grating to interrogate the result, where the input signal was modulated and the output detected by a lock-in amplifier. These methods all rely on the power reflected from a Bragg grating.

Different sensors have been produced by combining the behavior of a Bragg grating and a long-period grating into a superstructure grating [14, 15, 16]. They all used an optical spectrum analyzer to resolve the change.

Fiber lasers belong to the active component group. There are different types of fiber lasers. The ring laser configuration [17, 18] has a fiber beam splitter as output coupler, and a long erbium doped fiber as active medium[1]. Due to the temperature sensitivity of a long cavity, it is necessary with active stabilization to achieve single-mode operation. Another type of fiber laser is based on Bragg gratings as cavity mirrors [20, 21, 22]. This type of laser is not single-mode, but a distributed feedback (DFB) laser can become single-mode [23, 24], if a $\pi/2$ phase shift is introduced in the center of the grating. To enhance the output power of the fiber laser the core can be co-doped with ytterbium [25]. It is not possible to have both ytterbium and germanium in the core since the efficiency will decrease. Dong *et al* [26, 27] showed that it is possible to make a photosensitive ring with germanium and boron around the core, and produce a fiber laser.

When the reflection from a Bragg grating is used in a sensor, only a small amount of power is detected, due to the narrow reflection band. To enhance the detected power a fiber laser can be used as sensor. When the grating

[1] Other dopants can be used if another wavelength range is needed. A thulium doped fiber can emit light at a wavelength of 2.31 μm [19].

in the laser is influenced by for example temperature or strain, the output wavelength will change. The wavelength is therefore a direct measure of the change. If a DFB fiber laser emits light in both polarizations, the beat frequency between these and the change in wavelength can be measured, to detect changes in temperature and strain [28] or pressure and force [29]. A DFB fiber laser can also be used as an acoustic sensor in air [30].

A DFB fiber laser can be used as indirect sensor, where the light from the laser is used for measurements. The spectral width of a fiber laser is typically less than about 15 kHz [31, 32], and it is thus potentially useful for applications such as high-resolution spectroscopy or interferometry. In modulation spectroscopy, the sensitivity is enhanced by using synchronous detection of the first or second harmonic of the applied modulation frequency. If the laser is used for gas sensing this leads to a significant improvement of the detection limit. Another application is to use the first derivative response of the harmonic modulation as the error signal needed for locking the laser to a molecular absorption line. Such a scheme can be used for absolute wavelength standards needed in communication networks, where strict control of the optical wavelength is necessary.

Semiconductor lasers can be wavelength modulated up to the GHz range through the injection current. For an extended cavity laser, where the wavelength is controlled by the cavity length, wavelength modulation up to 1 kHz is feasible if the grating or an auxiliary mirror is mounted on a piezoelectric transducer. Tuning of a fiber laser can be done by strain [33], compression [34] or temperature. It has been demonstrated by Pan *et al*[35], that if the DFB fiber laser is mounted in a teflon block, it can be tuned 11 nm via the large temperature coefficient of teflon. To use the fiber laser for high-resolution molecular spectroscopy, it is necessary to modulate the wavelength besides tuning it. DFB fiber lasers do not have a built in way to be modulated. There are two possibilities, either strain modulation with a piezoelectric transducer or temperature modulation. If the laser is mounted in a block the temperature variation is very slow. Limberger *et al* [36] showed that it is possible to adjust or modify a grating by resistive heating of a thin film deposited on the fiber.

Another application of a laser which can be tuned and modulated is for a wavelength standard in the 1.5 μm telecommunication band. The advantage of a fiber laser is low cost when special wavelengths are needed.

The content of this thesis is as follows. In chapter 2 a short description of the theory of Bragg gratings and sampled gratings, and a description of DFB fiber lasers and long-period gratings is provided.

The work this thesis is based on can be divided into two parts. The first part is about applying passive gratings for sensor purposes. In chapter 3 a long-period grating in a fiber with a core concentricity error is investigated with regards to directional bending. In chapter 4 one long-period grating and two sampled gratings are used for a temperature and strain sensor.

In the second part of the thesis DFB fiber lasers are used for gas monitoring. An introduction to absorption spectroscopy, frequency modulation and selection rules for infrared spectroscopy of combination bands is given in chapter 5. To improve the signal to noise ratio, synchronous detection can be applied. This demands a possibility of tuning and modulating the wavelength. Tuning and modulation of a fiber laser has been implemented by straining the fiber with a piezoelectric transducer [37] as illustrated in chapter 6. A laser, which can be tuned and modulated, can also be stabilized and used as a wavelength standard. The stability can be investigated by use of an Allan variance. In chapter 7 a DFB fiber laser with a metal coating is investigated. Both chemically deposited silver and electron-beam evaporated gold are studied to find the best method for producing a reliable metal film. These lasers have also been used for gas monitoring and stabilization. In chapter 8 the conclusions are summarized.

Chapter 2

Gratings in optical fibers

Optical gratings are among the key components in the optical fiber sensors studied in this thesis. In this chapter different gratings are described. A uniform Bragg grating is described in section 2.2, since it is the only grating which can be directly calculated. The wavelength response of the grating changes when the temperature or the strain is altered. This effect is described in section 2.2.1. The spectral response of a uniform Bragg grating can be calculated with the transfer matrix method, as illustrated in section 2.2.2.

Another type of grating is the long-period grating with period of the order of 100 μm, which couples light to cladding modes. The grating can be used as a bending sensor as investigated in chapter 3, and it is described in section 2.3.

A third type of grating, described in section 2.4, is called a sampled grating. It has many narrow reflection peaks, which enhance the reflected power. In chapter 4 a combination of a long-period grating and two sampled gratings is investigated. To be able to calculate the reflection spectrum, a transfer matrix for the sampled grating is described in section 2.4.1.

A fiber laser is an active component. It can be produced with Bragg gratings as cavity mirrors. In chapter 6 and 7 a DFB fiber laser is used for gas monitoring. This type of fiber laser is therefore described in section 2.5.

2.1 Gratings

When a silicon fiber is doped with germanium it becomes photosensitive. If it is irradiated with UV light around 240 nm, a change in the refractive index can occur. This is due to a change in the glass defects. The change

in absorption for the defects, is related to the change in refractive index through the Kramers-Kronig relation

$$\Delta n(\lambda) = \frac{1}{2\pi^2} \int_0^\infty \frac{\Delta\alpha(\lambda')d\lambda'}{1-(\lambda'/\lambda)} \tag{2.1}$$

where λ is the wavelength, $\alpha(\lambda)$ is the absorption coefficient and $n(\lambda)$ the refractive index. There are different models describing the changes in refractive index. In the color center model, defects with energy levels in the wide band-gap, can absorb sub-band-gap photons and trigger the change in refractive index [38]. Kristensen [39] has a model where the germanium sites works as gates for transferring the excitation energy into the silica. Other models explain the change in index with compaction of the fiber, when it is irradiated with laser light [40].

If the fiber is loaded with H_2 or D_2 the photosensitivity is enhanced. When hydrogen is used, it induces a OH defect, which has an absorption band near 1.39 μm in the telecommunication band. When a grating is written in a hydrogen loaded fiber, UV induced losses appear in the 1.5 μm telecommunication band [41]. Deuterium is often used instead, since the OD absorption lies at a longer wavelength, and the UV induced loss is shifted out of the 1.5 μm range [42], but deuterium is also more expensive.

A periodic change in refractive index is called a grating. Depending on the grating type, light can couple to for example a backward travelling fundamental mode or a forward travelling cladding mode. These changes in refractive index have a fast decaying component, and a more stable one. If no damage of the fiber occurs when a grating is written, it can be erased at high temperature and rewritten as before [43].

2.2 Uniform Bragg gratings

A uniform Bragg grating has a sinusoidal modulation in the refractive index of the optical fiber core, with a period of the order of 1 μm. Bragg gratings have a narrow reflection peak, and they are therefore used for telecommunication components, for example as a wavelength selective element in a wavelength division multiplexer (WDM). Furthermore they can be used for sensors, since the wavelength of the reflection peak is dependent on temperature, strain and acoustic changes.

Meltz and Morley [44] induced in 1989, a Bragg grating by irradiating the fiber with an interference pattern from two beams of light with a wavelength of 244 nm. The modulation in refractive index can be induced in the fiber by a UV light interference pattern, which is produced by either

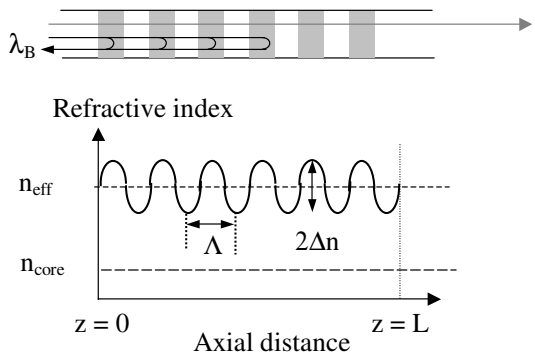

Figure 2.1: Illustration of the periodic modulation of a Bragg grating. Λ is the grating period and Δn is the amplitude.

an interferometric setup or a phasemask method. When an excimer laser is used as the UV source, it is necessary to use a phasemask due to the short coherence length. The excimer setup is described by Hübner [45]. The periodic modulation of a uniform Bragg grating is illustrated in figure 2.1 The index along the fiber can be written as

$$n(z) = n_{core} + \delta n_{eff}(z) + \Delta n(z) \cdot \cos\left(\frac{2\pi}{\Lambda} z + \phi(z)\right) \tag{2.2}$$

where ϕ is a phase shift in the periodic structure, Λ is the grating period, δn_{eff} is the DC contribution due to the UV exposure and Δn is the amplitude of the periodic modulation. This gives an effective refractive index n_{eff}, which is the mean value of the refractive index.

When light passes a fringe of a Bragg grating, a fraction of light in the fiber is reflected. Backwards reflection happens when the optical path length between the fringes is half the wavelength of the incoming light, since the reflected light adds up coherently. This is called the Bragg condition, and it can be written as

$$m\frac{\lambda}{2} = n_{eff}\Lambda \tag{2.3}$$

where m is the diffraction order. In the case m=1 the wavelength which fulfills equation 2.3 is called the Bragg wavelength:

$$\lambda_B = 2n_{eff}\Lambda \tag{2.4}$$

When the phasemask technique is used, the Bragg wavelength can be written as

$$\lambda_B = n_{eff}\Lambda_{mask} \tag{2.5}$$

since the grating period is half the period of the phasemask, Λ_{mask}.

2.2.1 Sensitivity of the Bragg wavelength

When a Bragg grating is influenced by temperature (T) or strain ($\epsilon \equiv \frac{\Delta l}{l}$) the Bragg wavelength changes. Since the Bragg wavelength is given by equation 2.4, the change in Bragg wavelength, as a function of temperature for a constant strain, is

$$\frac{\Delta\lambda_B}{\Delta T} = \left(2\frac{\partial n_{eff}}{\partial T}\cdot\Lambda + 2\frac{\partial\Lambda}{\partial T}\cdot n_{eff}\right)|_{\epsilon=const.} \tag{2.6}$$

which can be written as

$$\frac{\Delta\lambda_B}{\lambda_B} = \left(\frac{\partial n_{eff}}{\partial T}\cdot\frac{1}{n_{eff}} + \frac{\partial\Lambda}{\partial T}\cdot\frac{1}{\Lambda}\right)\Delta T|_{\epsilon=const.} \tag{2.7}$$

Equation 2.7 can be expressed by the thermal length expansion α and the thermo-optic coefficient ξ by [46]

$$\frac{\Delta\lambda_B}{\lambda_B} = (\alpha+\xi)\,\Delta T|_{\epsilon=const.} \tag{2.8}$$

where the thermal length expansion for fused silica is

$$\alpha = \frac{1}{\Lambda}\frac{\partial\Lambda}{\partial T} = 0.55\cdot 10^{-6}K^{-1} \tag{2.9}$$

and the thermo-optic coefficient, which depends on the fiber, is given by

$$\xi = \frac{1}{n_{eff}}\cdot\frac{\partial n_{eff}}{\partial T} \sim 9\cdot 10^{-6}K^{-1} \tag{2.10}$$

If instead the axial strain is altered at a constant temperature, the change in Bragg wavelength can be written

$$\frac{\Delta\lambda_B}{\lambda_B} = \left(\frac{\partial\Lambda}{\partial\epsilon}\cdot\frac{1}{\Lambda} + \frac{\partial n_{eff}}{\partial\epsilon}\cdot\frac{1}{n_{eff}}\right)\Delta\epsilon|_{T=const.} = (1-p_e)\,\Delta\epsilon|_{T=const.} \tag{2.11}$$

where $p_e = 0.22$ is the effective strain optic constant for fused silica. When a tensile force is applied to a fiber (with cross section area A) the stress is $\sigma = F/A$. The relationship between strain and stress is given by [47]

$$\sigma = E_0\epsilon\left(1+\frac{\alpha}{2}\epsilon\right) \tag{2.12}$$

where Young modulus $E_0 = 72$ GPa, and $\alpha = 6$ for fused silica.

This gives the relationship between the Bragg wavelength and the tensile force as

$$\frac{\Delta\lambda_B}{\lambda_B} \simeq \frac{1-p_e}{E_0 A}F \tag{2.13}$$

for stress below the breaking limit.

2.2.2 Transfer matrix for a uniform Bragg grating

The electromagnetic field in a fiber can be described as a wave with separate transverse and longitudinal dependent components given by

$$E(x,y,z,t) = F(x,t) \cdot A(z,t) e^{-i(\beta_0 z - \omega_0 t)} \tag{2.14}$$

with $A(t) = \hat{x}A_x(t) + \hat{y}A_y(t)$, where β_o is the propagation constant and ω_0 is the angular frequency of the wave. If there is a periodic structure the field can be written as a combination of a forward ($E_A(z)$) and a backward ($E_B(z)$) propagating wave [48]

$$E(z) = E_A(z) + E_B(z) = A(z) \cdot e^{-i\beta_B z} + B(z) \cdot e^{i\beta_B z} \tag{2.15}$$

In the coupled mode theory the fiber is assumed to support the fundamental transverse mode, and the electric field and the optical medium is assumed to be independent of the x and y coordinates. Further the chromatic dispersion is neglected. For wave propagation in Bragg gratings the coupled mode equation for the complex electric field amplitude at the angular frequency ω in the z direction is given by the scalar equation

$$\frac{\partial^2 E}{\partial z^2} + \tilde{\beta}^2(z) E = 0 \tag{2.16}$$

$\tilde{\beta}(z)$ is the propagation function given by the sum of the propagation constant β_0 and a small perturbation $\delta\beta(z)$ due to the grating. That is

$$\begin{aligned} \tilde{\beta}(z) &= \beta_0 + \delta\beta(z) && (2.17)\\ \beta_0 &= \frac{2\pi n_{eff}}{\lambda} && (2.18)\\ \delta\beta(z) &= k\Delta n \cos\left(\frac{2\pi}{\Lambda} z + \phi\right) && (2.19) \end{aligned}$$

where $k = \frac{2\pi}{\lambda} = \frac{\omega}{c}$ is the wave number.

The deviation from the Bragg condition is called the detuning, and it is given by:

$$\delta = \beta_0 - \beta_B = n_{eff}\left(\frac{2\pi}{\lambda} - \frac{2\pi}{\lambda_B}\right) = \frac{2\pi n_{eff}}{\lambda} - \frac{\pi}{\Lambda} \tag{2.20}$$

This gives the coupled mode equations [31, 45, 48]

$$\begin{aligned} \frac{\partial A}{\partial z} &= i\delta A + i\kappa B e^{-i\phi} && (2.21)\\ \frac{\partial B}{\partial z} &= -i\delta B - i\kappa^* A e^{i\phi} && (2.22) \end{aligned}$$

where ϕ is a discrete phase shift and κ is the coupling coefficient. For a Bragg grating written with a phasemask in a fiber with confinement factor η, κ is defined as

$$\kappa = \frac{\pi\eta\Delta n}{n_{eff}\Lambda_{mask}} \tag{2.23}$$

For a uniform Bragg grating with length L the coupled mode equations can be solved.

The transfer matrix can be written as [31, 45, 49]

$$\begin{pmatrix} E_A(0) \\ E_B(0) \end{pmatrix} = \begin{bmatrix} T_{11} & T_{12} \\ T_{21} & T_{22} \end{bmatrix} \begin{pmatrix} E_A(L) \\ E_B(L) \end{pmatrix} \tag{2.24}$$

where

$$\begin{aligned} T_{11} &= \left[\cosh(\gamma L) - i\frac{\delta L}{\gamma L}\sinh(\gamma L)\right] e^{i\beta_B L} \\ T_{12} &= \left[-i\frac{\kappa L}{\gamma L}e^{-i\phi}\sinh(\gamma L)\right] e^{-i\beta_B L} \\ T_{21} &= \left[i\frac{\kappa L}{\gamma L}e^{i\phi}\sinh(\gamma L)\right] e^{i\beta_B L} \\ T_{22} &= \left[\cosh(\gamma L) + i\frac{\delta L}{\gamma L}\sinh(\gamma L)\right] e^{-i\beta_B L} \end{aligned} \tag{2.25}$$

and

$$\gamma = \sqrt{\kappa^2 - \delta^2} \tag{2.26}$$

The amplitude of the forward propagating wave is normalized to one, $E_A(L) = 1$. There is no backwards travelling wave after the grating so $E_B(L) = 0$. The reflection coefficient is therefore: $r_g = -E_B(0)/E_A(0) = -T_{21}/T_{11}$, and the transmission coefficient is: $t_g = E_A(L)/E_A(0) = 1/T_{11}$. The reflectivity is given by $R = |r_g|^2$.

For a Bragg grating the peak reflectivity R_{max} is:

$$R_{max} = \tanh(\kappa L)^2 \tag{2.27}$$

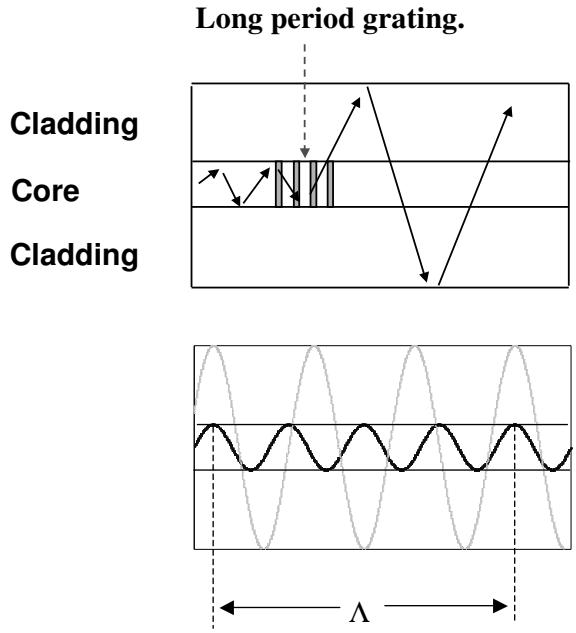

Figure 2.2: Illustration of the processes in a long-period grating and the grating period, Λ where the two modes are in phase.

2.3 Long-period gratings

A long-period grating has a period of the order of 100 μm. It couples light from the fundamental core mode to cladding modes as shown on figure 2.2. The grating period Λ is the distance between two points, where the core and cladding modes are in phase. The resonances of the long-period grating are given by the phase-matching condition [1]

$$\lambda = \Lambda(n_{co}^{eff} - n_{cl}^{eff}) \tag{2.28}$$

where n_{co}^{eff} and n_{cl}^{eff} are the effective refractive index in the core and cladding respectively.

A long-period grating is produced with an amplitude mask, which blocks the UV light in a periodic way, as described by Rathje [50]. Erdogan has a notation of the resonances which is given in reference [51], where 1ν denotes the fundamental core mode and the ν cladding mode. Erdogan [49] has also shown how to calculate the transfer matrix for a transmission grating. This will not be described here, since the calculations demand detailed knowledge of the refractive index in the core and cladding.

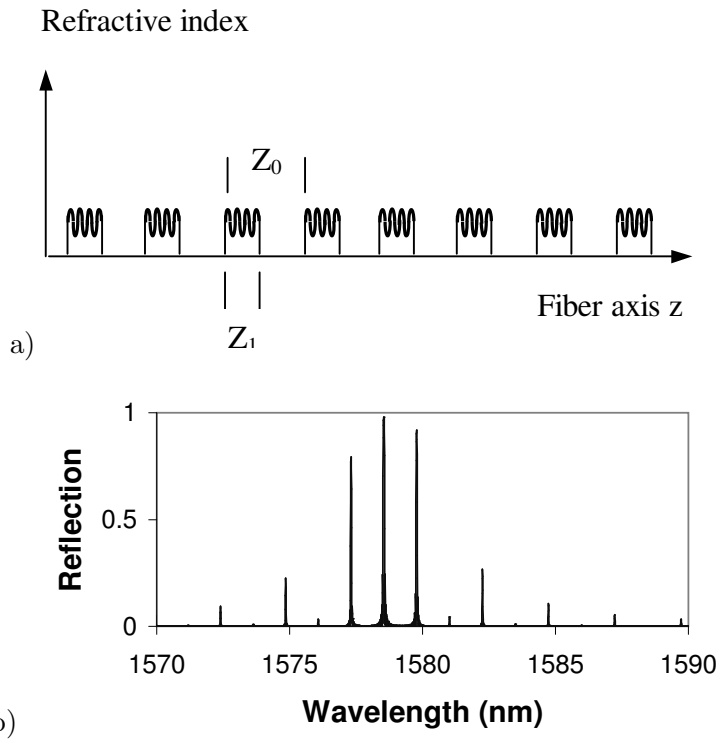

Figure 2.3: Illustration of a) the induced refractive index change for a sampled grating. z_0 is the sampling period and z_1 is the length of a single grating parts and b) a reflection spectrum for a sampled grating with $z_1/z_0 = 1/2$.

2.4 Sampled gratings

A sampled grating has multiple narrow reflection peaks. It is produced by using a phasemask to induce a Bragg grating, and an amplitude mask to sample the induced Bragg grating. An illustration of the induced index change is shown in figure 2.3. The spectral shape of the reflection peaks is determined by the Fourier transformation of the envelope function of $\kappa(z)$. For a uniform envelope function the shape is a sinc function. The overall shape of the reflection spectrum is determined by the Fourier transformation of $\kappa(z)$ for a single Bragg grating. In the case of a uniform Bragg grating, the overall envelope function is a sinc funcion. Hübner [45] gives an excellent description of sampled gratings, and the behavior of the reflection peaks. The distance between the peaks is equidistant in frequency, if

the dispersion is ignored [52]:

$$\Delta\nu = \frac{c}{2z_0 n_{eff}} \tag{2.29}$$

where z_0 is the sampling period and c is the speed of light.

2.4.1 Transfer matrix for a sampled grating

For a non-uniform Bragg grating the grating is divided into N sections which can be treated as uniform Bragg gratings. The total transfer matrix $\mathbf{T}$ is found by matrix multiplication of the transfer matricies $\mathbf{T^{(k)}}$ for the different sections:

$$\mathbf{T} = \prod_{k=1}^{N} \mathbf{T^{(k)}} \tag{2.30}$$

The transfer matrix for a sampled grating, can be calculated by dividing the grating in Bragg grating parts and non grating parts. In the sections where there is no discrete phase shift, the optical path length gives an accumulated phase. This can be represented by the transfer matrix $\mathbf{T_{Phase}}$ given by

$$\mathbf{T_{Phase}} = \begin{pmatrix} e^{-i\phi/2} & 0 \\ 0 & e^{i\phi/2} \end{pmatrix} \tag{2.31}$$

Where $\phi/2 = 2\beta_0(z_0 - z_1)$.
The total transfer matrix for a sampled grating is therefore given by:

$$T_{sg} = (\prod_{i}^{s} T_{BG,i} T_{Phase,i}) T_{BG} \tag{2.32}$$

where s is the number of sections.
The reflection for the central peak of the sampled grating is given by

$$R_{max} = \tanh(\kappa_0 \frac{z_1}{z_0} L) \tag{2.33}$$

That is, the strength of a sampled grating is z_1/z_0 of the strength of a Bragg grating with the same total length.

2.5 DFB fiber laser

A fiber laser is based on a fiber doped with atoms, which work as an active medium. The most used dopant is erbium, which has an emission band from 1530 nm to around 1610 nm. One way to produce a fiber laser is

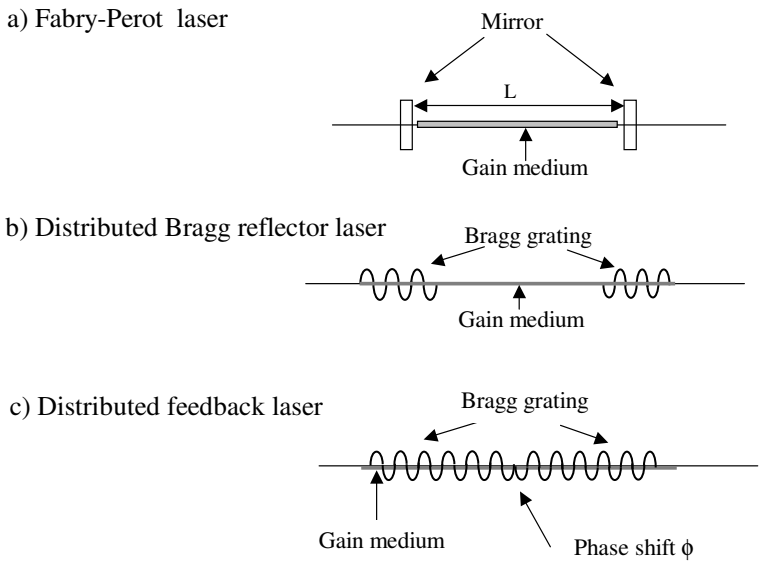

Figure 2.4: Illustrations of continuous lasers a) A Fabry-Perot laser, b) A distributed Bragg reflector (DBR) laser, c) Distributed feedback (DFB) laser.

with a ring configuration [17, 18, 19]. The advantage is a large wavelength tuning range, but a wavelength selective element, such as a Bragg grating, is necessary to achieve single-mode operation. Another type of fiber laser is based on a laser cavity with Bragg gratings as reflection mirrors [53, 22] like a Fabry-Perot laser (figure 2.4a). This type of laser (called a distributed Bragg reflector (DBR) laser) is shown in figure 2.4b.
The frequencies ν_m of the laser modes are described by:

$$\nu_m = m \cdot \frac{c}{2n_{eff}L} \tag{2.34}$$

where L is the cavity length. The number of modes is determined by the cavity length. This demands a short cavity length if single-mode operation is required.
Another way of producing a single-mode fiber laser is to make a distributed feedback (DFB) laser, where there is a discrete phase shift of $\pi/2$ between two Bragg gratings with zero distance between them [23, 24, 25]. The $\pi/2$ phase shift gives a phase change of π on a round trip, this means that light which matches the optical path length is not reflected. There is therefore a small transmission band in the reflection peak. It is this wavelength which is lasing. The DFB fiber laser is illustrated in figure 2.4c.

An erbium doped laser can be pumped with 980nm light which excites the erbium from the ${}^4I_{15/2}$ to the ${}^4I_{11/2}$ state, where 1480 nm pump light excites the erbium atoms to the meta-stable ${}^4I_{13/2}$ state [54]. Varming [31] has found the transfer matrix for a DFB fiber laser. The result is not quoted here since no calculations are done with fiber lasers.

A DFB fiber laser can have an output power of the order of 100 μW, since there is an upper limit to the erbium amount, above which clustering effects can occur. A way to increase the output power without increasing the pump power (or using an erbium amplifier) is to add Yb^{3+} into the core [25, 26]. When the fiber laser is pumped with 980 nm light both erbium and ytterbium absorb the pump. The energy absorbed by the ytterbium atoms is transferred to the erbium atoms via a non-radiative energy exchange. In this case several mW is achieved. The problem with adding Yb^{3+} is the lack of photosensitivity, since germanium will reduce the performance. Instead it is possible to add germanium and boron in a ring around the core to produce photosensitivity, and thereby produce a fiber laser [26]. The boron is added since it lowers the refractive index where germanium increases it. Since a fraction of the light in the fundamental mode is confined in the cladding, the grating in the ring around the core still works like a laser cavity.

Chapter 3

Long-period gratings for bending sensing

In the following two chapters, two examples of direct sensing are investigated. In this chapter a direction dependent bend sensor, based on a fiber with a core concentricity error is investigated.

3.1 Motivation

When light passes a long-period grating (LPG), it can couple to cladding modes as explained in section 2.3. This gives transmission loss for wavelengths which satisfy the phase matching condition:

$$\lambda = \Lambda(n_{co}^{eff} - n_{cl}^{eff}) \tag{3.1}$$

where n_{co}^{eff} and n_{cl}^{eff} are the effective refractive index in the core and cladding respectively.

The resonance wavelength depends on the refractive index of the surroundings, so it can be used as a chemical sensor, since different chemical have different resonances [2].

An example of wavelength resonances before and after out diffusion of deuterium is illustrated in figure 3.1a. The transmission is not normalized with respect to the light source. It is seen that the resonance wavelength is moved approximately 15 nm towards longer wavelength when the D_2 is out diffused. This is the case, since some of the deuterium is bound in the core, where the grating is written, and probably less is bound in the cladding, so the resonances shift to longer wavelengths. Figure 3.1b shows the same grating when it is straight and when it is bent. It is seen that

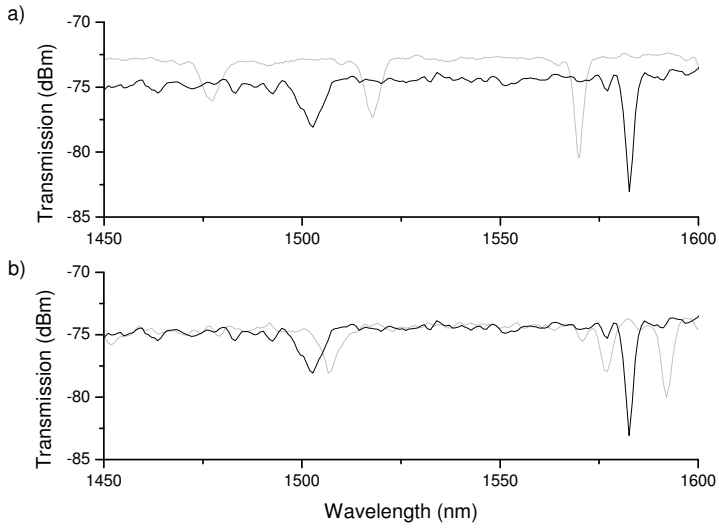

Figure 3.1: Resonances for a long-period grating with period 250 μm a) before (gray) and after (black) out diffusion of D_2 and b) when the grating is straight (black) and bent (gray).

the resonances split when the grating is bent. The wavelength splitting is largest for higher order cladding modes.

A long-period grating can also be used as gain flattening filter in an erbium doped amplifier [1]. These gratings have been used as sensor elements to measure effects like strain [9, 10, 13], temperature [10, 11] and bend [3, 4, 5, 6]. When the long-period grating is bent, the resonance wavelength splits into two dips. Steblina *et al* [55] have observed a splitting of the core-cladding mode when a fiber (without a long-period grating) was bent. They explained the splitting with breaking of symmetry. When the fiber has a core concentricity error (CCE) the resonances are intrinsically split. Rathje [7] has shown that if the fiber has a core concentricity error, the long-period grating can be used as a direction dependent bend sensor. The optimum direction was determined by measuring the bending sensitivity for different directions. To maximize the bending sensitivity the CCE must be increased, as also demonstrated by Patrick [8] using a fiber with a CCE of 14 μm. However, this large CCE resulted in a natural bent, which can impose limitations in some practical implementations.

In this chapter different properties of a long-period grating in a fiber with a CCE of 2.4 μm is investigated. Rathje [50] had some problems with reproducibility which are solved now. The CCE direction can be determined with a perpendicular light diffraction facility, and this technique makes it

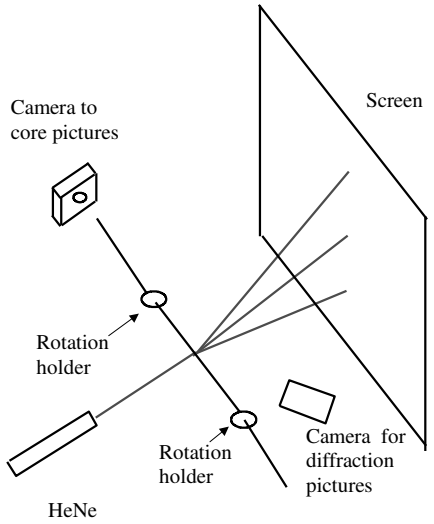

Figure 3.2: Setup for diffraction investigations. The diffraction pattern can be seen by the eye, and a picture can be taken with a digital camera.

possible to write the grating with a beam perpendicular or parallel to the CCE direction (se section 3.2). The temperature and bending sensitivity of these long-period gratings are also investigated.

3.2 Perpendicular light diffraction and writing a long-period grating

By means of diffraction the CCE direction can easily be found. For this light from a HeNe laser was used perpendicular to the stripped part of the fiber, which was mounted in a rotation holder. The diffraction pattern is seen vertical on a screen. This is illustrated in figure 3.2, together with the digital camera for the diffraction pictures and the one for the core pictures. The zero order diffraction has to be damped since it saturates the digital camera.

When the fiber rotates, the diffraction pattern changes. The pattern is symmetric when the CCE direction is in the laser direction, and asymmetric otherwise. The diffraction pattern is shown in figure 3.3a with a fiber rotation of 45 degrees between each pattern. The patterns at 0^0 (number 1) and 180^0 (number 5) are symmetric, whereas 90^0 (number 3) and 270^0 (number 7) are maximally asymmetric. Figure 3.3b shows the end picture corresponding to the 270^0 rotation of the fiber core. Consequently,

a) 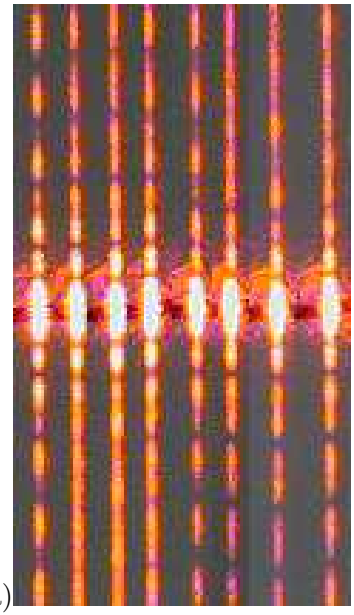 b) 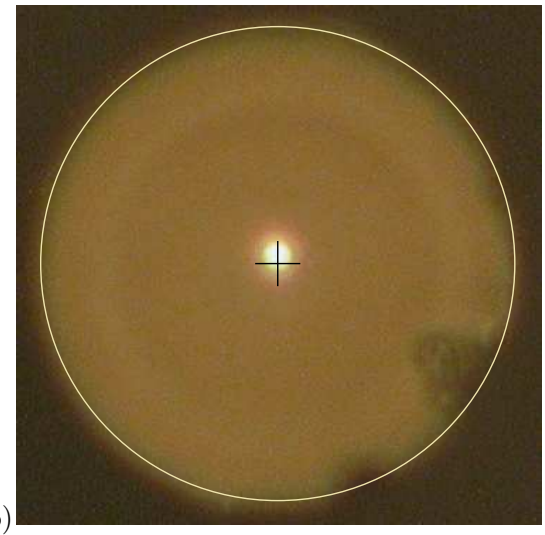

Figure 3.3: a) Diffraction pattern, the first is symmetric (0 degrees), number 3 (90 degrees) and 7 (270 degrees) show maximum asymmetric. b) The core picture corresponds to the diffraction pattern at 270 degrees.

when a diffraction pattern corresponds to the aforementioned 270^0 rotation pattern, the CCE will point upwards.

This knowledge of the CCE direction can be used to write a grating with the CCE parallel (a) or perpendicular (b) to the UV light (see figure 3.4).

The long-period gratings were fabricated in an unloaded Ge-doped fiber, with a CCE of 2.4 μm. After orientation of the CCE direction a long-period grating with a length of 3 cm was written, using an amplitude mask with a period of 250 μm. The writing was done by excimer laser exposure with a total fluence of $\sim$ 5.5 kJ/cm^2. The fluence was high, because the fiber was not loaded, so the photosensitivity was only due to the germanium. A broadband LED and an optical spectrum analyzer were used for the measurements.

3.3 Bending sensitivity

To investigate the bend sensitivity dependence of the CCE direction during grating writing, a long-period grating (A) with the CCE parallel and one

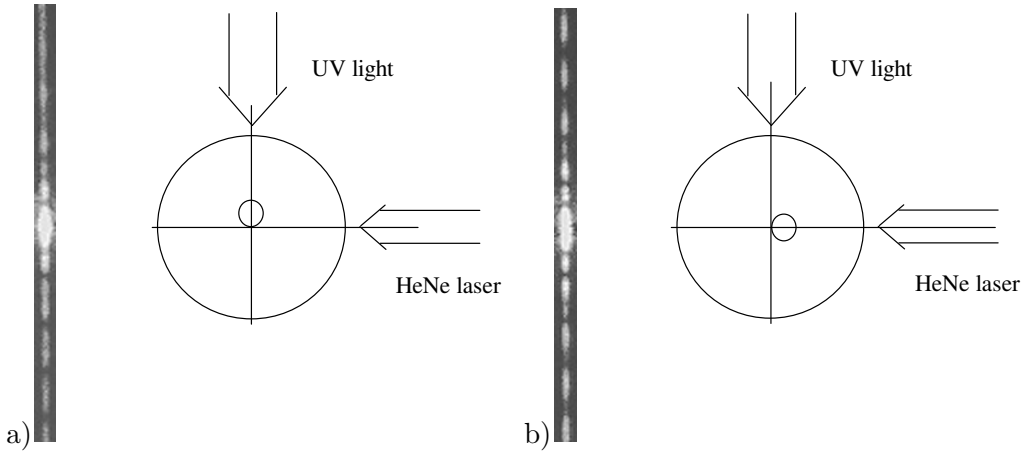

Figure 3.4: Diffraction pattern and CCE direction for a) a grating with the CCE direction parallel to the writing beam, b) a grating with the CCE direction perpendicular to the writing beam.

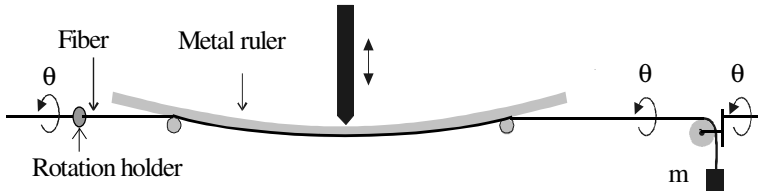

Figure 3.5: The bending setup. The mass, m, ensures a constant longitudinal force on the grating.

long-period grating (B) with CCE perpendicular to the UV light, were bent in different directions and compared. The bending measurements were performed in a setup similar to the setup in reference [7]. To improve the setup two rotation holders were used instead of tape stickers, since the tape twisted when put on the fiber. The setup is shown in figure 3.5. The load induces a constant strain during the bending measurements. It is ensured that the device with the load can rotate together with the rotation holder, and still have the same force transfer from the load.

When the metal ruler is pressed down, it induces a bend of the fiber. The curvature of this bend can be found with a standard formula [56] given by:

$$f(x) = -d\left(3\frac{x}{L} - 4\left(\frac{x}{L}\right)^3\right),\ x \leq \frac{L}{2} \tag{3.2}$$

where d is the depression of the ruler, and L the distance between the outer

bending points. The curvature can be found from equation 3.2 by [56]

$$c(x) = \frac{f''(x)}{(1+f'(x)^2)^{3/2}} = \frac{\frac{24dx}{L^3}}{\left(1+\left(d\left(\frac{3}{L}-\frac{12x^2}{L^3}\right)\right)^2\right)^{3/2}} \tag{3.3}$$

It is seen that the curvature depends on the distance from the center. It is therefore important to place the long-period grating symmetrically around the center. If the grating is misaligned, it will give a systematic error in the bending, since the fiber is rotated and not aligned between measurements.

The bend response for different directions is almost symmetric for grating A and asymmetric for B, as illustrated on the polar plot in figure 3.6. The wavelength splitting is represented by the radial distance from the center, and the angle is between the CCE direction and the bending direction. The asymmetry is due to writing induced difference in the refractive index in the x and y direction, called birefringence, which varies through the fiber because of different intensity of the writing beam. When the writing beam is parallel with the CCE direction, the difference induced birefringence is largest in the bending direction where the wavelength splitting is increasing or decreasing most, so the plot should be symmetric along this axis if the fiber was perfectly aligned. For the grating B that is written in the fiber with CCE direction perpendicular to the writing beam, the difference in birefringence is largest in the writing direction i.e. in the 90-270 degree direction. This is seen as a big asymmetry in the polar plot.

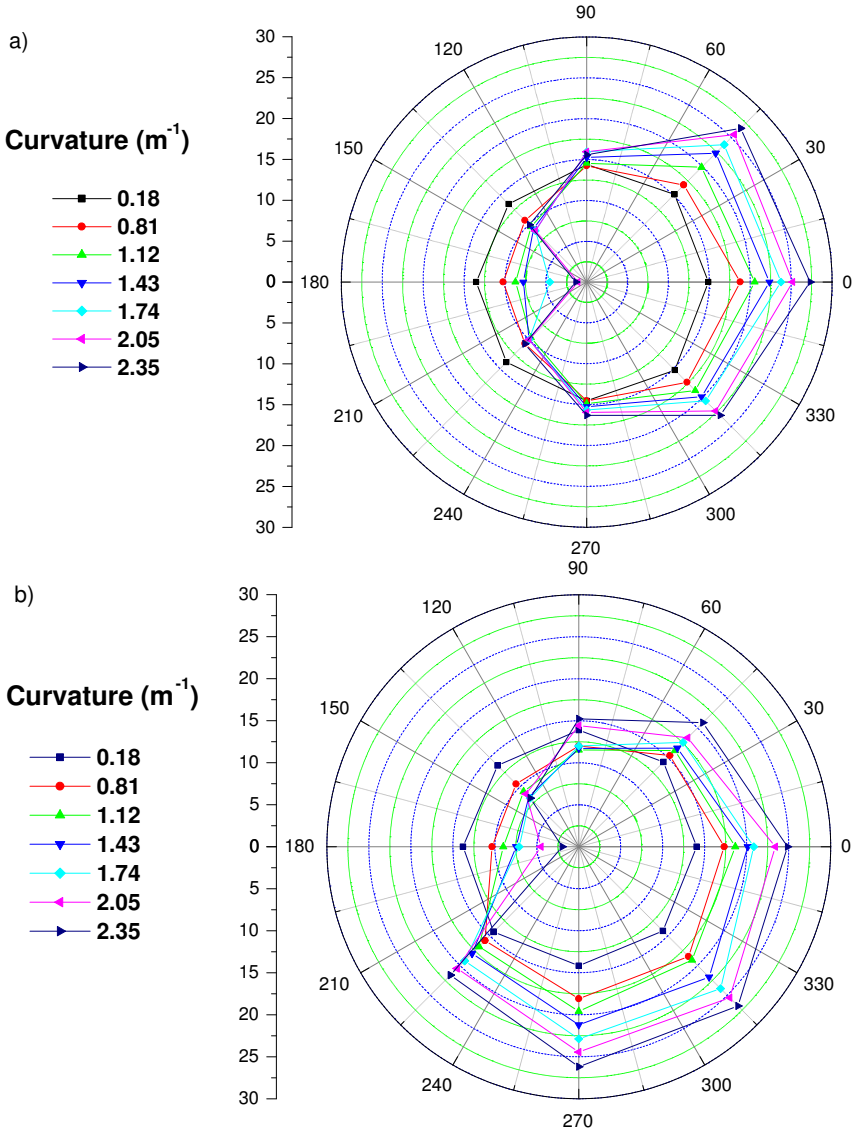

Figure 3.6: Polar plot of the bending response for gratings written with a) parallel and b) perpendicular CCE direction compared with the UV light. The radial part is the wavelength splitting, and the angle is between the CCE direction and the bending direction.

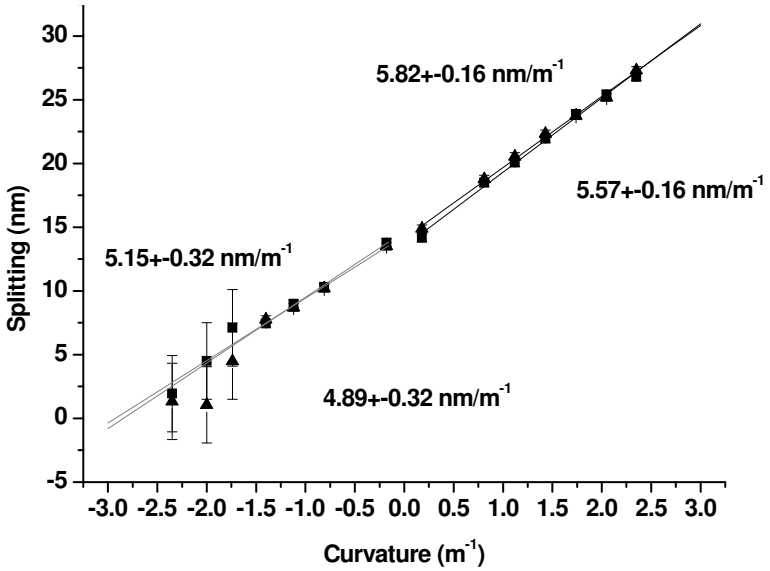

Figure 3.7: Optimum bend response for long-period grating A with parallel CCE (triangle) and for the long-period grating B with perpendicular CCE (square).

Figure 3.7 shows the bending response in the directions where the wavelength splitting increases and decreases most i.e. in the 0-180 degree direction. The response for long-period grating A is (4.89 $\pm$ 0.32) nm $\cdot$ m and (5.57 $\pm$ 0.16) nm m for down- and upward bend respectively. For long-period grating B the response for downward bend is (5.15 $\pm$ 0.32) nm $\cdot$ m and (5.82 $\pm$ 0.16) nm $\cdot$ m for upward bend. The behavior in the optimal bend direction is therefore almost independent of the writing direction. Patrick [8] showed that there is a continuous change in splitting from forward to backwards bend. In the regime near zero bend the sensitivity is therefore lower than 5 nm/m^{-1}.

For grating A the two peaks overlapped for curvatures corresponding to the interval between -1.75 m^{-1} and -2.35 m^{-1} (se figure 3.8). When the curvature decreased further the peaks separated again. It was not possible to determine whether they had passed through each other or not, since the small peak was at the left as before the overlap.

A diffraction measurement afterwards showed that the CCE is upward when a downward bend gave a minimal splitting. This is in agreement with Patrick's results [8].

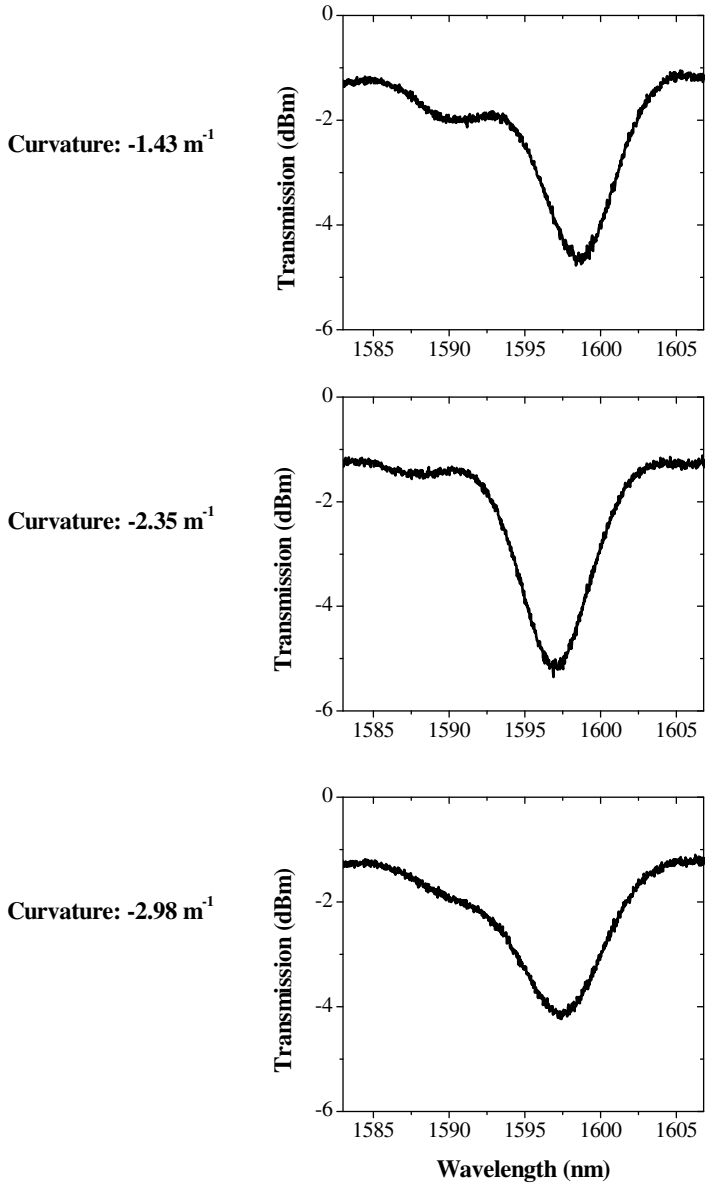

Figure 3.8: Decrease in curvature for grating A gave an overlap of the two peaks for a curvature of -2.35 m^{-1} (middle graph), the upper and lower graphs show the transmission spectrum for a radius of curvature of -1.43 m^{-1} and -2.98 m^{-1} respectively.

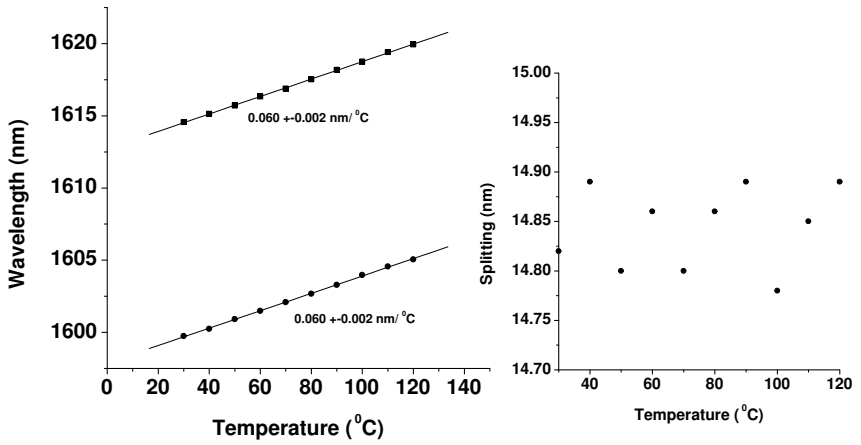

Figure 3.9: Temperature dependence of the split resonance. The insert shows the wavelength splitting.

3.4 Temperature sensitivity

The resonance wavelength of a grating changes with temperature. To investigate the behavior of the wavelength splitting, grating A was heated by a heat plate at a rate of 4 ^{0}C/min in the temperature interval 30-120 ^{0}C. To prevent bending when the fiber expanded due to the heat, the long-period grating was mounted with a load. Figure 3.9 shows the response of the two peaks which corresponds to the (17) cladding mode [51]. It is seen that the sensitivity is 0.060 ± 0.002 nm/^{0}C for both the lower and higher wavelength. The maximum difference in the splitting is about 0.1 nm, which is within the uncertainty of the measurement estimated to be around 0.2 nm. The splitting is therefore insensitive to temperature changes in this interval. It is only grating A which was heated, since grating A and B behaves equal when they are not bent.

3.5 Discussion

The temperature and strain will only displace the resonance wavelength, but it will not change the splitting. The sensor can therefore be used for bending sensing, in the case where the temperature and strain is of no concern. This sensor depends on a way to measure the wavelength

splitting to investigate the bend. This can be done either with an optical spectrum analyzer, or by scanning the wavelength through the wavelength range of interest and detect the transmission signal. The detection system is therefore limited to cases, where the change is slow compared to the measuring time.

3.6 Conclusion

Diffraction can be used to determine the CCE direction. It is therefore simple to write gratings with a certain CCE direction compared with the writing direction. Furthermore it is easy to determine the direction of the maximal bending response. This enables a simple way of mounting the sensor, since the orientation can be determined before use. Since the writing direction and temperature does not affect the wavelength splitting it is possible to make simple, robust bending measurements.

Chapter 4

Temperature and strain sensor based on sampled and long-period gratings

In the prior chapter an example of a sensor based on wavelength measurements was studied. In this chapter a sensor to resolve temperature or strain changes is investigated. It is based on measurements of the reflected power.

Different gratings have different strain and temperature dependencies, so a combination can be used to resolve the effects. A combination of a long-period grating and a Bragg grating has been used to resolve temperature and strain [11, 12, 13]. There are also examples of specially designed cases where the long-period grating has either a temperature or a strain dependence [14, 15, 16].

A Bragg grating has a narrow reflection band where a sampled grating behaves like a Bragg grating, but it has several reflection peaks. In the following chapter a combination of two sampled and one long-period grating is investigated, to make temperature and strain measurements possible with a simple and cheap detection scheme.

4.1 Experiment

A long-period grating of length 3 cm, with a period of 250 μm and a duty cycle of 50/50 was written in a D_2 loaded DK-SM fiber with a total fluence of 117 J/cm^2. The resonances moved $\sim$15 nm after out diffusion of D_2. Afterwards one of the resonances was at $\sim$1580 nm with a transmission loss of $\sim$10 dB. Two sampled gratings were written in the same type of fiber with an amplitude mask with period 700 μm and 500 μm respectively,

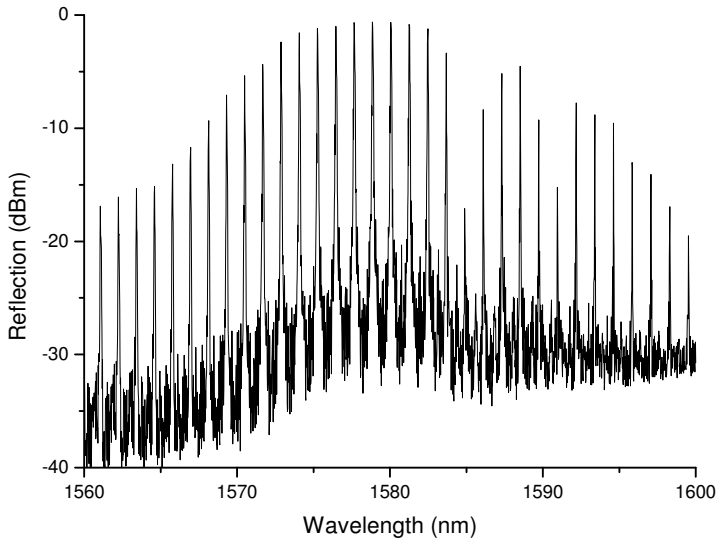

Figure 4.1: A reflection spectrum from a sampled grating. The fiber has a long-period dip in the same wavelength range, thus giving a dip in the reflection spectrum.

and a duty cycle of 1/5. The phasemask had a period of 1088 nm, to get the reflection peaks around 1580 nm. The total fluence was 200 J/cm^2. As shown on figure 4.1 the reflection spectrum is very broad and it has a dip approximately where the long-period grating has a resonance. If the grating is used, the long-period change will be measured together with the sampled grating. It is therefore only possible to resolve the two contributions, if the wavelength spectrum is measured. Since one of my goals is to make a cheap sensor, it is necessary to measure with and without the long-period grating to resolve the temperature and strain effects.

To achieve this two sampled gratings were written in a HD-SM fiber with a duty cycle of 50/50 to get a higher maximal reflection, for a reasonable total fluence. The gratings were written with an amplitude mask with period 700 μm and a phasemask with period of 1094 nm, to get the reflection peaks around 1580 nm, with a total fluence of 270 J/cm^2. This fiber can also be used for long-period gratings, but the resonances are at different wavelengths. The reflection of the two grating are shown on figure 4.2. They have maximal transmission losses of 14 dB and 17 dB which gives $\kappa L = 2.29$ and $\kappa L = 2.64$ from equation 2.33. From these transmission dips the reflections can be calculated to be -0.17 dBm and -0.09 dBm. The reason for the lower reflection values in figure 4.2 is insertion loss and loss

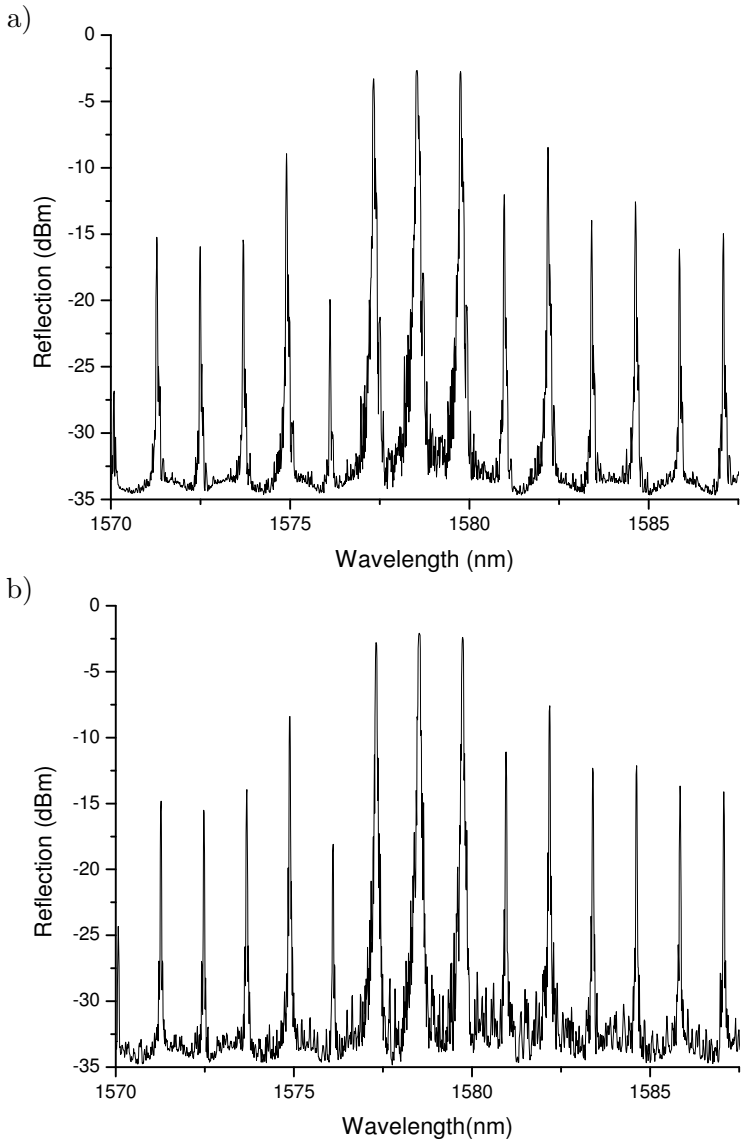

Figure 4.2: Reflection spectra of two sampled gratings A and B

in the circulator. Grating A is used as a reference grating, since it is shifted against higher wavelengths.

The temperature and strain dependence for grating B and the long-period grating can be investigated with a tunable laser source and an optical spectrum analyzer (OSA). This system will be referred to as the OSA

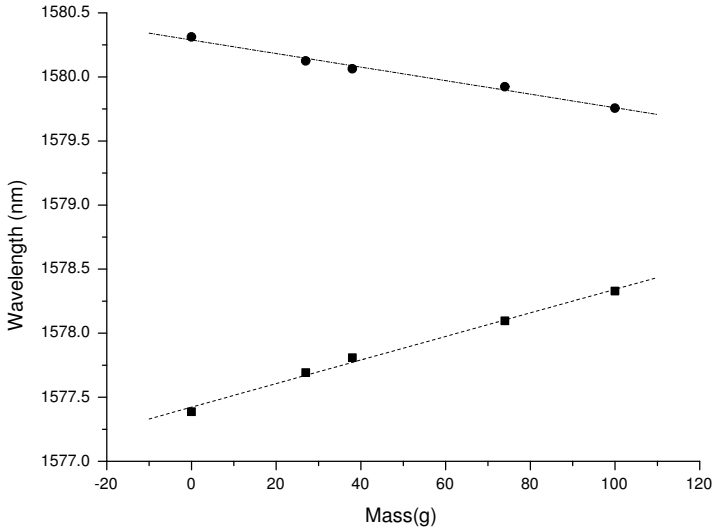

Figure 4.3: One reflection peak from the sampled grating B (■) and the resonance wavelength of the long-period grating (•) as a function of applied mass.

system. Figure 4.3 shows the strain response. Under these measurements it was observed that the distance between reflection peaks and their widths were unchanged when the temperature or strain was changed.

The found coefficients are shown in table 4.1.

	dλ/dT [nm/^{0}C]	dλ /dm [nm/g]
Grating B	0.009	0.0093
LPG	0.043	-0.0053

Table 4.1: Coefficients for grating B and the long-period grating.

From these coefficients it is possible to write the wavelength change of the sampled grating as

$$\Delta\lambda_{sg} = 0.009\Delta T \ + 0.0093\Delta m \tag{4.1}$$

and the change in resonance wavelength of the long-period grating as

$$\Delta\lambda_{lpg} = 0.043\Delta T \ - 0.0053\Delta m \tag{4.2}$$

The coefficients for the wavelength as a function of applied mass can be calculated to be a function of strain, since $\epsilon = m \cdot 9.82/(E_0 A) = m \cdot 1.11 \cdot 10^{-2}$. This makes it possible to resolve the strain.

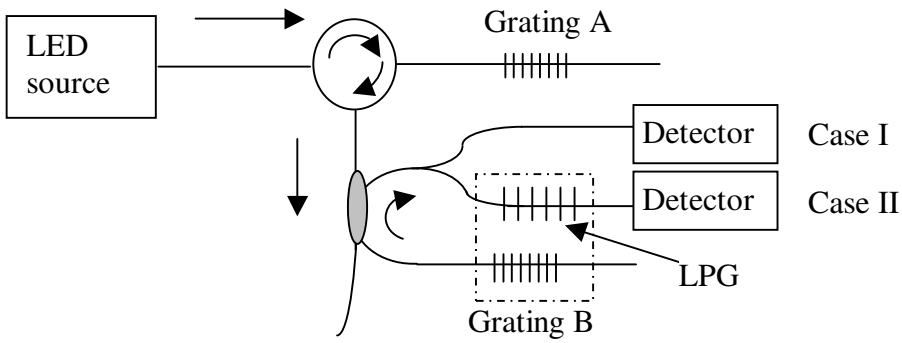

Figure 4.4: The setup for measuring temperature and strain. In the setup one circulator and one 3 dB coupler were used.

4.2 Results

A broad band LED and a HP detector is used to make the sensor as cheap as possible. To investigate what actually happens when the temperature or strain is applied, a tunable laser and an optical spectrum analyzer are used for additional measurements. Figure 4.4 shows the setup. To minimize the loss the second beam splitter was not used. Instead the long-period grating was inserted for the measurements called case II and not inserted in case I.

The reflection from B of the reflection from A (case I) at 21 ^{0}C is shown in figure 4.5. Figure 4.6 shows the reflection from B of the reflection of A transmitted through the long-period grating (case II) at 21 ^{0}C. The loss induced by the long-period grating is clearly seen by the dip around 1580 nm.

Figure 4.7 shows the reflected power measured with a detector as a function of temperature. It is seen that the dynamic range is 20 dB, when the temperature is changed 40 ^{0}C. Since the reflection peaks are sinc-functions (se section 2.4), a variation in the measured power will occur, when the small side lopes passes through the main peak of the first reflection spectrum. At each temperature the reflected power was measured with the detector, and the behavior was investigated with the OSA system. This induces varying losses from temperature to temperature, since the cables are changed between the light sources and detector systems. The error bars are set to ± 1 dBm and $\pm 1^0$C, since the loss can vary from one measurement point to the next, and the temperature can vary depending on how well the heat has stabilized, and on how good the heat contact is.

The reflected power can also be measured as a function of the applied

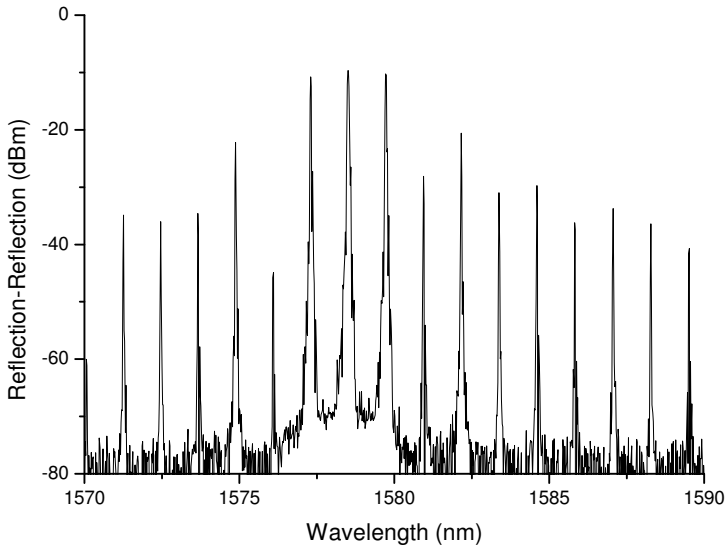

Figure 4.5: Reflection from B of the reflection of A measured with the OSA system.

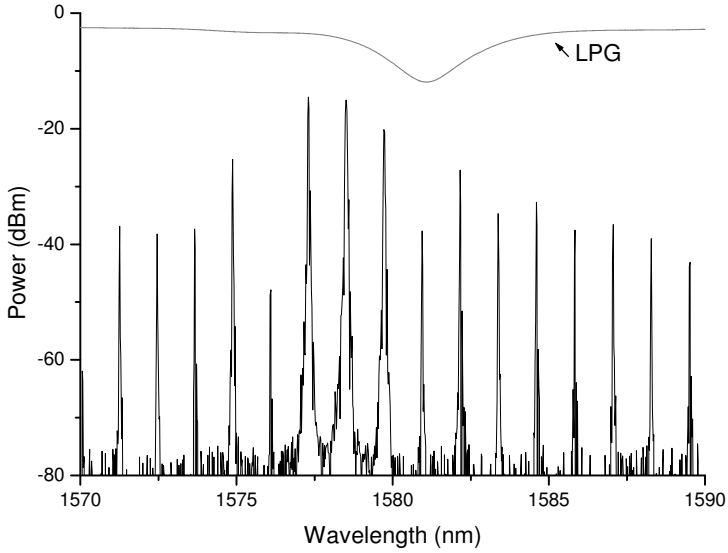

Figure 4.6: Reflection from B of the reflection of A transmitted through the long-period grating. The transmission spectra of the long period grating is also shown.

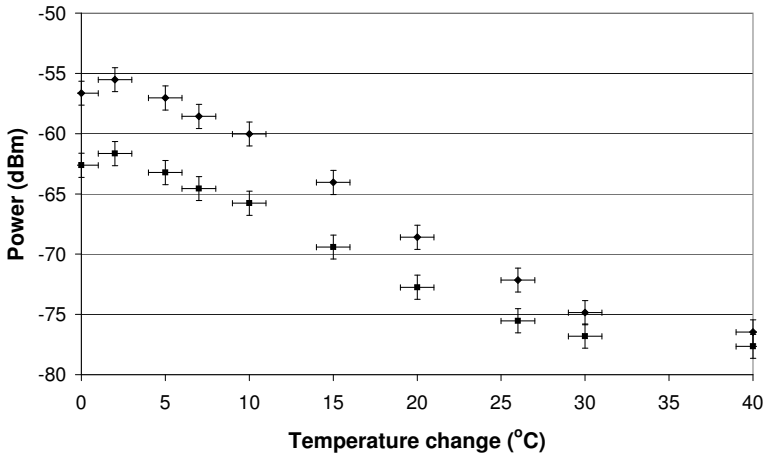

Figure 4.7: Reflection from B of the reflection of the LED from A measured with the detector as a function of temperature. The ♦ data is without the LPG and ■ it the data with the LPG inserted.

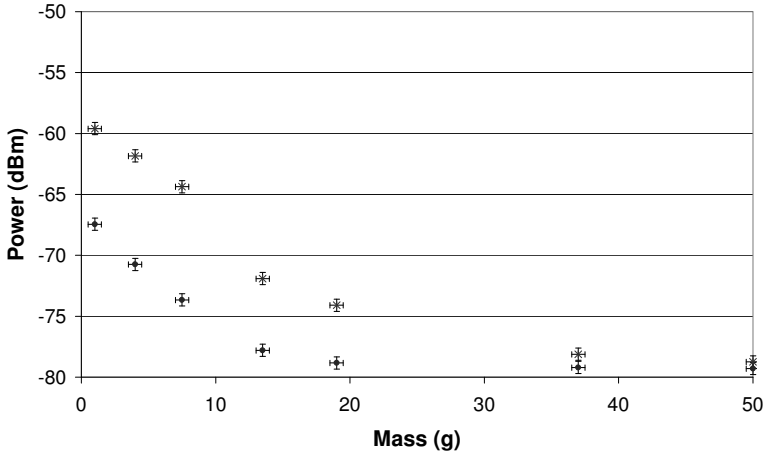

Figure 4.8: Reflection from B of the reflection of the LED from A measured with the detector as a function of the mass of the load. The ∗ data is without the LPG and • it the data with the LPG inserted.

load. The result is shown in figure 4.8 and it shows a dynamic range of 20 dB when the load is changed with 50 g. After this the displacement is so large that there is no reflection only a background noise. When the load is increased further the peaks will eventually overlap again. The maximal power is -59 dBm this time, since a circulator with a much higher insertion

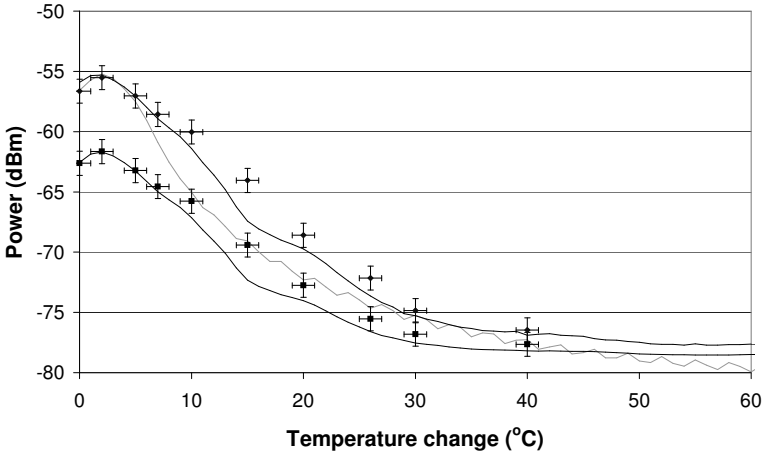

Figure 4.9: Simulations (gray curve) and measurements of power as a function of temperature in case I(♦) and case II (■). The black curves show the result calculated on the basis of the reflection spectrum.

loss was used for these measurements. In these measurements the power was first measured for case I as a function of the mass, and then in case II. This was done to decrease the loss from one measurement point to the next.

4.3 Simulations

Simulations of the behavior can be made by using the transfer matrix method described in section 2.4.1. To simulate the long-period grating a Gaussian dip is used, since calculation require a detailed knowledge of the refractive index in the core and cladding. The simulations of case I based on the data from table 4.1 and scaled with regards to the losses gives the behavior shown in figure 4.9 (gray curve) together with the measured data as a function of temperature. It is seen that the simulations based on the transfer matrix method is decreasing too fast. This is the case since the simulated reflection peaks are about 10-15 pm too narrow, which will decrease the overlap range.

To approach the real case it is possible to calculate the overlap based on the reflection spectra shown on figure 4.2. The results from these calculations are also shown on figure 4.9 (black curves), where a constant background contribution is added to represent the lower detection limit. It is seen that this behavior describes the data much better, but there is still

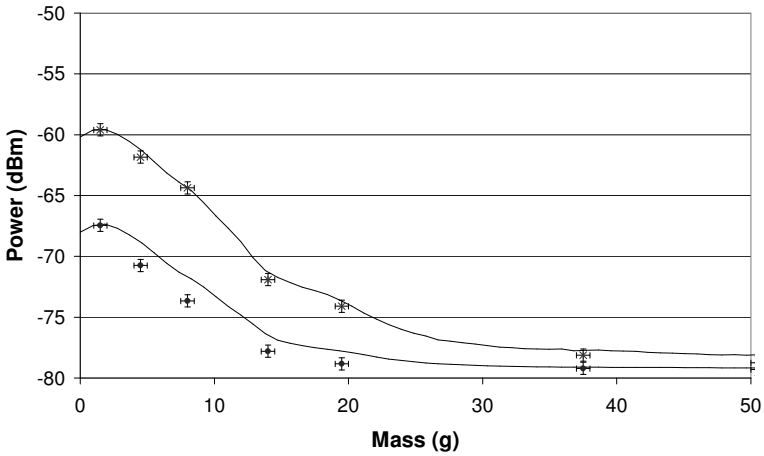

Figure 4.10: Power as a function of the load mass for case I (∗), case II (•) and simulations (black curve).

a bump, which is not resolved. One reason could be that the connector was cleaned and assembled better in this measurement.

The reflected power can also be calculated in the case where a load is applied to induce strain. The results are shown on figure 4.10 together with the measured values. It is seen that these results fit much better in case I, since the power was measured without changing the cables. For case II it seems that the long-period grating changes faster than expected. In these measurements the two grating were mounted in the same holder, so they are influenced by half the load. This gives a small uncertainty of the applied mass, but not so large that the difference in case II can be explained.

Measurements of the power when both temperature and strain is applied, shows that the overlap decreases very fast. This means that if the sensor is mounted in a material, and this induces some strain, then the measuring range decreases. To increase the tuning range, the reference grating can be strained to compensate for the difference in peak wavelength.

4.4 Conclusion

This chapter shows that it is possible to resolve temperature and strain since the sampled and long-period grating have different temperature and strain coefficients. To get the values of the temperature and strain, a routine that fits the data with a calculated power has to be written. In this case it is most accurate to apply the program used to calculate the overlap of the

measured reflection spectra. More work has to be done before the applied temperature and mass is calibrated correct and the simulation fits better.

To improve the measurements a switch can be used before the long-period grating, so the cables do not have to be changed, and thereby induce varying losses. Another way to increase the detection range is by increasing the detected power, since the detection limit is set by the background signal. One way to increase the detected power is by decreasing $\frac{z_1}{z_0}$, which will lead to an increase in the number of reflected peaks. The reduced length z_1 leads to a large increase in the total fluence, which is necessary to get a high maximal reflection. It would furthermore be advisable, to design the long-period grating and the sampled gratings to have wavelength response around the wavelengths, where the input source has its maximal value.

The advantage of this method is the possibility of measuring the change in temperature and strain with a detector instead of an optical spectrum analyzer.

Chapter 5

Molecular spectroscopy

5.1 Motivation

Erbium doped fiber lasers emit light in the 1.5 μm telecommunication band. In this range there are different molecules, such as C_2H_2, HCN, H_2S, CO and CO_2, which have vibration bands and combination bands, thus they can be studied with laser spectroscopy, if the fiber laser can be tuned. If the laser can also be modulated, the signal to noise ratio can be improved by synchronous detection. Furthermore the line center of an absorption line is an absolute frequency reference. If the fiber laser can be tuned and modulated, it is possible to stabilize the wavelength of this type of laser at the center of the absorption line, and thereby produce a wavelength standard. Acetylene has line strengths, which are relatively strong so that the necessary absorption can be obtained in short cells. DFM is interested in a stabilized fiber laser, since a wavelength standard in the telecommunication range around 1.5 μm is valuable for DWDM systems, where several wavelengths are used to increase the capacity of the optical network.

The content of this chapter is as follows. Molecule spectra are explained, and the selection rules for transitions in infrared spectroscopy are described in 5.2. Acetylene is given as an example in 5.2.2. One remarkable behavior of these spectra, is the fact that the line strength can vary for even and odd values of the angular momentum quantum number, as explained in section 5.2.3.

Absorption spectroscopy can be used to measure the molecular absorption lines, this method will be described in 5.3. One way to improve the signal-to-noise ratio is by frequency modulation and lock-in detection (section 5.3.1). This is also a way to provide a first or second harmonic signal

of the absorption coefficient, which is necessary for locking the laser wavelength to the center of an absorption line. The stability of a system can be investigated by calculating an Allan variance as described in section 5.3.2.

5.2 Near-infrared spectroscopy

Rotation or vibration of a molecule give rise to a lot of energy levels and therefore to many transitions. If the dipole moment of a molecule is non-zero, it can be studied with infrared spectroscopy. Combination bands, where the molecules make a transition to a state which is a combination of two vibration modes accompanied with a transition to different rotation levels, can be studied by near-infrared spectroscopy of molecules in the gas phase.

The total wave function ψ of a molecule is in the Born-Oppenheimer approximation given by

$$\psi = \psi_e \psi_v \psi_r \psi_{ns} \tag{5.1}$$

Where ψ_e, ψ_v, ψ_r and ψ_{ns} are the electronic, vibrational, rotational and nuclear spin wave functions respectively. The Born-Oppenheimer approximation is valid since the electron adjusts its motion fast to a change in the nuclear motion.

The behavior of the molecule can be approximated, by describing the rotation as a rigid motion. In this approximation the total angular momentum J is a good quantum number. Vibration of a molecule can be described as a harmonic oscillator, with energy levels given by

$$E_v = h\nu(v + 1/2) \tag{5.2}$$

where v is the vibrational quantum number and h is Plancks constant. $\nu = \frac{1}{2\pi}\left(\frac{k}{m}\right)^{1/2}$ is the classical vibration frequency, where m is the reduced mass and k is the force constant.
The total term value (E/hc) for both vibration and rotation is [57]

$$\frac{E}{hc} = \omega\left(v + \frac{1}{2}\right) - \omega x_e\left(v + \frac{1}{2}\right)^2 + B_v J(J+1) - D_v J^2(J+1)^2 \tag{5.3}$$

where $\omega = 1/\lambda$ is the classical vibration wave number, in the harmonic approximation, and x_e is the anharmonic contribution. $B_v = \frac{h}{8\pi^2 cI}$ is the rotational constant with a dimension of wave number, where $I = r^2\mu$ is the moment of inertia. A correction term to the assumption about a rigid motion, is the centrifugal distortion constant $D_v = \frac{4B_v^2}{\omega^2}$.

5.2.1 Selection rules for vibrational transitions

Not all transitions are allowed in the dipole approximation. For molecular spectroscopy group theory is very practical, since the selection rules apply for the point group. By investigating to which point group a molecule belongs, it is possible to determine which transitions are allowed in the dipole approximation, but it does not determine if the probability is zero. The lower the symmetry order is the higher is the number of allowed transitions. For a polyatomic molecule the vibrational transition intensity is proportional to $|R_v|^2$, where the vibrational transition moment is

$$\mathbf{R}_v = \int \psi_v'^* \mu \psi_v'' d\tau_v \tag{5.4}$$

and μ is the dipole moment. ψ_v' and ψ_v'' are the wave functions in the upper and lower vibrational state respectively.
The dipole moment is given by

$$\mu = \sum_i q_i \mathbf{r_i} \tag{5.5}$$

where q_i is the charge and $\mathbf{r_i}$ is the distance of the i′th particle.

The integral in equation 5.4 is only non-zero if the direct product of the representations of the wave functions and the electric dipole moment is the total symmetric species A, that is [57]

$$\Gamma(\psi_v') \times \Gamma(\mu) \times \Gamma(\psi_v'') = A \tag{5.6}$$

in the non degenerated case and

$$\Gamma(\psi_v') \times \Gamma(\mu) \times \Gamma(\psi_v'') \supset A \tag{5.7}$$

in the degenerated case, where the representation contains the totally symmetric species. μ is a vector, so it has the same symmetric species as the translation T in the same direction

$$\Gamma(\mu_x) = \Gamma(T_x),\ \Gamma(\mu_y) = \Gamma(T_y) \text{ and } \Gamma(\mu_z) = \Gamma(T_z) \tag{5.8}$$

Equation 5.6 and 5.7 can therefore be rewritten. If the lower state has $v = 0$ then $\Gamma(\psi_v'') = A$, and

$$\Gamma(\psi_v') \times \Gamma(T_x) = A \tag{5.9}$$

and/or

$$\Gamma(\psi_v') \times \Gamma(T_y) = A \tag{5.10}$$

and/or

$$\Gamma(\psi_v') \times \Gamma(T_z) = A \tag{5.11}$$

It is therefore necessary to determine which point group a molecule belongs to, and investigate the translation symmetric species in the character table.

The vibrational selection rule gives $v = \pm 1$. The rotation selection rule for a linear molecule is $\Delta J = \pm 1$ for a $\Sigma - \Sigma$ transition.[1] This gives two branches in the spectrum. The one with $\Delta J = 1$ is called the R branch and the one with $\Delta J = -1$ is called the P branch. P(J) refers to the J value of the lower state. For a $\Pi - \Sigma$ transition the selection rule is $\Delta J = 0, \pm 1$. In this case each J level in the upper state is split due to Coriolis force, which modifies the term value expression with $\pm \frac{q_i}{2} J(J+1)$, q_i determines the magnitude of the splitting. To determine which component of the split levels is involved in the R or P branches, it is necessary to apply the parity selection rule, which says that transitions which changes the parity are allowed. When $\Delta J = 0$ is allowed there is a third branch called the Q branch. This branch is in the center of the spectrum.

5.2.2 Acetylene

Acetylene belongs to the $D_{\infty h}$ point group (shown in appendix A). It has combination bands in the 1.5 μm region and is therefore of interest. The vibrations are shown in figure 5.1 and listed in table 5.1. The ν_4 and ν_5 vibrations are double degenerated, and they have an angular momentum which can be ± 1. The notation used for the symmetric species belonging to the $D_{\infty h}$ is as follows: The Σ and Π vibrational states have an angular momentum of 0 and 1 respectively. g and u indicates if the wave function is symmetric or antisymmetric to inversion through the center of the molecule. + or - indicates if the wave function is symmetric or antisymmetric to reflection across any plane containing the internuclear axis. The signs are only used to Σ species since Π is double degenerated.

The representation of the combination state $\nu_1 + \nu_3$ can be found by the direct product of

$$\Gamma(\psi_{\nu_1+\nu_3}) = \Gamma(\psi_{\nu_1}) \times \Gamma(\psi_{\nu_3}) = \Sigma_g^+ \times \Sigma_u^+ = \Sigma_u^+ \tag{5.12}$$

because $\Gamma(\psi_{\nu_3}) = \Sigma_u^+ = T_z$ the direct product is:

$$\Gamma(\psi_{\nu_1+\nu_3}) \times \Gamma(\mu) \times \Gamma(\psi_{v=0}) = \Sigma_u^+ \times \Sigma_u^+ \times \Sigma_g^+ = \Sigma_g^+ \tag{5.13}$$

[1] The notation for linear molecules is a bit different from the other point groups, in this case Σ_g^+ =A is the totally symmetric species.

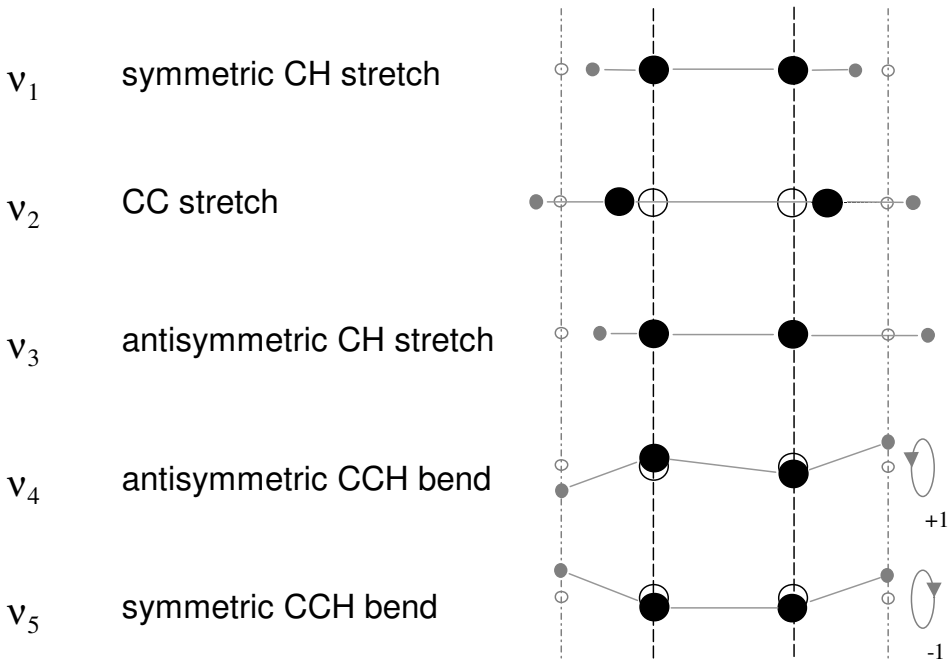

Figure 5.1: The normal modes of vibration of acetylene. The ±1 refers to the angular momentum of the vibration. The unfilled circles represent the equilibrium position.

Name	Vibration	Wavenumber /cm^{-1}	Symmetric species	Infrared active
ν_1	symmetric CH stretch	3374	Σ_g^+	no
ν_2	CC stretch	1974	Σ_g^+	no
ν_3	antisymmetric CH stretch	3287	Σ_u^+	yes
ν_4	antisymmetric CCH bend	612	Π_g	no
ν_5	symmetric CCH bend	729	Π_u	yes

Table 5.1: Properties of the vibration modes of 12-acetylene.[57]

Since Σ_g^+ is the total symmetric species, this combination state is infrared active, due to the change in dipole moment. For the combination state

$\nu_1 + \nu_2 + \nu_4 + \nu_5$ the representation is

$$\begin{aligned}\Gamma(\psi_{\nu_1+\nu_2+\nu_4+\nu_5}) &= \Gamma(\psi_{\nu_1}) \times \Gamma(\psi_{\nu_2}) \times \Gamma(\psi_{\nu_4}) \times \Gamma(\psi_{\nu_5}) \\ &= \Sigma_g^+ \times \Sigma_g^+ \times \Pi_g \times \Pi_u \\ &= \Pi_g \times \Pi_u \\ &= \Delta_u + \Sigma_u^+ + \Sigma_u^- \end{aligned} \tag{5.14}$$

Since ν_4 and ν_5 are degenerated vibration modes equation 5.7 has to be satisfied. The direct product is

$$\begin{aligned}\Gamma(\psi_{\nu_1+\nu_2+\nu_4+\nu_5}) \times \Gamma(\mu) \times \Gamma(\psi_{v=0}) &= (\Delta_u + \Sigma_u^+ + \Sigma_u^-) \times \Sigma_u^+ \times \Sigma_g^+ \\ &= \Sigma_g^+ + \Delta_g + \Sigma_g^- \end{aligned} \tag{5.15}$$

This combination state is also infrared active. The two combination bands can therefore be investigated by absorption spectroscopy in the near-infrared region.

5.2.3 Intensity variation in the spectrum.

For linear polyatomic molecules, which have an even number of identical nuclei with nuclear spin quantum number I=n+1/2 (n is zero or an integer), the total wave function is antisymmetric under exchange of two identical nuclei with equal distance to the center.

The infrared spectra for $^{12}C_2H_2$ has an intensity difference of 3:1 between odd and even values of J, since the rotation levels are symmetric or antisymmetric to nuclear exchange. For ^{12}C the nuclear spin quantum number I=0 and I=1/2 for H. The difference in intensity is due to the two equivalent protons, which are exchanged on rotation of the molecule through 180 degrees. There are tree symmetric and one antisymmetric nuclear spin wave functions, which give the nuclear statistical weights 1 to 3 for even and odd J respectively.

For $^{13}C_2H_2$ both ^{13}C and H have I=1/2, so they are Fermions and the total wave function should be antisymmetric under exchange of two equivalent nucleons with equal distance from the center. Since $m_I(H) = \pm 1/2$ and $m_I(C) = \pm 1/2$ it can be shown that there are 10 symmetric and 6 antisymmetric nuclear spin wave functions, which gives an intensity alternation between even and odd J that is 5 to 3.

For an isotope with a larger reduced mass the band is displaced to a lower wave number. The bands for $^{13}C_2H_2$ are therefore shifted to longer wavelengths.

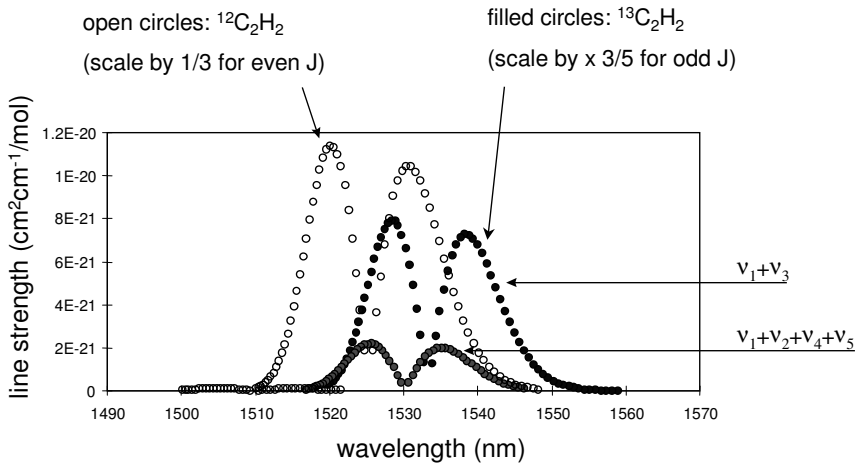

Figure 5.2: The line strength for $^{12}C_2H_2$ and $^{13}C_2H_2$ [58].

All these effect are illustrated on figure 5.2, which shows the line strength[2] as a function of wavelength for $^{12}C_2H_2$ and $^{13}C_2H_2$.

5.3 Absorption spectroscopy

A way to investigate molecular vibrations is by absorption spectroscopy. In absorption spectroscopy the spectral intensity I_T is normally measured, to determine the absorption coefficient $\alpha(\omega)$ given by Beer′s law,

$$I_T(\omega, L) = I_0 \cdot e^{-\alpha(\omega)L} \tag{5.16}$$

where L is the absorption path length, and I_0 is the initial intensity. The absorbance is given by $\alpha L = \ln(-I_T/I_0)$. For small absorbancies $\alpha L << 1$, the exponential function can therefore be approximated by

$$e^{-\alpha(\omega)L} \simeq 1 - \alpha(\omega)L \tag{5.17}$$

so

$$I_T(\omega) \simeq I_0(1 - \alpha(\omega)L) \tag{5.18}$$

From a reference beam $I_R = I_0$ the absorption coefficient is given by

$$\alpha(\omega) = \frac{I_R - I_T(\omega)}{I_R L} \tag{5.19}$$

[2]The Hitran database uses the notation cm/mol for line strength. The correct notation is cm^{2}cm^{-1}/mol, where cm^{-1} is the unit for wave-number, and mol is number of molecules.

The reference beam can be produced by a beam splitter with a known reflectivity.

For the transition $|i\rangle \rightarrow |k\rangle$ with absorption cross section σ_{ik} the absorption coefficient $\alpha_{ik}(\omega)$ is determined by

$$\alpha_{ik}(\omega) = [N_i - \frac{g_i}{g_k} N_k]\sigma_{ik}(\omega) = \Delta N \sigma_{ik}(\omega) = \Delta N S g(\nu - \nu_0) \tag{5.20}$$

where N_i is the density of the absorbing molecules and N_k the density of molecules in the upper state, g_i and g_k are the degeneracy of the levels, S is the line strength, and g is the line function . For a line which is both Doppler and pressure broadened, the line profile is described by a Voigt profile [59].

In the near-infrared region $N_k \sim 0$, so the minimum detectable density N_i is

$$N_i \geq \frac{\Delta I}{\mathrm{I}_0 L \sigma_{ik}} \tag{5.21}$$

It is possible to get a high detection sensitivity, if $L\sigma_{ik}$ is large, or the minimum detectable value $\Delta I/\mathrm{I}_0$ is as small as possible. For small αL the ΔI is small compared with the signal. When detector noise and intensity fluctuations sets the limit, the minimum detectable absorbance is generally $\frac{\Delta I}{I} \geq 10^{-4} - 10^{-5}$.

Another way of finding the density is by the ideal gas law, which relates the pressure and the density of molecules, N,:

$$P = N k_B T \tag{5.22}$$

where T is the temperature, $k_B = 1.38 \cdot 10^{-23}$ J/K is Boltzmanns constant.

This relates the minimal detectable absorption with the pressure and the length by

$$\frac{\Delta I}{I} = N_i L S g(\nu - \nu_0) = S g(\nu - \nu_0) \frac{LP}{k_B T} \tag{5.23}$$

Since there is a pressure broadening in a gas cell, it is better to have a long cell than a high pressure.

5.3.1 Frequency modulation

The sensitivity can be increased by use of frequency modulation and synchronous detection. Here the laser output frequency ω_L is modulated at the modulation frequency f. The laser frequency ω_L is therefore tuned periodically from ω_L to $\omega_L \pm \Delta\omega_L$, and ω_L is tuned linearly through the absorption

spectrum. The difference $\mathrm{I}_T(\omega_L) - \mathrm{I}_T(\omega_L + \Delta\omega_L)$ is detected with a lock-in amplifier, which is set to the modulation frequency. For small modulations $\Delta\omega_L$, I_T can be Taylor expanded so the difference is

$$\mathrm{I}_T(\omega_L + \Delta\omega_L) - \mathrm{I}_T(\omega_L) = \frac{dI_T}{d\omega}\Delta\omega_L + \frac{1}{2!}\frac{d^2\mathrm{I}_T}{d\omega^2}\Delta\omega_L^2 + ... \tag{5.24}$$

If I_R is independent of ω

$$\frac{d\alpha(\omega)}{d\omega} = -\frac{1}{I_R L}\frac{d\mathrm{I}_T}{d\omega} \tag{5.25}$$

If a laser frequency ω_L is modulated with an angular frequency Ω, the frequency can be written as

$$\omega_L = \omega_0 + a\sin\Omega t \tag{5.26}$$

In this case equation 5.24 can be written as [59]

$$\mathrm{I}_T(\omega_L) = \mathrm{I}_T(\omega_0) + \sum_n \frac{a^n}{n!}\sin^n\Omega t \ \left(\frac{d^n\mathrm{I}_T}{d\omega^n}\right)_{\omega_0} \tag{5.27}$$

For $\alpha L << 1$ equation 5.25 gives

$$\left(\frac{d^n\mathrm{I}_T}{d\omega^n}\right)_{\omega_0} = -\mathrm{I}_0 L\left(\frac{d^n\alpha(\omega)}{d\omega^n}\right)_{\omega_0} \tag{5.28}$$

The $\sin^n(\Omega t)$ terms can be written as sin or cos terms. For small modulations ($a/\omega_0 << 1$) the signal, $\mathrm{S}(n\Omega)$ behind a lock-in amplifier tuned to the frequency $n\Omega$ is [59]

$$\mathrm{S}(n\Omega) = \left(\frac{\mathrm{I}_T(\omega_L) - \mathrm{I}_T(\omega_0)}{\mathrm{I}_0}\right)_{n\Omega} = aL\begin{cases} b_n\sin(n\Omega t) & n = 2m+1 \\ c_n\sin(n\Omega t) & n = 2m \end{cases}$$

The signals for the first three derivatives of the absorption coefficient $\alpha(\omega)$ are

$$S(\Omega) = -aL\frac{d\alpha}{d\omega}\sin(\Omega t) \tag{5.29}$$

$$S(2\Omega) = \frac{a^2 L}{4}\frac{d^2\alpha}{d\omega^2}\cos(2\Omega t) \tag{5.30}$$

$$S(3\Omega) = \frac{a^3 L}{24}\frac{d^3\alpha}{d\omega^3}\sin(3\Omega t) \tag{5.31}$$

It is therefore possible (with phase sensitive detection) to measure only a small frequency interval centered at the modulation frequency Ω. This

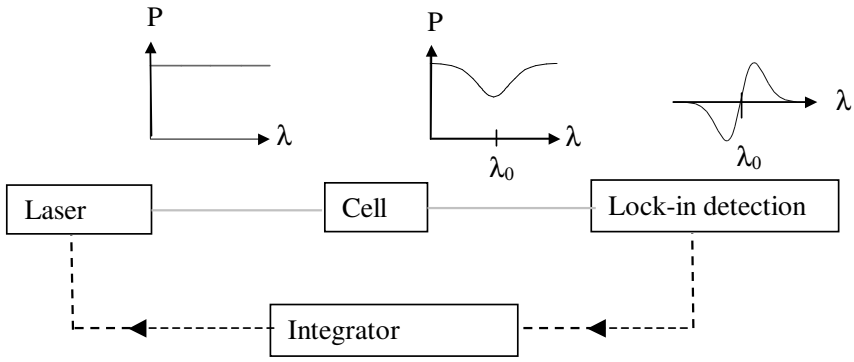

Figure 5.3: Setup for absorption measurements. The light from the laser is illustrated in the first insert. After the cell there is an absorption dip, illustrated in the second insert. The first harmonic of the absorption spectrum is resolved by the lock-in detection, which is shown in the third insert. The dashed line indicates a servo circuit to lock the laser at the line center.

reduces the loss from frequency independent absorption from the cell and the background noise, and it increases the signal to noise ratio.

The setup for absorption measurements with synchronous detection is shown in figure 5.3. The lock-in amplifier gives the first harmonic of the absorption coefficient, and it becomes zero at line center. If the lock-in signal is integrated and sent to the laser, the wavelength can ce locked at the line center. The integrator enables the error signal to become zero at line center. Figure 5.3 also shows the servo circuit with a dashed line.

5.3.2 Allan variance

A way to study the stability of a laser is to calculate an Allan variance [60]. Here it is the change from one measurement point to the next which is investigated. If the frequency ν is measured and $Y_i = \frac{\nu_i}{\nu_0}$ is the normalized frequency averaged over the measurement time τ, then the Allan variance is given by

$$\sigma_y^2(\tau) = \frac{\sum_{i=1}^{N-1} |\overline{Y}_{i+1} - \overline{Y}_i|^2}{2(N-1)} \tag{5.32}$$

The time stability can be investigated by changing the measurement time. The Allan variance is plotted in a double log- plot with $\log(\sigma)$ as a function of $\log(\tau)$. In the short time domain there can be a $\tau^{-1/2}$ dependency, due to white noise which is independent of frequency. A τ^1 behavior is due to drift in the system.

Chapter 6

Wavelength modulation and tuning based on piezoelectric transducers

Single-mode lasers with narrow line width are attractive for applications such as sensor systems, laser spectroscopy or wavelength standards in telecommunication. As a spin off from telecommunication, small robust semiconductor lasers oscillating in the infrared region, are available. A Fabry-Perot semiconductor laser is multi-mode, but it can be made single-mode by using an external diffraction grating for optical feedback. Such a laser called an extended cavity laser (ECL), can be tuned single-mode up to ~ 100 nm by rotating the grating. If the grating is dithered by a piezo, it can be used for frequency modulation up to a few kHz. A limitation of the ECL is the cost. An alternative to the ECL is the semiconductor DFB laser. It can be tuned over 3 nm by changing the temperature, and modulated up to the GHz range by the injection current. A drawback is the price of non standard wavelengths. Another possibility is a DFB fiber laser, where the wavelength can be chosen in the range 1525 nm to 1610 nm. An advantage of the fiber laser compared to the DFB semiconductor laser is, that the wavelength selective process is independent of the gain.

A laser, which can be both tuned and modulated, can be used for gas monitoring, and it can also be wavelength stabilized. The DFB fiber laser can be tuned either by strain or temperature as shown in equation 2.6 and 2.11. One way to strain modulate a fiber laser is by mounting it with piezoelectric transducer (PZT) as demonstrated by Wetjen *et al* [33]. In this chapter strain modulation and tuning is investigated, and temperature modulation and tuning is investigated in chapter 7. In section 6.4 an exam-

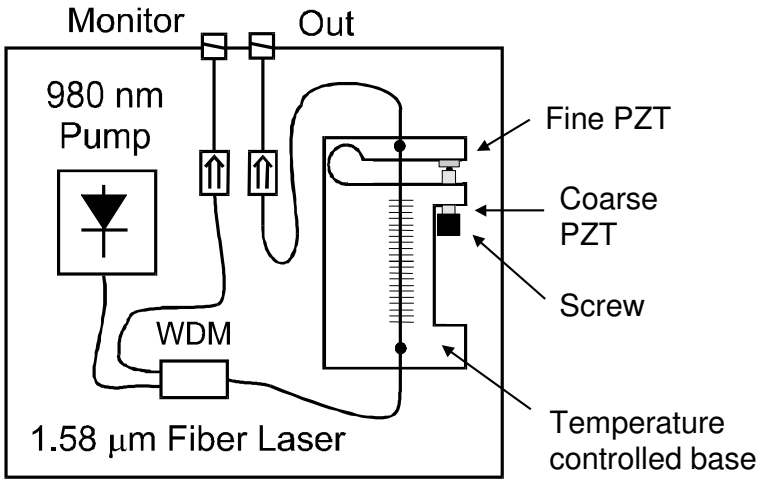

Figure 6.1: The aluminum mount where the fiber laser is glued with epoxy just outside the grating. The fiber laser can be strained by a screw, a coarse and a fine piezoelectric transducer (PZT).

ple of absorption measurement of CO_2 is investigated and compared with the spectrum measured with an ECL and a DFB semiconductor laser. In section 6.4.1 the fiber laser is locked to an absorption line, and the stability is investigated.

6.1 Experiment

The Er^{3+}-Yb^{3+} doped DFB fiber laser was produced by Koheras with a wavelength of 1578 nm [1]. When the fiber laser was pumped with 980 nm radiation from a pump diode, the threshold was at a pump power of 40 mW. When the pump power was 100 mW the fiber laser gave 1.3 mW.

The fiber laser was glued with epoxy just outside the grating on to an aluminum mount, illustrated on figure 6.1. On the mount there are two piezoelectric transducers (PZT) and one lead screw to strain the fiber. The aluminum mount is temperature controlled to ensure passive stability. The optical output from the fiber laser was characterized by a wavemeter with 7 digit resolution, a scanning Fabry-Perot interferometer with a free spectral range of 2 GHz, and a fiber coupled power meter.

[1] Se www.koheras.dk

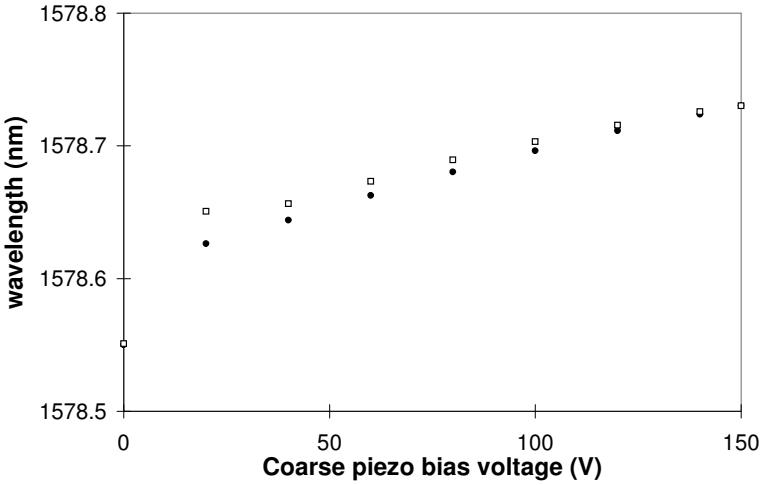

Figure 6.2: Wavelength change as a function of the voltage on the coarse PZT. The circular data points are measured for increasing voltage, where the squares are measured for decreasing voltages.

6.2 Tuning of the wavelength

The lead screw can be tuned by 6.8 nm/mm referred to the displacement of the screw. To avoid damage of the fiber the tuning was limited to 2.7 nm. This corresponds to a relative length change of 0.0023. The strain-optic coefficient lowers the tuning, which would have been 3.6 nm if only the length was changed. The temperature of the aluminum mount can tune the wavelength linearly in the range 20-30 ^{0}C with 32.6 pm/^{0}C. The large tuning coefficient is due to the thermal length expansion of the aluminum mount, which has a linear thermal expansion coefficient of $23{\cdot}10^{-6}$ C^{-1}. The lead screw and the temperature were chosen, so the absorption line under investigation was in the middle of the coarse PZT scan. So the start wavelength was 1578.55 nm. The coarse PZT has a nominal displacement of 15 μm at 150 V, which gives a maximal wavelength tuning of 0.12 nm. The fine PZT has a displacement of 0.9 μm at 150 V and a maximal wavelength change of 5.5 pm. Figure 6.2 shows the wavelength for increasing (•) and decreasing (□) voltage on the coarse PZT. It is seen that the wavelength tuning has a hysteresis effect. When the increasing voltage was above $\sim$ 25V the wavelength changed linearly with 0.86 pm/V, until the voltage was above 120 V. On the way down the fiber laser became multi-mode, which gave a poor wavelength determination from about 60 V and down. The fiber laser was multi-mode in some limit cases and otherwise it was

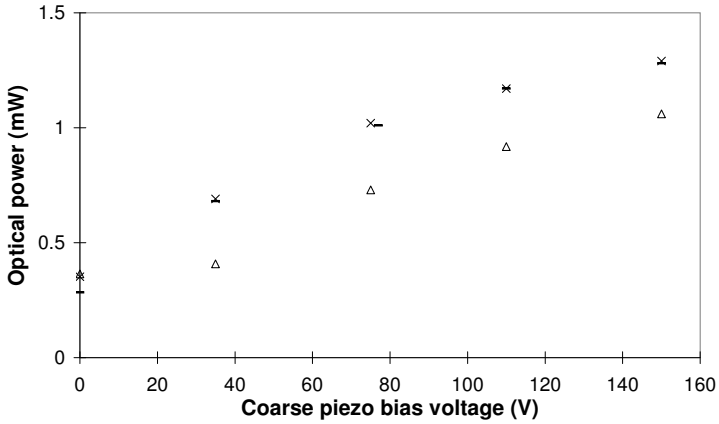

Figure 6.3: The optical output power as a function of the voltage on the coarse PZT for a pump power of 60 mW for different temperatures 20 ^{0}C (-), 24 ^{0}C ($\times$) and 30 ^{0}C ($\triangle$).

single-mode.

When the fiber laser was strained the output power increased, as shown on figure 6.3 for 60 mW pump power with different temperatures of the mount. It is seen, that the power increases to more than the double value, when a voltage is applied. The optical output depends also on the temperature, since the power decreased for 30 ^{0}C. The large change in power is probably due to the mounting, since it is very critical. This has not been confirmed, since DFM only has one mount.

6.3 Modulation

The PZT can also be used to modulate the wavelength. The frequency response was investigated with the scanning Fabry-Perot interferometer. Figure 6.4 shows the normalized frequency response, which had a uniform fall off until applied frequencies about 2 kHz. After this several mechanical resonances were observed. This measurement was done by H. Simonsen.

The large power change shown in figure 6.3 can give rise to a large amplitude modulation. The effect can be investigated by observing the DC and AC parts in the detector signal. By applying different modulations on the fine PZT for different voltages on the coarse PZT, it is possible to investigate the relative amplitude modulation compared to the DC signal, as shown in figure 6.5 for an applied frequency of 314 Hz. The DC voltage of the fine PZT was 75 V, to be in the middle of the voltage range. The

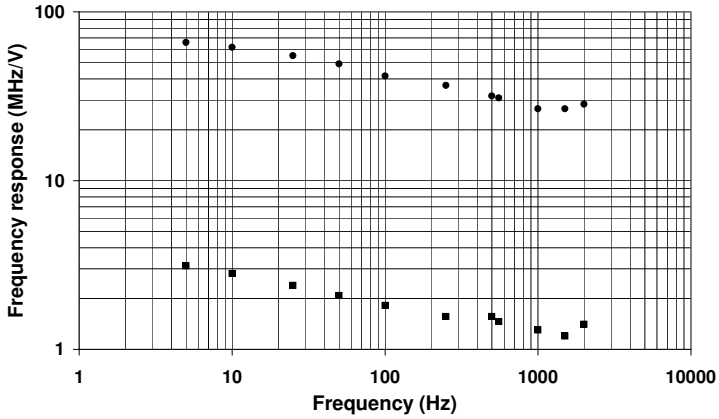

Figure 6.4: Frequency response of the coarse PZT (●) and the fine PZT (■).[37]

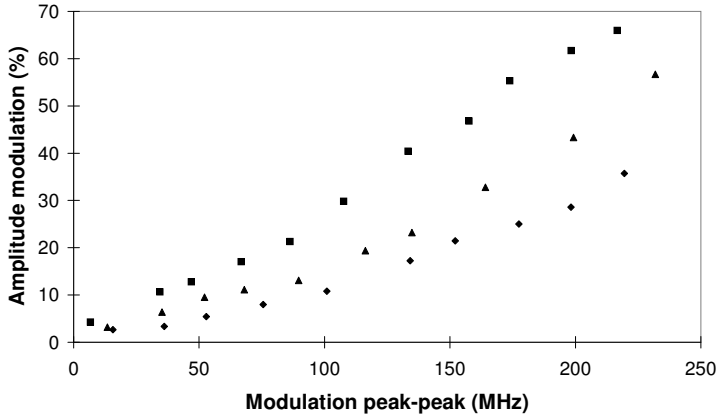

Figure 6.5: Relative amplitude modulation, when the fine PZT is set at 75 V and modulated at 314 Hz. Voltages on the coarse PZT: 40 V (■), 75(▲), 150 V (♦)

frequency modulation was calculated from the fine PZT voltage and the frequency response for 314 Hz (se figure 6.4), which was $\sim$ 1.5 MHz/V. It is seen that the relative amplitude modulation decreases for increasing voltages on the coarse PZT. If it is the coarse PZT which is modulated, the result is as shown in figure 6.6. It is seen that the relative amplitude modulation decreases for increasing voltage on the coarse PZT. In the following measurements it is the fine PZT which is used to modulate the wavelength.

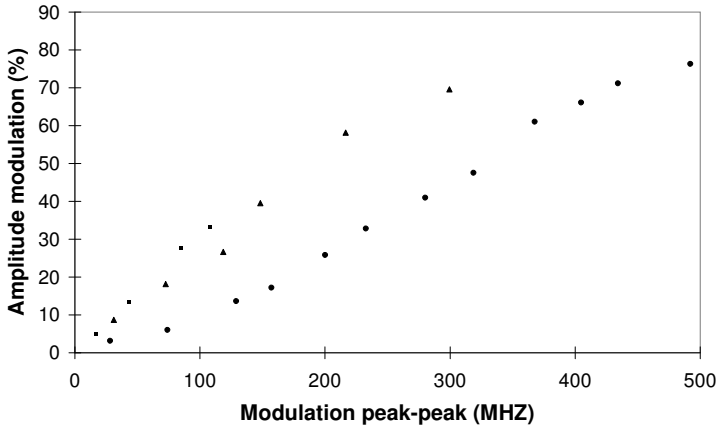

Figure 6.6: Relative amplitude modulation when the fine PZT is set at 75 V, and the coarse PZT is modulated at 314 Hz. Voltages on the coarse PZT: 35 V (■), 75(▲), 100 V (●)

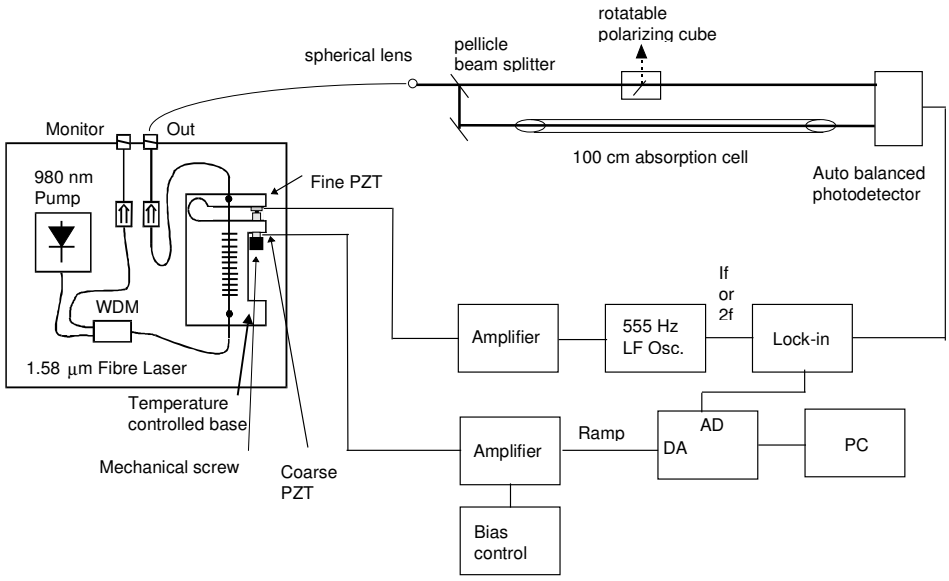

Figure 6.7: Setup for absorbance measurements.

6.4 Absorbance measurements

Since the fiber laser can be tuned by the coarse PZT and modulated by the fine PZT, it can be used for absorbance measurements. The setup for

measuring absorbance is shown in figure 6.7, where the output from the fiber laser is collimated by a spherical lens, and split by a pellicle beam splitter. One beam can be attenuated by a rotatable polarizing cube to provide the right amount of power in the reference beam. The other beam is sent through a gas cell with windows at the Brewster angle. The detector is a balanced detector, which gives the optimal output for the relationship between the reference and the signal of 2:1.

CO_2 can vibrate in 3 modes, where ν_1 is the symmetric CO stretching, and ν_3 is the antisymmetric stretch. The ν_2 is the degenerated bend. The fiber laser was strain modulated at 555 Hz, and the first or second harmonic was recovered by the lock-in amplifier. The gas cell was 1 m and contained CO_2. Figure 6.8 shows the P16 line of the $22^01 - 00^00$ combination band of CO_2 in the wavelength range 1578.63 nm to 1578.73 nm at pressures of 5, 50, 100, and 200 mbar, for a modulation amplitude of 190 MHz.

The notation 22^01 means that it is the $2\nu_1+2\nu_2+1\nu_3$ combination state. The P16 line at 1578.665 nm has a line strength of $1.557{\cdot}10^{-23}$ $\mathrm{cm^2cm^{-1}/mol}$ and a self broadening parameter of 2.96 MHz/mbar [61]. It is seen, that even though the absorbance is increased at higher pressures, the self broadening makes the first harmonic signal decrease and broaden. It is therefore at pressures around 50 mbar, that the first harmonic signal is optimized.

To investigate how the shape of P16 at 1578.665 nm is resolved, when the fiber laser is used to measure the second harmonic signal, it is compared with the one measured with an ECL. Figure 6.9 shows the second harmonic spectra of P16 measured with a) an ECL modulated at 313 Hz with piezo modulation of the grating, and c) the fiber laser modulated with 555 Hz respectively. Since the P12 line has a line strength of $1.657\cdot\ 10^{-23}$ cm/mol and a collision broadening parameter of 3.05 MHz/mbar [61], it has characteristics similar to the P16 line. The spectrum recorded of P12 (1572.992 nm) with a semiconductor DFB laser with a current modulation at 313 Hz (figure 6.9b), can therefore be compared with the spectrums of the P16 line. In all three cases the modulation depth was chosen to maximize the second harmonic signal, corresponding to a modulation depth $b \equiv \nu_m/\Delta\nu \approx 3$, where ν_m is the modulation amplitude, and $\Delta\nu$ is the HWHM of the line width [62].

The qualitative difference between the three line profiles is a consequence of amplitude modulation. Modulation of the ECL grating yields essentially a pure wavelength modulation and therefore a symmetric second harmonic profile. In the limit of low modulation depth the profile is proportional to the second derivative of the Voigt line profile. In this case the line is strongly over-modulated in order to optimize the signal-to-noise

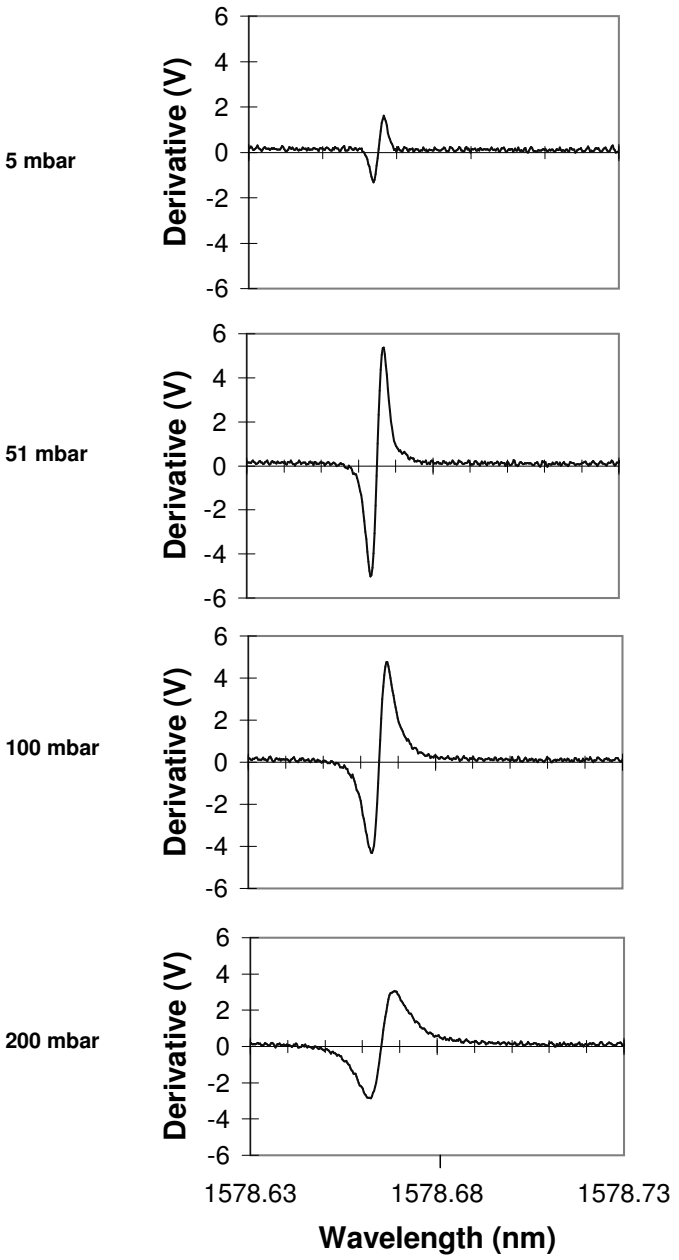

Figure 6.8: The first harmonic spectrum for different pressures as a function of wavelength.

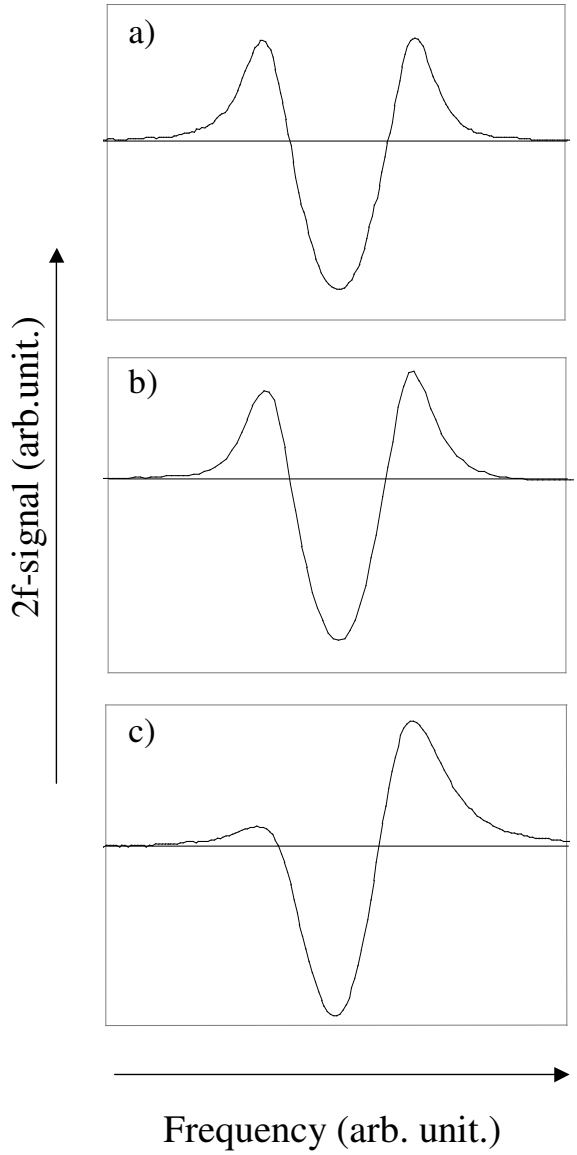

Figure 6.9: The second harmonic spectra of CO_2 recorded with an ECL(a), a semiconductor DFB laser (b) and a fiber laser (c). a) The ECL New Focus 6262 is modulated at 313 Hz and scanned through the P16 at 1578.665 nm. b) The semiconductor DFB laser from Sensors Unlimited is modulated at 313 Hz and scanned through the P12 line at 1572.992 nm. c)The fiber DFB laser from Koheras was modulated at 555 Hz and scanned through the P16 line. The frequency increases to the right.

ratio, which gives a small asymmetry. For the semiconductor DFB laser modulation of the current will change both the wavelength and the amplitude, and as shown in reference [62] this leads to the asymmetry observed in figure 6.9b. Strain modulation of the fiber laser leads to an amplitude modulation which is larger than for the semiconductor DFB laser, and the asymmetry is correspondingly stronger.

The signal-to-noise ratio corresponded in all three cases to a minimum detectable absorbance of $1.5 \cdot 10^{-4}$, limited by low frequency background variations.

The absorbance of the P16 line can be calculated as follows. The Voigt line profile can be calculated to $g = 26.2\ (\mathrm{cm}^{-1})^{-1}$. For the CO_2 line P16 with a line strength of $1.6 \cdot 10^{-23}\ \mathrm{cm}^2\mathrm{cm}^{-1}/\mathrm{mol}$, in a gas cell with a length of 1 m with a pressure of 100 mbar, the absorbance is

$$\begin{aligned} \alpha L &= \frac{P}{kT} \cdot S \cdot g \cdot L \\ &= \frac{10000 \cdot 10^{-6}}{1.38 \cdot 10^{-23} \cdot 296} \cdot 1.6 \cdot 10^{-23} \cdot 26.2 \cdot 100 \\ &= 10.3 \cdot 10^{-4} \cdot 100 = 0.103 \end{aligned} \tag{6.1}$$

This means that about 10.3 % is absorbed in the 1 m gas cell at a pressure of 100 mbar. A direct measurement of the absorbance yielded 0.109.

This example was performed on a known gas content. If a gas in air is to be measured, the wavelength shall be chosen carefully, since H_2O has many absorption lines. Otherwise it might not be the wanted gas which is detected. If the gas content is very low a long absorption path can be necessary. This can be done by multiple reflections between two mirrors.

6.4.1 Locking of the laser

The output from a laser can have a drift in time for example due to temperature fluctuations. A fiber laser, which can be tuned and modulated, can also be stabilized by locking the wavelength to an absorption line. It requires that an error signal can be feed back to the laser to adjust the wavelength. This is done the following way: First the wavelength is chosen close to the absorption line. The detector signal is sent to the lock-in amplifier, to get a first harmonic signal. The signal depends on how far the optical wavelength is compared to the line center, where the error signal is zero. The error signal is sent to an integrator, which integrates the error signal to return the signal to zero at line center, if the phase on the lock-in amplifier is chosen correctly. The integrator can also amplify the signal, if a larger response is needed. To be able to lock the laser, the sensitivities

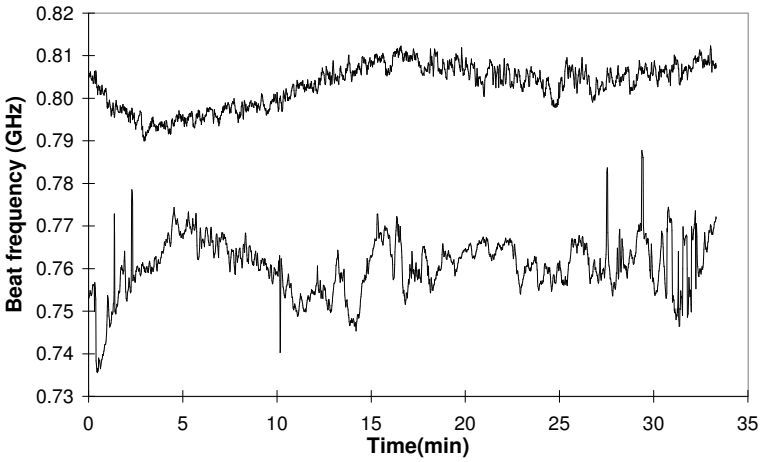

Figure 6.10: The beat signal between an ECL and a fiber DFB laser when the ECL is free and the fiber laser is locked (upper) and when the fiber laser is free and the ECL is locked (lower).

and time constants has to be chosen carefully. If not, it is possible to get oscillations in the feedback loop due to overshoot of the response. The time constant of the lock-in amplifier is set to be a few periods of the applied modulation frequency.

The stability of the fiber laser can be investigated by measuring the beat signal between the modulated fiber laser and an ECL. In this case the two signals are overlapped by using a 3 dB coupler. The beat signal is detected by a fast detector, and the signal is sent to a spectrum analyzer. It is not possible to measure the beat frequency if both lasers are locked, since the total width of the beat frequency becomes too large for the detector. An example where the upper curve shows the case where the fiber laser is locked, and the ECL is free, is given in figure 6.10. The lower curve shows the opposite case. It is seen, that the most stable result is when the ECL is free, but it has a drift on the minute scale.

A way to investigate the stability is by making an Allan variance (see section 5.3.2). Investigations of the stability was done by H. Simonsen[37]. In this case he locked the fiber laser with the first harmonic signal and the ECL with the second harmonic signal of the same absorption line, to get a small difference in wavelength. He found that the stability was $\sim$ 2 MHz for integration times less than 20 s. A stabilized fiber laser can be used as a wavelength standard in the 1.5 μm telecommunication band. The found stability is sufficient to meet the requirements of telecommunication [63],

where the minimum channel widths are 50 GHz.

6.5 Conclusion

A DFB fiber laser can be tuned and modulated by straining the fiber. By using a fine PZT to modulate and a coarse PZT to tune the wavelength it is possible to make absorption measurements as illustrated by the P16 line in CO_2. The second harmonic spectrum has more asymmetry than the spectrum measured with an ECL. The reason is the large increase in power when the fiber is strained. In some limit cases the fiber laser was observed to be multi-mode. The laser only became double mode, when the PZT was near the limit for the operation. When the optimal gas pressure and amplitude of the frequency modulation was found, it was possible to lock the laser with a stability of better than 2 MHz [37].

Chapter 7

Temperature modulation and tuning of DFB fiber lasers

7.1 Introduction

The wavelength response of a grating depends on the temperature. Gratings which can be adjusted or modified by resistive heating of a thin film deposited on the fiber, are gaining increasing importance as components in optical communication systems [36]. A homogeneous temperature profile enables fine tuning of the reflection maximum, to the wavelengths required in dense wavelength division multiplexing systems (DWDM) [64]. An inhomogeneous film which produces a constant temperature gradient along the grating, induce a controllable chirp, which may be used for dispersion compensation [65]. Films with periodically varying thickness can induce superstructures in the grating [66].

In this chapter thermal tuning and modulation of the laser wavelength is described. The temperature (and hence the wavelength) is controlled through resistive heating of a thin metal film on the fiber laser. In section 7.3 a metal film produced by chemical deposition of silver is analyzed [67], and in section 7.4 a metal film produced by electron beam evaporation is investigated. A fiber laser, which can be both tuned and modulated, can be used for absorption measurements, or it can be stabilized to a molecular absorption line. In section 7.6 examples of gas sensing will be given, and in section 7.7 investigation of the laser stability (when it is locked to an absorption line) is carried out. First the theory behind the heat flow is given in section 7.2.

7.2 Theory of temperature modulation

A theoretical analysis of the heat flow, in homogeneous as well as inhomogeneous metal films, has been given by Rogers *et al* [68] and Salamon *et al* [69]. Here is given a theoretical analysis of the heat flow for a homogeneous metal layer, where an alternating voltage is applied.

The rate at which heat is removed from the metal surface by convection, is determined by the surface conductivity h [W/m^2 ^{0}C], while the rate at which it flows from the surface into the interior of the fiber is determined by k/r, where k [W/m ^{0}C] is the thermal conductivity of silica, and r [m] is the radius of the fiber. The dimensionless ratio between these quantities is referred to as the Biot number Bi = rh/k [70], and if Bi<<1 the fiber will assume a uniform temperature over its cross section. If there is a difference in diameter between the erbium doped fiber and the end fiber, there will be a change in dissipated power per unit length at the transition from the end sections to the center section, and this change will lead to a change in temperature. Considering a length of fiber Δx around the transition, and expressing the condition that heat flow along the fiber is comparable to heat flow away from the fiber by convection. The characteristic length for the temperature inhomogeneity is $\Delta x = \sqrt{kr/2h}$. If this length is much smaller than the distance from the discontinuity to the grating, the temperature can be considered to be homogeneous over the length of the grating, and the longitudinal heat flow can consequently be neglected. It is verified a posteriori, that both of these conditions are satisfied.

A one-dimensional rate equation for the temperature increase T_2 of the center section can be written in the following form [71]

$$\frac{dT_2}{dt} = \frac{P_{2,in}(t) - P_{2,out}(t)}{c_p \rho \pi r_2^2 L_2} \tag{7.1}$$

where c_p=730 J/kg ^{0}C is the specific heat at constant pressure and ρ = 2200 kg/m^3 the density of silica. r_2, T_2 and L_2 are the radius, temperature and length of the erbium doped center section respectively. In the following subscript 2 refers to the center section and 1 to the outer sections. The outer sections are the coated parts of the non-doped fibers, which is spliced to each end of the doped fiber. That is $2L_1 = L_{tot} - L_2$.

The total resistance can be written as

$$R = 2R_1 + R_2 = \frac{\rho_e}{\Delta}\Big(\frac{L_1}{\pi r_1} + \frac{L_2}{2\pi r_2}\Big) \tag{7.2}$$

where ρ_e is the resistivity of the metal, and Δ is the film thickness. Since for constant current the power delivered to a section of the fiber is proportional

to its resistance, the power $P_{2,in}$ delivered to the center section can be expressed in terms of the total power P as

$$P_{2,in}(t) = R_2 I^2(t) = R_2 \frac{V^2(t)}{R^2} = \frac{R_2}{R} P(t) \tag{7.3}$$

The power leaving the center section can be expressed as

$$P_{2,out}(t) = 2\pi r_2 L_2 h T_2(t) \tag{7.4}$$

For an applied sinusoidal voltage $V(t) = V_o \sin(\omega t)$, where $\omega = 2\pi f_{applied}$, equation 7.1 can be rewritten as

$$\frac{dT_2}{dt} = bP_o \sin^2(\omega t) - aT_2(t) \tag{7.5}$$

where

$$P_o = \frac{V_o^2}{R} \tag{7.6}$$

$$a = \frac{2h}{\rho r_2 c_p} \tag{7.7}$$

$$b = \frac{R_2}{R} \frac{1}{c_p \rho \pi r_2^2 L_2} \tag{7.8}$$

The homogeneous solution to equation 7.5 (which decays exponentially with time constant $\tau = a^{-1}$) is disregarded. The driven solution is found to be

$$T_2(t) = \frac{bP_o}{2a}\Big(1 - \frac{1}{\sqrt{1 + (2\omega/a)^2}} \sin(2\omega t + \theta)\Big) \tag{7.9}$$

$$\theta = \text{atan}\Big(\frac{a}{2\omega}\Big) \tag{7.10}$$

In the static limit $\omega \to 0$, $\theta \to \pi/2$, so that the solution can be written

$$T_2(t) \to \frac{bP_o}{2a}(1 - \cos(2\omega t)) = \frac{bP_o}{a} \sin^2(\omega t) = \frac{b}{a} P(t) \tag{7.11}$$

The quantity b/a can be determined from the static tuning rate via equation 7.11, since

$$\frac{b}{a} = \lim_{\omega \to 0} \frac{T_2(t)}{P(t)} = \frac{dT}{dP} \tag{7.12}$$

At an applied modulation frequency $\omega > 0$ the instantaneous laser frequency f(t) is related to T_2(t) as

$$f(t) = f_0 + \frac{df}{dT} \cdot T_2(t) \tag{7.13}$$

where f_0 is the laser frequency in the absence of modulation, and $T_2(t)$ is given by equation 7.9. Writing

$$f(t) = f_0' - f_m \cdot \sin(2\omega t + \theta) \tag{7.14}$$

it is found that the laser frequency oscillates about a mean value of

$$f_0' = f_0 + \frac{df}{dT} \cdot \frac{bP_o}{2a} \tag{7.15}$$

with an amplitude of

$$f_m = \frac{df}{dT} \cdot \frac{bP_o}{2a} \cdot \left(1 + \left(\frac{2\omega}{a}\right)^2\right)^{-1/2} \tag{7.16}$$

This equation can be rearranged, and by introducing equation 7.12 the amplitude of the modulation can be written as

$$\frac{1}{f_m^2} = \left(\frac{P_o}{2} \cdot \frac{df}{dP}\right)^{-2} \cdot \left(1 + \frac{4}{a^2}\omega^2\right) \tag{7.17}$$

so that the parameter a can be determined from a linear fit to f_m^{-2} as a function of ω^2. It is seen that for frequencies $\omega >> a$ the modulation f_m is a linear function of $P/f_{applied}$.

7.2.1 Tuning and modulation by applying a voltage

In some cases it is possible to apply both a modulation and a tuning voltage to the coating, due to a large tuning range. The power can in this case be written as

$$\begin{aligned} P &= \frac{(V_{DC} + V_{AC})^2}{R} \\ &= \frac{V_{DC}^2 + 2V_{DC}V_0 \sin(\omega t) + V_0^2 \sin^2(\omega t)}{R} \end{aligned} \tag{7.18}$$

In this case the driven solution to equation 7.1 is

$$\begin{aligned} T_2(t) &= \frac{bV_{DC}^2}{R} + \frac{bV_{DC}V_o}{aR} \frac{1}{\sqrt{1 + (\omega/a)^2}} \cos(\omega t + \theta_{DC}) \\ &\quad + \frac{bV_o^2}{2aR}\left(1 - \frac{1}{\sqrt{1 + (2\omega/a)^2}} \sin(2\omega t + \theta_{AC})\right) \end{aligned} \tag{7.19}$$

$$\theta_{DC} = \operatorname{atan}\left(\frac{a}{\omega}\right) \tag{7.20}$$

$$\theta_{AC} = \operatorname{atan}\left(\frac{a}{2\omega}\right) \tag{7.21}$$

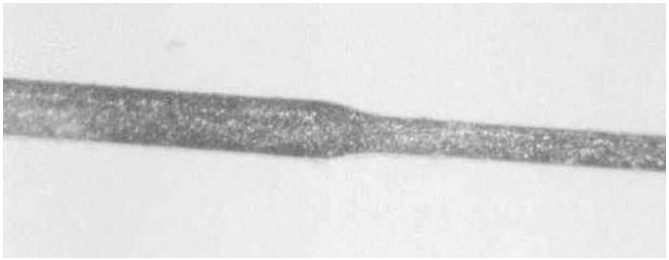

Figure 7.1: Chemically deposited silver coating.

In the case where a lock-in amplifier is used to enhance the detection sensitivity, it is necessary to have either a ωt or $2\omega t$ dependence to get a true first or second derivative in the molecular spectrum. It is therefore advisable to have either $V_{DC} >> V_{AC}$ or $V_{DC} << V_{AC}$.

7.3 Chemically deposited silver on the fiber laser

One way to produce a metal layer is by using conductive glue, but this does not give a homogenous layer. Furthermore the layer is difficult to control. Instead chemical deposition of silver can be applied.

7.3.1 Experiment

To produce a DFB fiber laser, an erbium doped fiber with a length of $L_2 = 6$ cm, a core diameter of 4 μm and a cladding diameter of 80 μm was spliced between two non-doped silica fibers with diameter of 125 μm. A 5 cm long Bragg grating was written in the erbium doped section with a Bragg wavelength of 1556 nm and a peak reflectivity larger than 99 %. After inducing an additional phase shift at the center, to ensure single-mode operation, the laser was annealed for 30 min at 200^0C and tested. It was found to produce 100 μW of radiation at the Bragg wavelength when pumped with 100 mW of radiation at 980 nm.

Next, the fiber laser was coated by chemically depositing a silver film by Tollens reaction[1] over a total length of 13 cm. Figure 7.1 shows the silver coating. It is seen, that the coating has a granular appearance.

[1]Tollen's reaction is widely used for silvering mirrors. Although most descriptions point to the risk of formation of explosive agents during the preparation of the reactant, it is usually not mentioned that it may become explosive if stored for an extended period before being used.

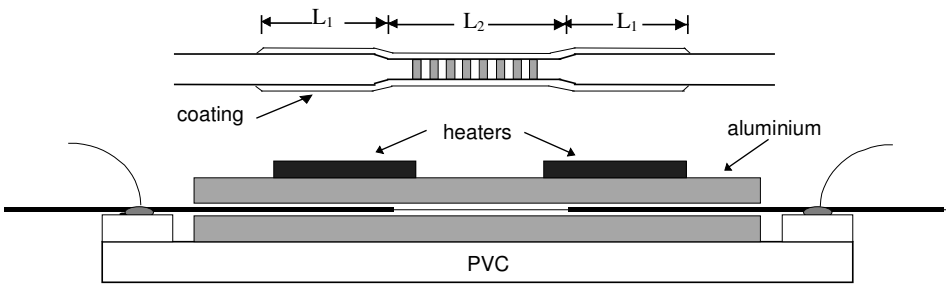

Figure 7.2: The mounting setup for the coated fiber laser. $L_2 = 6$ cm is the length of the erbium doped section, and $L_1 = 3.5$ cm is the coated length of the undoped fiber section on both sides.

The coated fiber was mounted in the setup shown in figure 7.2. To ensure a well defined environment for the fiber, it was placed at the center of a 2x2 mm^2 groove in a 12 cm long aluminum block of 10x30 mm^2 cross section. This block could be heated from the top by two Peltier elements, and in the following, this mode of heating is referred to as external heating. The aluminum block was mounted on a PVC support, and the fiber laser was attached with conducting glue to two electric terminals. The silver film could now be heated by applying a voltage to the terminals, and this mode of heating is referred to as internal heating.

The output wavelength was measured with a wavemeter with 7 digit resolution, and the wavelength response was further analyzed with a scanning Fabry-Perot interferometer with a free spectral range of 2 GHz.

7.3.2 Results

Initially, the thermal wavelength response of the fiber laser was determined by applying external heating up to 45 ^{0}C. The wavelength was found to tune linearly with temperature with a coefficient of $d\lambda/dT = 9.7$ pm/^{0}C, corresponding to a frequency tuning rate $df/dT = -1.20$ GHz/^{0}C, in good agreement with what is normally found for silica fibers. The temperature tuning is dominated by the temperature dependence of the refractive index, and the less than 10 % contribution associated with the thermal expansion coefficient of the silica fiber is not detectably modified by the presence of the silver film. During this experiment the fiber was detached from one terminal to eliminate the risk of inducing mechanical strain during heating. Static characterization of the silver film was performed by measuring the response to internal heating at applied DC power levels up to 110 mW. The emission wavelength and the electrical resistance of the film were mea-

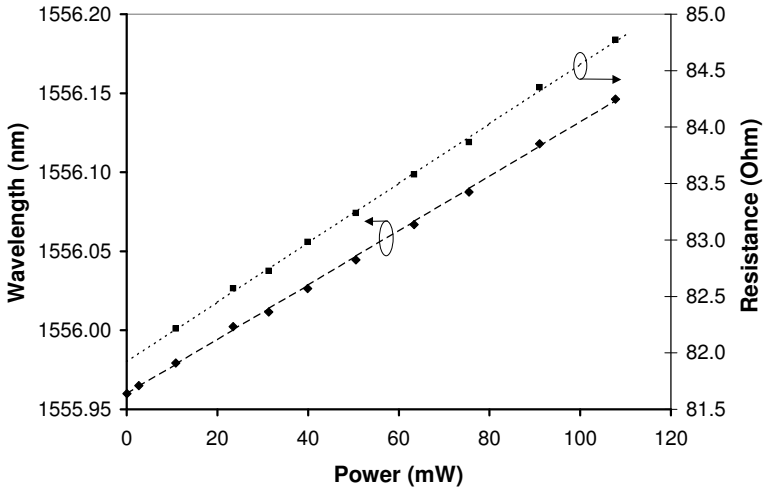

Figure 7.3: a) Wavelength tuning and b) resistive tuning as a function of applied power.

sured simultaneously with results as shown in figure 7.3. In both cases the tuning is linear with rates of $d\lambda/dP = 1.72$ pm/mW for the wavelength and $dR/dP = 0.026\ \Omega$/mW for the resistance. During this experiment the aluminum block was maintained at room temperature. The laser remained single-mode at all applied power levels, indicating adequate homogeneity of the film. Combining $d\lambda/dP$ and $d\lambda/dT$ gives $dT/dP = 0.178\ ^0$C/mW, so the temperature increases by 19.5 ^{0}C over the range covered in figure 7.3.

Dynamic characterization was performed by applying a sinusoidal voltage to the terminals. The frequency response at three different voltage levels is shown in figure 7.4 for applied frequencies from 1 Hz to 30 Hz. Due to the free spectral range of 2 GHz it was not practical to measure peak-to-peak modulations higher than about 1 GHz. Since the wavelength is controlled by the applied power, which is proportional to the voltage squared, the effective frequency is twice the applied frequency $f_{eff} = 2f_{applied}$. The modulation amplitude f_m is a linear function of the applied modulation power, and above an effective frequency of 4 Hz it is inversely proportional to the frequency. This can be condensed into the expression $f_m \approx 2.4[GHz \cdot Hz/V^2]V_{rms}^2/f_{eff}$ where V_{rms} is the applied rms voltage, and f_{eff} is the effective modulation frequency in Hz.

During all experiments the line width of the laser was found to be smaller than the 10 MHz resolution limit of the scanning Fabry-Perot interferometer.

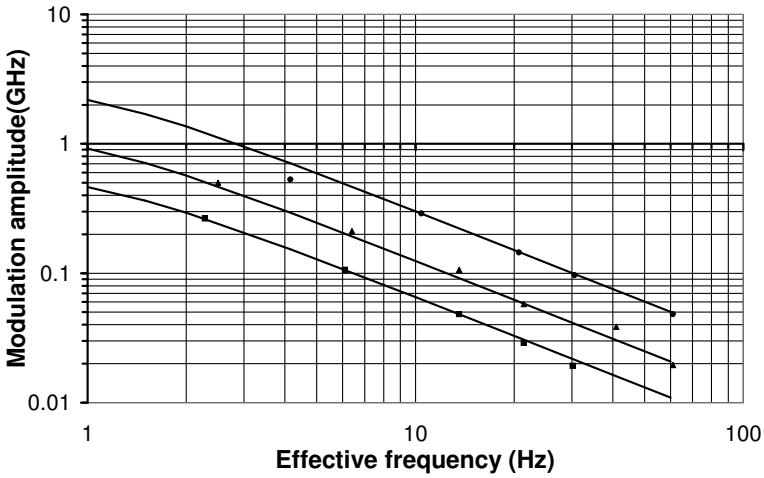

Figure 7.4: Frequency response of temperature modulation for 0.508 Vrms (■), 0.76 Vrms (▲) and 1.117 Vrms (•)

V_{RMS}[V]	a [s^{-1}]	b[^{0}C/mJ]
1.12	5.75	1.02
0.76	5.18	0.92
0.51	5.55	0.97
Average	5.49	0.97

Table 7.1: Least squares analysis of the data of figure 7.4.

7.3.3 Analysis

In the following, subscript 2 refers to the center section of length L_2=6 cm and radius r_2=40 μm, while subscript 1 refers to either of the end sections each of length $L_1 = (14 - L_2)/2 = 3.5$ cm and radius 62.5 μm. Assuming the specific resistivity of the silver coating to equal the bulk resistivity, and assuming the film thickness to be uniform, the thickness can be evaluated from the measured resistance. With a specific resistivity of $\rho_e = 1.66 \cdot 10^{-8}$ Ωm, and taking into account the variation in diameter of the coated length, the film thickness is found to be 84 nm.

The frequency response of temperature modulation results is shown in figure 7.4. The data are fitted with a least squares fit of equation 7.17. This gives the a and b values listed in table 7.1, where b is found from equation 7.12. The scatter of the results is mainly due to the uncertainty associated with reading the peak-to-peak modulation from the scanning Fabry-Perot interferometer. Using the average value of a =5.49 s^{-1} from

Table 7.1 together with ρ= 2200 kg/m^3 and c_p = 730 J/kg ^{0}C, a surface conductivity of h = 176 W/m^2 ^{0}C is found from equation 7.7. With a heat conductivity of k = 1.6 W/m ^{0}C and a fiber radius of r_2 = 40 μm a Biot number for the center section is Bi = 0.0059, and the assumption Bi<<1 is therefore justified. The extent of the temperature inhomogeneity at the transition to the center section is $\Delta x = \sqrt{(kr/2h)} \approx 0.4$ mm, so that also the assumption of homogeneous temperature along the length of the grating is justified. Rogers *et al* [68] have found a surface conductivity of h=130 W/m^{2}0C for e-beam evaporated gold films. Assuming the surface conductivity to scale as the bulk conductivity, this corresponds to a value of 130·(429/317) W/m^2 ^{0}C = 176 W/m^2 ^{0}C for silver. The perfect agreement of experimental values is of course somewhat fortuitous in view of the scatter of the a values in Table 7.1. From equation 7.8 a value of b = 1.18 ^{0}C/mJ is found, also in good agreement with the average b-value of Table 7.1.

The modulation amplitude can also be expressed as in section 7.3.1. The coefficient of 2.4 GHz can also be found from the a value by equation 7.17, which gives:

$$f_m = \left(\frac{P_o}{2} \cdot \frac{df}{dP}\right) \cdot \frac{a}{2 \cdot 2\pi f_{applied}} = \left(\frac{a}{2\pi R} \cdot \frac{df}{dP}\right) \cdot \frac{V_{rms}^2}{f_{eff}} \simeq 2.3 \frac{V_{rms}^2}{f_{eff}} \quad (7.22)$$

The good agreement was expected, due to the good fit of the measured data. It is seen that this fit only gives the a value, where the other fit can give both a and b if the modulation response for slow frequencies can be measured.

7.3.4 The chemically deposited coating

The silver coating was produced by chemical deposition. The advantages with this technique are that it does not require specialized equipment and that the layer has approximately the same radial thickness. The drawbacks are the fragility of the coating which is easily damaged by mechanical contact, and the potential explosion hazards associated with Tollen's reaction. The best coating was made the first time, after this some black dirt particles appeared on the coating. In some cases there were areas where the silver had fallen off. This type of coating can therefore not be recommended.

The first silver coating on a fiber laser worked as intended and it has been used for experiments such as gas monitoring.

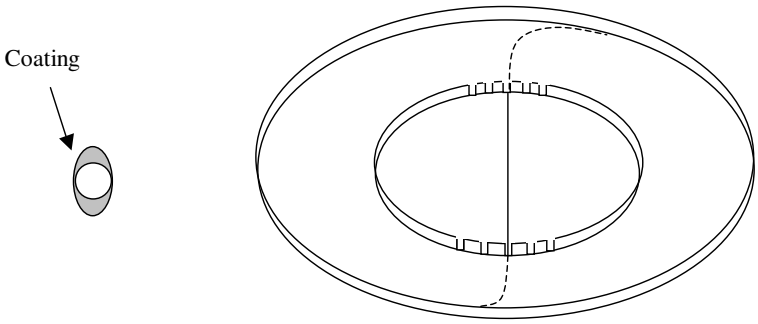

Figure 7.5: a)Illustration of the cross section of the metal layer evaporated on the fiber b) sketch of the fiber holder. The center part is not covered. The dashed lines indicates the fiber which is covered.

7.4 Metal coating produced by electron beam evaporation

Instead of chemically deposited silver it is possible to use electron beam evaporation, to deposit a metal coating. Here a metal is evaporated by an electron beam, and the flying metal hits the sample on the side facing the metal. Since the metal is hitting the fiber at one side, it is necessary to turn the specially designed holder to get metal on the other side of the fiber. This gives a metal layer, which has a cross section shown on figure 7.5a. The holder is limited by the evaporation setup, which is designed for 4 inch wafers. This gives a limitation in the diameter of 110 mm and 6 mm in the height. Furthermore only metal is allowed in the chamber. In the first holder the fiber was mounted like a coil, where a length of 12 cm was unblocked from both sides, so the fiber can be coated from two opposite sides. The problem with this holder is, that it can only be used for one fiber laser at the time. The next holder was designed to contain 5 fiber lasers. This decreases the coated length since the fiber laser can not be bend too sharply to prevent it from breaking (se figure 7.5b). This gives a coated length of between 6 and 7 cm, depending on where in the holder it is placed. This means that there is only a small distance from the grating to the edge of the coating. This is not a problem, since the characteristic length of the temperature inhomogeneity Δx is very short, as seen for the silver coating. The fiber laser used for this part, was produced by Koheras, and they used a doped fiber with a diameter of 125 μm.

7.4.1 Experiment

In this experiment a DFB fiber laser with an Erbium-Ytterbium (Er-Yb) doped fiber was used. It was produced by Koheras. The emission wavelength is 1548 nm, and the output power is 5 mW, when pumped with radiation at 980 nm with a power of 100 mW. Er-Yb lasers absorb almost all the pump energy, so there is a gradient of pump radiation through the fiber. This can result in instability of the laser, which can be minimized by the correct mounting.

Coating with e-beam evaporation.

The fiber laser was coated with the gold layer by use of e-beam evaporation, to get a fast evaporation and a reproducible coating. To make the gold bond and ensure that the gold does not diffuse into the core, a 50-100 Å titanium layer was evaporated before the layer of 2000 Å gold.

It is assumed, that this layer does not induce strain effects when it is heated by a current, since the metal layer has equal thickness on opposite sides. If the layer is not homogenous, it can induce either a phase shift (if it is like a point defect) or chirp if the layer varies slowly along the fiber. Investigations of the reflection or transmission before and after evaporation of gold, shows that there is not induced an additional phase shift. Figure 7.6 shows the transmission spectrum, when a voltage is increased from 0 V to 5 V. It is seen, that there are no additional phase shifts. The two phase shifts belong to two polarizations. The laser is single-mode, if it is mounted carefully.

Characterization of the coating properties

The temperature coefficient of the coated DFB fiber laser was found by heating the laser in the holder from section 7.3.1 without attaching the ends, to prevent mechanical stress. This gave a linear dependence of temperature with a coefficient of $d\lambda/dT$=9 pm/^{0}C.

The coated DFB fiber laser was mounted in a brass holder shown on figure 7.7. The holder is 20x5x100 mm^3 with a grove of 2x2 mm^2. The two electrodes are isolated from the holder, so the fiber laser can be attached to the electrodes (with conducting glue) without touching the brass. A 2 mm thick brass plate is used as a top plate. The holder has not any Peltier elements, since the wavelength can be tuned sufficiently by changing the voltage.

Static characterization of the resistance and emission wavelength of the fiber laser was done simultaneous, as a function of applied power up to

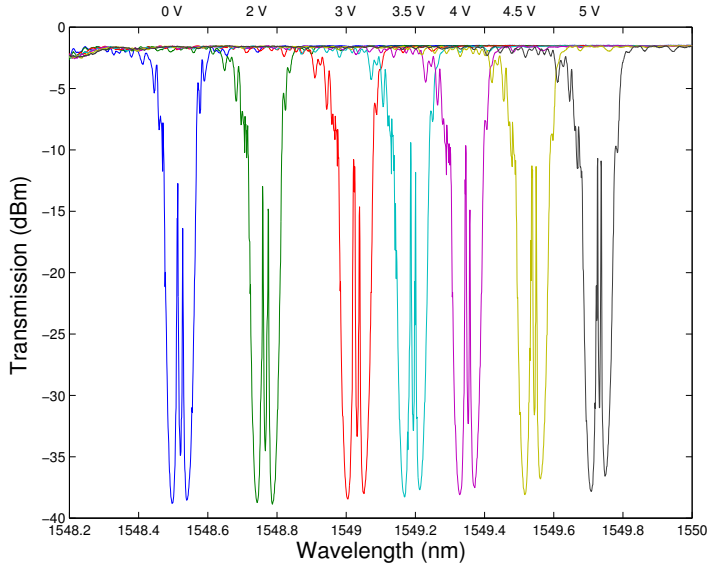

Figure 7.6: Transmission spectrum when the voltage is increased from 0 V to 5 V. The voltage is written above the associated transmission dip.

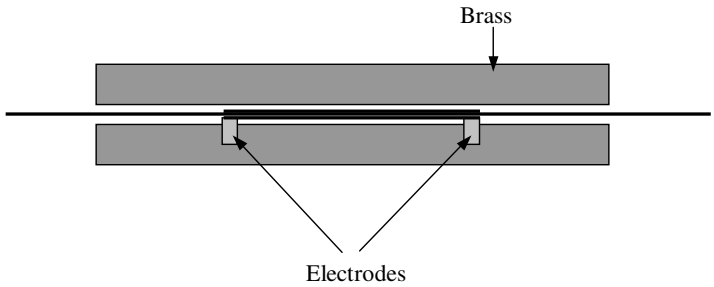

Figure 7.7: Brass holder for the coated fiber. The electrodes are isolated from the rest of the metal, and placed so the fiber can be mounted without touching the brass block.

500 mW. It is seen in figure 7.8, that both wavelength and resistance tuned linear with rates of $d\lambda/dP = 2.77$ pm/mW and $dR/dP = 0.03$ Ω/mW respectively. Combining $d\lambda/dT$ and $d\lambda/dP$ gives $dT/dP = 2.77/9$ ^{0}C/mW $=0.31$ ^{0}C/mW. This means, that over the range covered in figure 7.8 the temperature increased by 154 ^{0}C. This temperature increase is much higher than for the silver coating. The reason is that all the power is applied to

the grating, and the total power is much higher in this case. The fiber

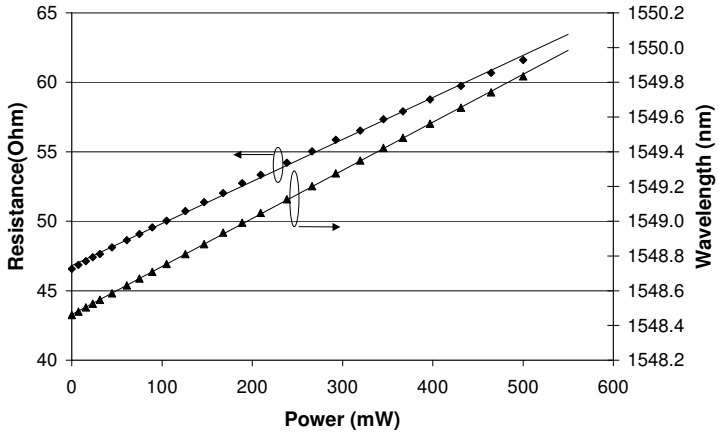

Figure 7.8: Wavelength and resistance tuning as a function of applied powers.

laser was annealed during production. If the annealing temperature was lower than the induced temperature, a further annealing can happen. This can change the properties of the fiber laser the first time it is influenced by a high voltage, but afterwards the results are reproducible. The resistance does also change after first measurement, where the gold probably has reconfigured. Afterwards it is also reproducible, if the voltage is not increased further.

The fiber laser remained single-mode up to the maximal applied power of 500 mW, but the optical output power decreased for increasing voltage. This is shown in figure 7.9, where the optical power was measured with a detector. The lower maximal power is due to the applied AC+DC coupler, which lowered the maximal voltage range. The wavelength was measured with the wavemeter, which has an analog output. The analog output is restrained to a change in wavelength of ± 0.1 nm from the setpoint wavelength, so two scans were necessary to cover the applied power range. When the limit of the analogue output is reached, the output of the wavemeter saturates as seen above ~ 250 mW. It is seen that the optical power oscillates, which is not the case for the wavelength. The oscillation has a constant period, so it comes from etalon effects in the setup. The decrease in optical power is due to the faster change in phase shift compared with the center wavelength as shown in figure 7.6. This will result in a non-optimal phase shift and thus a decreasing power. The oscillation in optical output power is not a problem in our case, since it changes slowly. To make the influence smaller, a balanced detector can be used for gas

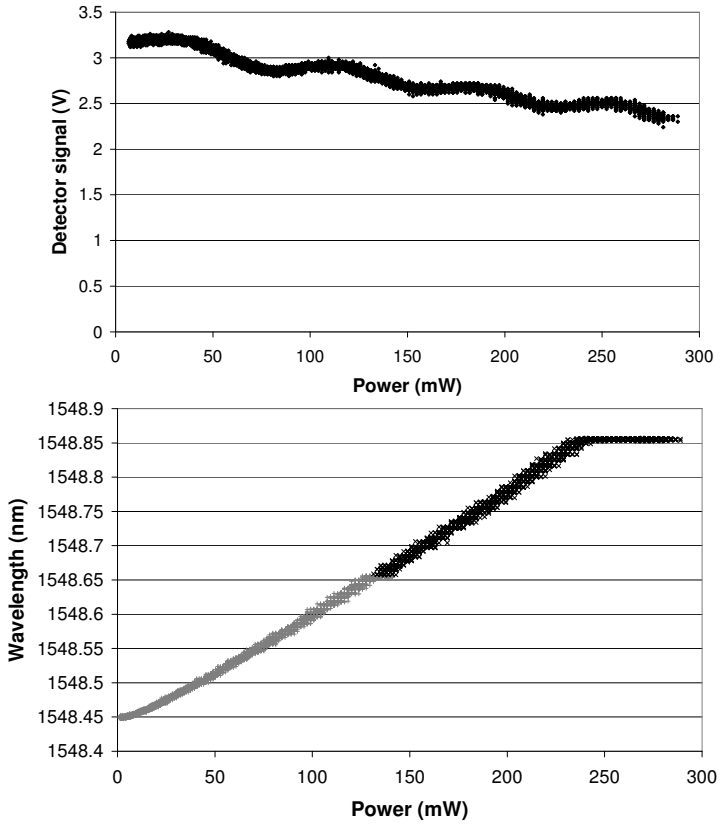

Figure 7.9: Optical output power and wavelength as a function of applied power. The wavelength is measured with two scans, since the range of the analogue output on the wavemeter is ±0.1 nm.

sensing or for locking applications.

As for the silver coating, the gold coating can be modulated by applying a sinusoidal voltage. The response of the frequency modulation was investigated with the scanning Fabry-Perot interferometer (with a free spectral range of 2 GHz), for 4 different amplitudes. Figure 7.10 shows the modulation response for, V_{rms}= 0.4 V, V_{rms}= 0.9 V, V_{rms}=1.5 V and V_{rms}=2.0 V for applied frequencies in the range 0.7 Hz to 90 Hz. When the amplitude increases, the responding modulation can get higher than 1 GHz. In this case only modulations resulting from slow applied frequencies can be measured with the scanning Fabry-Perot interferometer.

The figure shows that for low applied frequencies the modulation amplitude goes towards a constant value, while for high applied frequencies it

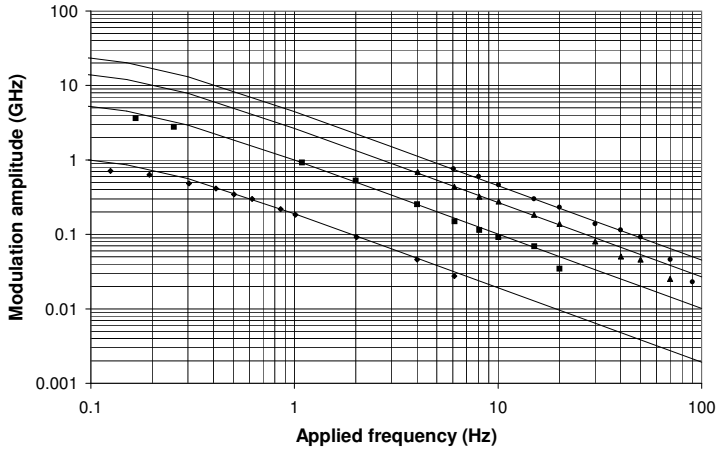

Figure 7.10: The amplitude of the frequency modulation, when an AC voltage with applied frequency $f_{applied}$ is used. (no DC voltage). The rms values are 0.4 V(♦), 0.9 V (■), 1.5 V (▲) and 2 V (•)

falls off as f^{-1}.

7.4.2 Analysis

For an Er^{3+}-Yb^{3+} doped fiber with radius 62.5 μm and a length of 5.3 cm between electrodes the resistance is 46 Ω. Assuming that the bulk resistivity of $\rho_e = 2.24 \cdot 10^{-8}\Omega$m for gold applies, the resistance depends on the thickness Δ by

$$R = \frac{\rho_e L}{A} = \frac{\rho_e L}{\pi r_2 \cdot (r_2 + \Delta) - \pi r_2^2} \tag{7.23}$$

so the thickness is

$$\Delta = \frac{\rho_e L}{\pi r_2 R} = 0.13\ \mu m \tag{7.24}$$

From the data the relationship between the frequency modulation and the power can also be found. This gives $f_m = 0.029P/f$, where f is the applied frequency. From this relationship the a or b value can be found from equation 7.16 in the case where $4\pi f/a > 1$. This gives

$$f_m = \frac{df}{dT} \cdot \frac{bP}{2a} \cdot \frac{a}{4\pi f} = \frac{1.126 \cdot b}{8\pi} \frac{P}{f} = 0.029 \frac{P}{f} \tag{7.25}$$

so $b = 0.64\ ^0$C/mJ. The a value can be found from the statical limit to be: $a = b/(dT/dP) = 0.647/0.308 = 2.08\ s^{-1}$.

From the a value the surface conductivity h can be found by applying equation 7.7. This gives h=104 W/m^2 ^{0}C, which is lower than the value h=130 W/m^2 ^{0}C Rogers *et al* [68]. They had a homogeneous gold layer on the fiber. The surface conductivity depends on the shape of the surface. In my experiment the layer is elliptical distributed around the fiber. This is probably the reason for the different values of the surface conductivity.

The b value can be found from equation 7.8, which gives b=0.96 ^{0}C/mJ. In this case it seems like the calculated b value is too high. Figure 7.10 shows the data points together with the curves calculated with the fitted a and b values. It is seen that there is good agreement for applied frequencies higher than 0.4 Hz. Below this value the data points are very inaccurate, since the frequency modulation is to close to the free spectral range of the scanning Fabry-Perot interferometer.

The Biot number is Bi= $62.5 \cdot 10^{-6} \cdot 138/1.6 = 5.3 \cdot 10^{-3}$, so the assumption about uniform temperature over the fiber cross section applies. The characteristic length is found to be $\Delta x = \sqrt{kr/2h} = \sqrt{1.6 \cdot 62.5 \cdot 10^{-6}/2 \cdot 138}$ m =0.6 mm, thus the temperature along the grating is homogeneous.

7.5 Mounting of the DFB fiber laser

The performance of a DFB fiber laser is very dependent on how it is mounted, since additional phase shifts can change the behavior. The additional phase shifts can occur from for example twist of the fiber or temperature variations. The mount used in section 7.3.1 is good for gas sensing applications due to the large external heat tuning range, as will be illustrated in section 7.6.

For stabilization of the DFB fiber laser this mount is not good, since temperature fluctuation of 0.1^{0}C gives a change in wavelength of 0.1·53 pm = 0.656 GHz, and the HWHM line width for transitions in the combination band of $^{13}C_2H_2$ is between 0.3 GHz and 0.5 GHz. The temperature fluctuation will therefore lead to a sweep through the absorption line.

To be able to stabilize the DFB fiber laser it is necessary to have a low temperature coefficient in the setup, to make it possible to lock the laser to the line center. The simplest way is to have the fiber laser lying on the table with the two electrodes glued on the fiber with conductive glue. Unfortunately a laser which is single-mode, can become unstable when a voltage is applied due to air flow and turbulence. This is the case since different parts of the laser is cooled different.

Instead the laser with the electrodes glued on can be put into a glass tube. In this case the laser is in a more stable environment, but it is difficult

to mount the fiber laser in this way, since the electrodes can induce stress in the fiber. If the laser is mounted, so that it is single-mode, it is possible to use it for gas sensing and lock it to an absorption line.

A third possibility is to mount the DFB fiber laser in a brass block with isolated electrodes as described in section 7.4.1. In this case the brass works as a stable environment, and it is not necessary to add Peltier elements, if the laser can be tuned sufficiently by the power applied to the coating. Investigations of the laser mounted in this holder and locked to an absorption line in $^{13}C_2H_2$ will be done in section 7.7.

7.6 Gas sensing

To perform gas sensing it is necessary to tune the wavelength through absorption lines. Wavelength tuning can be done by changing the temperature. There are two ways to do that, either external heating, which will be described in section 7.6.1, or internal heating which will be described in section 7.6.2.

7.6.1 External temperature tuning

A DFB fiber laser, which can be tuned and modulated, can be used for gas sensing by scanning the wavelength through a region with absorption lines of the gas investigated. The modulation is necessary to make synchronous detection. The setup for wavelength modulation spectroscopy is illustrated in figure 7.11. It will be applied for spectroscopy of $^{13}C_2H_2$ [58].

Application of external heating to the mount shown in figure 7.2 will cause a bending of the PVC support due to the inhomogeneous temperature distribution, and if both ends of the fiber are fixed to the terminals, this will cause the fiber to be strained. In combination with the temperature dependence of the refractive index, this leads to an overall tuning rate of 53 pm/^{0}C, and scanning the temperature from 30 ^{0}C to 45 ^{0}C a wavelength range from 1556.5 nm to 1557.3 nm is covered, corresponding to about 100 GHz.

The spectrum as seen in figure 7.12 is recorded by measuring the signal transmitted through a 500 mm cell containing nominally 99 % pure $^{13}C_2H_2$ at a pressure of 100 mbar. Modulation is applied at 14 Hz with a rms voltage of 0.57 V, corresponding to a modulation amplitude of $f_m = 0.028$ GHz at an effective frequency of 28 Hz, and the spectrum is recorded by setting the lock-in amplifier to detection at the second harmonic of the applied frequency (se section 5.3.1). Equation 5.29 gives the signal for the first

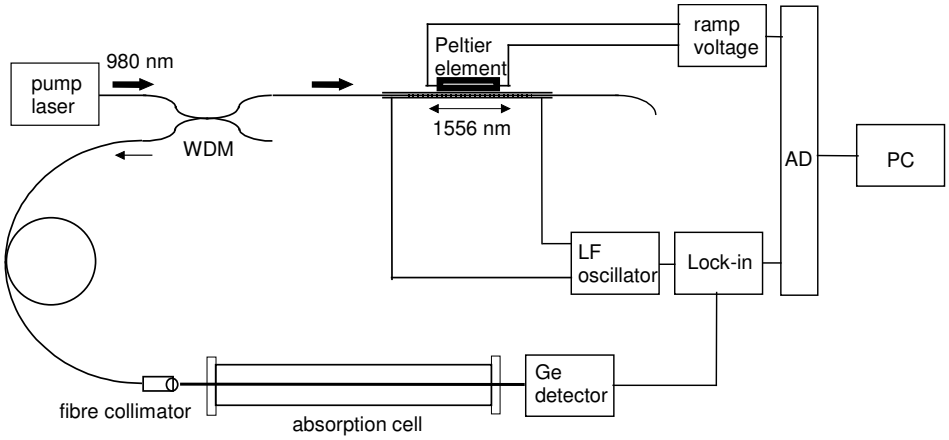

Figure 7.11: Experimental setup for wavelength modulation spectroscopy.

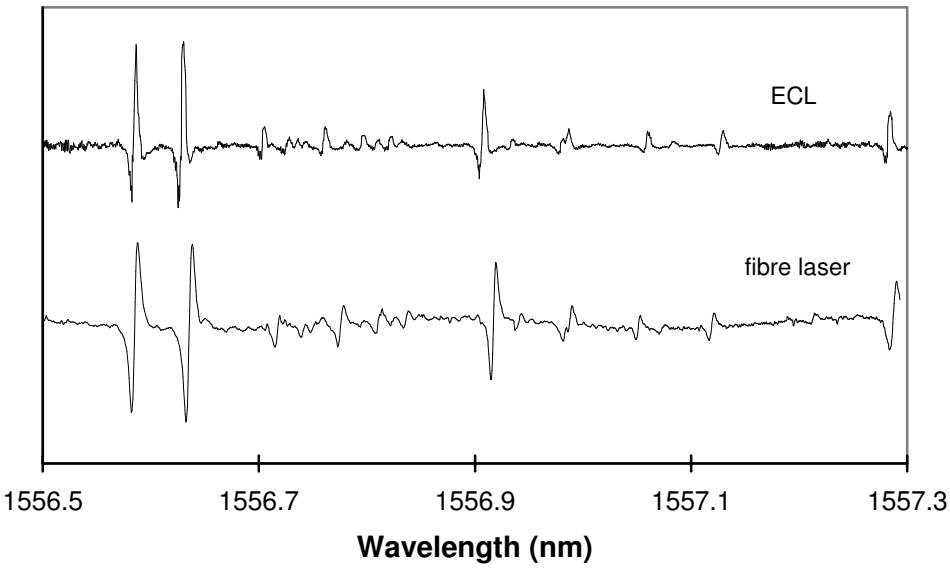

Figure 7.12: Wavelength modulation spectra recorded with a thermally modulated fiber laser (lower) and a piezo modulated extended cavity laser (upper).

derivative of the absorption coefficient for a modulation Ω. In this case $\Omega = 2\omega$ so the equation becomes

$$S(2\omega) = -aL\frac{d\alpha}{d(2\omega)}\sin(2\omega t) = K(\omega)\cos(2\omega t + \pi) \tag{7.26}$$

It is the applied frequency ω which is used by the lock-in amplifier. When the settings is set to record the second derivative profile, it measures a signal which is proportional to $\cos(2\omega t)$. This means that when the setting is for a second derivative spectrum, it is the first derivative with respect to the effective frequency which is measured.

Under the given conditions the lines are Voigt profiles with HWHM line widths ranging from 0.3 to 0.5 GHz, and since the modulation amplitude is substantially smaller, the signals are not significantly affected by modulation broadening.

In figure 7.12 the spectrum recorded with temperature modulation is compared with a similar spectrum recorded with a New Focus extended cavity laser with 313 Hz piezo modulation and second harmonic detection. Ideally, line profiles recorded with this detection scheme should be symmetric, reflecting the second derivative of the Voigt profile, and the asymmetry observed in figure 7.12 is a consequence of some residual amplitude modulation [62]. It is seen that all the absorption lines are resolved as good as in the spectrum recorded with the New Focus laser. The background variation can be due to etalon effects from the gas cell with planar windows.

7.6.2 Tuning of the wavelength by a DC-voltage ramp

The DFB fiber laser with the gold coating can also be used for gas sensing. Due to the large tuning range, it is possible to tune the wavelength with a DC-voltage ramp, and simultaneously apply an AC-voltage for modulation of the wavelength. In this case a voltage ramped from 0 V to 4.6 V was applied. The applied modulation of 0.14 Vrms at 10 Hz, giving a frequency modulation of about 100 MHz. Again the 500 mm gas cell containing 99 % $^{13}C_2H_2$ at a pressure of 100 mbar was used. The first harmonic of the applied frequency was recorded with the lock-in amplifier. Figure 7.13 shows the scan where the P26 (1548.820 nm) is the strongest line. The wavelength axis is calibrated, like figure 7.12, from the knowledge of the wavelength of different absorption lines. The applied voltage was measured together with the lock-in signal. The maximal applied voltage was 4.6 V. If it is assumed that the resistance is equal to the DC case, the maximal applied power was $\sim$ 350 mW. This change in power should increase the wavelength by: $0.350 \cdot 2.77$ nm=0.97 nm. The wavelength scan

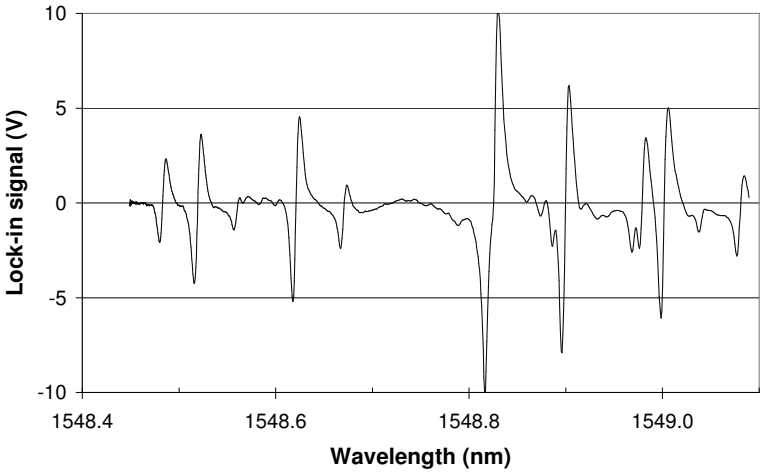

Figure 7.13: First harmonic wavelength modulation spectra of $^{13}C_2H_2$ recorded with a DFB fiber laser coated with a gold film. The laser is tuned by a DC-voltage and modulated by a AC-voltage. The large absorption line is the P26 line.

is only 0.61 nm. This gives a tuning coefficient of $d\lambda/dP = 1.75$ pm/mW. Another explanation is, that the resistance is increased when an AC voltage is applied since the mean temperature is increased. This will give a smaller effective power, and thus a smaller tuning range.

7.7 Locking the DFB fiber laser wavelength to an absorption line in $^{13}C_2H_2$

As shown in section 6.4.1 the wavelength has a drift in time. The long-term drift can be eliminated by locking the laser wavelength to an absorption line. In this case the error signal from the integrator is added to the AC and DC voltages. This works as a servo circuit. In the case of an applied frequency of 10 Hz the time constant is set to 1 s. It is therefore only possible to compensate for slow variations. Figure 7.14a shows the detector signal and the output from the lock-in amplifier when the wavelength is scanned through an absorption line. It is seen that it is possible to determine the line center very accurately from the detector signal, by scanning the wavelength through the absorption line, and stop where the signal is minimal, and the phase of the modulation changes. The lock-in signal shows the first derivative of the detector signal, which is delayed ~ 0.2 sec.

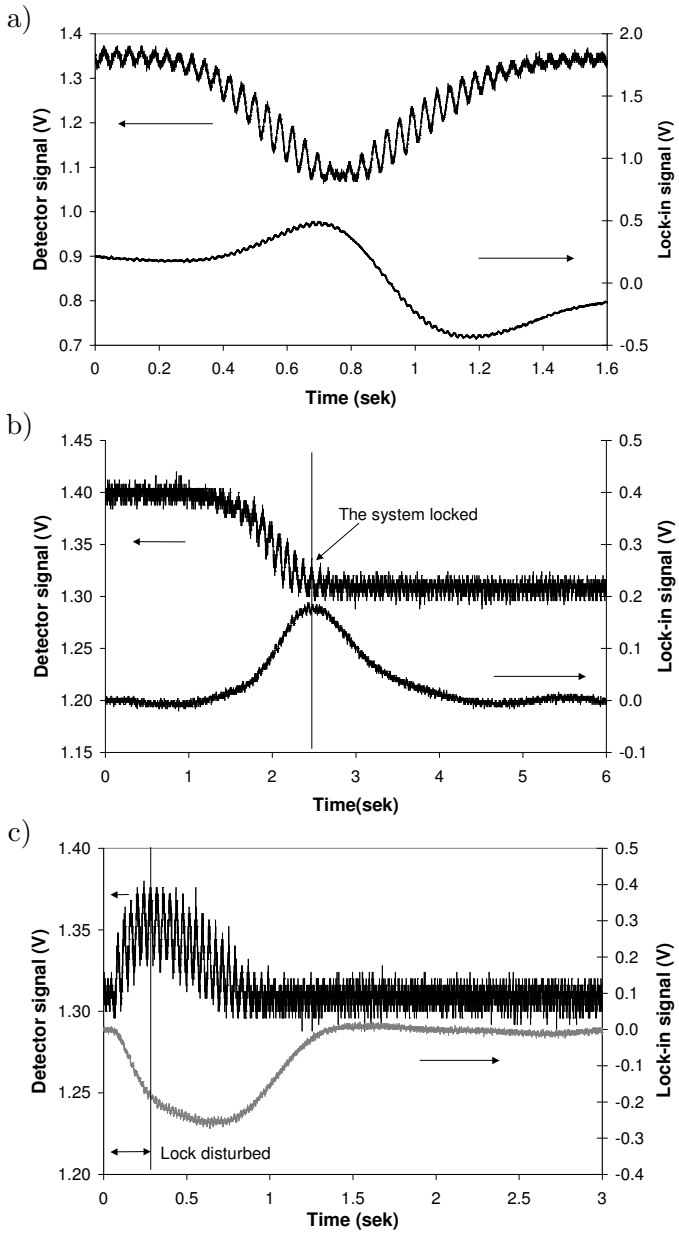

Figure 7.14: The detector signal and the output from the lock-in amplifier, when a) the wavelength is scanned through an absorption line, b)the lock is applied and c)the wavelength is changed a bit away from the line center to test the lock.

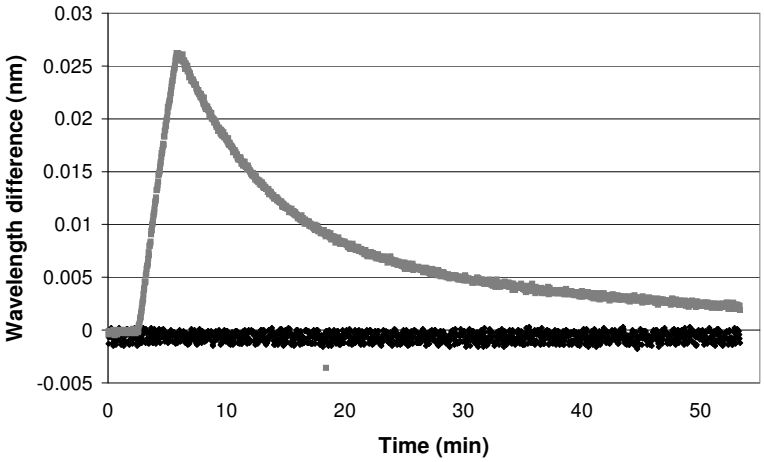

Figure 7.15: The wavelength change when heat is applied for 4 minutes, so the temperature increased 2.5 ^{0}C. The gray curve is for the unlocked laser and the black curve is for the locked laser.

If the lock is applied at the center wavelength the behavior is illustrated on figure 7.14b.

It is seen, that the error signal return to zero when the lock is applied. There is a small transient in the signal. If the sensitivity on the lock-in amplifier is too high, the error signal increases. In this case the error signal overshoots, and this results in oscillations in the lock-in signal due to delay in the system.

In the case where the wavelength is changed a bit away from the line center, the error signal will increase, and the servo circuit will apply a voltage to the fiber to return the wavelength to the line-center. This process is shown in figure 7.14c. It is seen that the lock-in signal changes until the wavelength is at the center of the absorption line. Then the lock-in signal returns to zero, like the case where the lock is applied.

The lock can be investigated by heating the laser with a lamp in 4 minutes, and measure the change in wavelength. During this time the temperature increased 2.5^{0}C. The wavelength was measured with the wavemeter and the analog output was sent to the AC/DC card. Figure 7.15 shows the result for the unlocked (gray) and locked (black) laser. It is seen that the laser remains locked for a change of $\sim$ 2.5 ^{0}C.

To investigate the stability of the laser measurements were done with and without locking the laser. To have a measure for whether the laser was locked to the line center or locked away from the absorption line, the

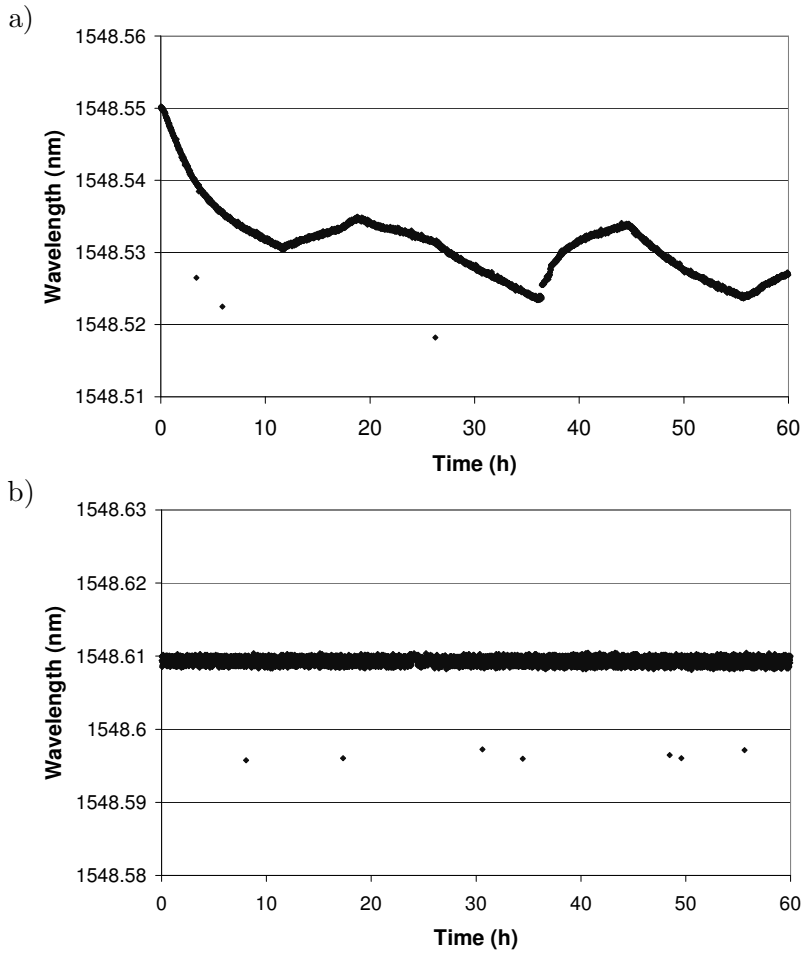

Figure 7.16: The wavelength when the laser is a) unlocked and b) locked as a function of time.

wavelength was measured. Figure 7.16 shows the wavelength change for the laser when it is a) unlocked (and without any voltage) and b) locked. It is seen, that there is some data which jumps in the data series. This is due to the wavemeter, which sometimes measured wrong because of intensity fluctuations. This data is removed from the stability calculations, since they are not due to the fiber lasers wavelength stability. It is seen that when the laser is not locked there are some daily variations in the wavelength corresponding to a change in temperature of $\sim$1 ^{0}C. The big decrease in the beginning, is due to a temperature decrease after removal of the voltage. The discontinuity is due to a short stop of the data acquisition program.

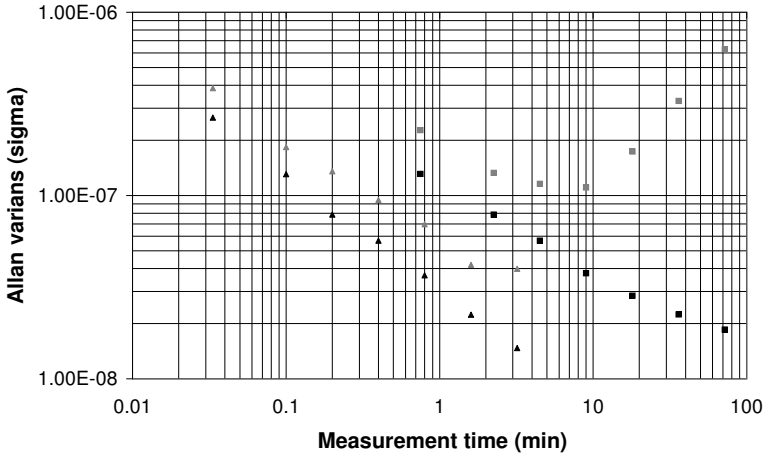

Figure 7.17: The Allan variance for a unlocked (gray) and locked laser (black) for sampling intervals of 2 sec. (△) and 45 sec. (□).

As shown in section 5.3.2 the stability can be investigated by an Allan variance. To make an Allan variance the wavelength change was measured with a 2 sec. and 45 sec. sampling intervals for the locked laser, and when the laser did not have a voltage on the coating. The different points in figure 7.17 are found by averaging over 1, 3, 6, 12, 24, 48 and 96 points to get different measuring times. The Allan variance is calculated for these measuring times. It is seen that the lowest variance of $1.5 \cdot 10^{-8}$ is for the 2 sec. sampling interval series, this gives the stability of: $1.5 \cdot 10^{-8} \cdot 3 \cdot 10^{8} / 1548 \cdot 10^{-9}$ Hz=2.9 MHz. The offset of the series with the 45 measuring interval is due to the modulation, which always has an influence for a few averaging points. To minimize the effect, a very long series with a short sampling interval can be measured, and the different variances at different measuring times can be found by averaging the data points. This is not done here due to the limited number of points in the data acquisition program, which makes it difficult to get a daily variation. It is seen that the unlocked data points follow $\tau^{-1/2}$ at short times which is due to white noise. At longer times it behaves like τ^{1} due to drift in the system. For longer times it is still the white noise, which sets the limitation of the locked fiber laser. It is therefore reasonable to believe, that the system is stable at longer time scales as well. The stability limit of the locked laser is set by the Doppler broadening of the line. The lower limit will look like a constant value in the Allan variance plot.

7.8 Conclusion

It has been shown, that it is possible to modulate and tune the wavelength by temperature heating through resistive heating of a metal film.

The fiber laser tuned by resistive heating was single-mode if the metal was e-beam evaporated, and the laser was mounted carefully. The laser could be tuned linearly with 2.77 pm/mW by increasing the applied power. As shown it is both possible to tune and modulate the wavelength with external heating and with internal heating. The laser can therefore be used for gas monitoring, and it can be stabilized. The found stability of $2 \cdot 10^{-8}$ was limited by the Doppler broadened line.

Chapter 8

Conclusion

In this thesis I have investigated different subjects.

It has been shown, that the core concentricity error direction can be found by diffraction. A bending sensor can therefore be produced in a controlled way. The wavelength splitting was insensitive to change in temperature, and the sensitivity in the maximal bending response direction did not depend on the writing direction. It is therefore possible to perform simple and robust bending measurements. To resolve the bend it is necessary to measure the wavelength in the range around the wavelength resonance. This sensor will only describe the bend and not temperature or other types of strain. Such a bend sensor can be applied in constructions where the bend has to be monitored, due to a potential danger if the construction fails. The changes have to be slower than the monitoring system.

Another type of grating based sensor was investigated in chapter 4. It was based on a combination of a long-period grating and two sampled gratings, to be able to measure both strain and temperature changes with a detector. The behavior was simulated with the transfer matrix method, but this did not explain the real measurements, since the calculated widths were too narrow. A calculation based on the measured reflection spectra gave a reasonable agreement with the measured data. It is reasonable to believe that the data can be expressed by these calculations, if the applied temperature and strain can be calibrated correctly. The sensor can be improved by minimizing the insertion loss, increasing the reflected power by decreasing z_1/z_0 and increasing the total fluence. A way to increase the reflected power is by designing the long-period grating and the sampled gratings to have their response at the maximal value of the input power.

In the other part of the thesis DFB fiber lasers have been applied for gas monitoring, and they have also been stabilized to a Doppler broadened

absorption line. Two different techniques have been applied to tune and modulate the output wavelength. A PZT modulated DFB fiber laser can be modulated with frequencies up to the kHz range, which makes it possible to stabilize the laser for variations slower than 0.1 sec. The applied setup has a large increase in power when the PZT voltage is increased. There is furthermore a hysteresis effect with regards to the wavelength. The coarse PZT makes it possible to tune the wavelength 1.8 nm.

A technically simpler way to tune the wavelength is by resistive heating. A metal coating produced by chemically deposited silver was fragile and not reproducible. There was furthermore an explosion hazard involved under production. The laser could be used for gas monitoring, but the mount it was put in, made it impossible to lock the laser. Electron beam evaporation produces a reproducible metal layer, which does not induce additional phase shifts. It is furthermore possible to tune the wavelength 1.4 nm by applying a DC voltage. The modulation can be up to 100 Hz, which makes it possible to stabilize the wavelength for variations which are longer than 1 sec. In both cases the stability of the locked DFB fiber laser was ~ 2 MHz, limited by the Doppler broadened line. This is more than good enough for DWDM systems with a wavelength separation of 50 GHz.

Appendix A

The point group $D_{\infty h}$ of Acetylene

$D_{\infty h}$	I	$2C_\infty^\phi$	...	$\infty\sigma_v$	i	$2S_\infty^\phi$	...	∞C_2	
$A_{1g} \equiv \Sigma_g^+$	1	1	...	1	1	1	...	1	
$A_{2g} \equiv \Sigma_g^-$	1	1	...	-1	1	1	...	-1	R_z
$E_{1g} \equiv \Pi_g$	2	$2\cos(\phi)$	...	0	2	-2cos(ϕ)	...	0	(R_x, R_y)
$E_{2g} \equiv \Delta_g$	2	$2\cos(2\phi)$	...	0	2	$2\cos(2\phi)$	...	0	
$E_{3g} \equiv \Phi_g$	2	$2\cos(3\phi)$	...	0	2	-2cos(3ϕ)	...	0	
$\vdots$	$\vdots$	$\vdots$		$\vdots$	$\vdots$	$\vdots$			
$A_{1u} \equiv \Sigma_u^+$	1	1	...	1	-1	-1	...	-1	T_x
$A_{2u} \equiv \Sigma_u^-$	1	1	...	-1	-1	-1	...	1	R_z
$E_{1u} \equiv \Pi_u$	2	$2\cos(\phi)$	...	0	-2	$2\cos(\phi)$	...	0	(T_x, T_y)
$E_{2u} \equiv \Delta_u$	2	$2\cos(2\phi)$	...	0	-2	$-2\cos(2\phi)$	...	0	
$E_{3u} \equiv \Phi_u$	2	$2\cos(3\phi)$	...	0	-2	$2\cos(3\phi)$	...	0	
$\vdots$	$\vdots$	$\vdots$		$\vdots$	$\vdots$	$\vdots$			

Table A.1: The $D_{\infty h}$ point group [57]

C_∞^ϕ is a rotation with an angle ϕ around the molecular axis.

σ_v: reflection in the plane which is vertical with respect to the highest-fold axis.

S_∞^ϕ: rotation and reflection

Appendix B

Publications

This thesis is based partly on the work presented in the following international publications and conferences. The publications is in S.Søgaard since I got married after the publication dates.

H. Simonsen, J. Henningsen, S. Søgaard and J.E. Pedersen: "CO_2 stabilised Er^{3+} doped fibre laser at 1578 nm". 14th European Time and Frequency Forum, Torino, 14-16 March, (2000).

H. Simonsen, J. Henningsen and S. Søgaard: "DFB fibre lasers as optical wavelength standards in the 1.5 μm region". CPEM 2000: IEEE Transactions on Instrumentation and Measurement **50**, 482–486 (2000).

S. Søgaard, J. Henningsen and J.E. Pedersen: "Wavelength modulation of fibre lasers - a direct comparison with semiconductor DFB lasers and extended cavity lasers". Optical Fiber Sensors OFS2000, SPIE **4185**, 436–439 (2000).

S. Søgaard, M. Kristensen and J. Rathje: "Characterization of a long-period grating (LPG) bend sensor in a core concentricity error fiber". Proceeding to conference on Bragg grating, photosensitivity and poling in glass waveguides. ISBN 1-55752-680-X, BThC4–1(2001).

S. Søgaard and J. Henningsen: "Fibre laser modulation by integrated thin film resistive heating". Optical Fiber Measurement Conference (OFMC). ISBN 0 946754 40 3, 251–254 (2001).

S. Søgaard and J. Henningsen: "Thermal tuning and modulation of a DFB fibre laser with a thin-film heater". Applied Physics B **75**, 497–501 (2002).

Some of the work has also been presented at meetings in the Danish optical society and the Danish physical society.

S. Søgaard and J. Henningsen: "Thermal Modulation of a DFB Fibre Laser". Danish Optical Society meeting, 23-24 november-2001.

S. Søgaard and J. Henningsen: "The DFB fibre laser - a novel tool for spectroscopy". Meeting in the danish physical society, 30-31 may-2002.

Bibliography

[1] A.M. Vengsarkar, P.J. Lemaire, V. Bhatia, T. Erdogan and J.E. Sipe: "Long-period fiber gratings as band-rejection filters". J. Light. Tech. **14**, 58 (1996).

[2] V. Bathia, M.K. Burford and K.A. Murphy: "Long-period fiber grating sensors". OFC′96 Technical Digest pages ThP1,265–266 (1996).

[3] H.J. Patrick, C.C.Chang and S.T.Vohra: "Long-period fibre gratings for structure bend sensing". Electronic Letters **34**, 1773–1775 (1998).

[4] H.J. Patrick and S.T.Vohra: "Directional shape sensing using sensitivity of long period gibre gratings". OFS-13, SPIE **3746**, 561–564 (1999).

[5] S.W. James, C.C.Ye, S.Khaliq and R.P. Tatam: "Bending sensing using optical fibre long period gratings". SPIE **4185**, P1–08, 66–69 (2000).

[6] Y. Liu, L.Zhang and I. Bennion: "Bending curvature sensing based on measurement of resonance mode splitting of long-period fibre grating". SPIE **4185**, P2–44, 560–563 (2000).

[7] J. Rathje, M. Kristensen and J.Hübner: "Effects of core concentricity error on bend direction asymmetry for long-period fiber gratings". Conference Proceeding, Bragg Gratings, Photosensitivity, and Poling in Glass Waveguides, OSA Technical Digest Series pages 283–285 (1999).

[8] H.J. Patrick: "Self-aligning, bipolar bend transducer based on long period grating written in eccentric core fiber". Conference proceeding, OFS 2000 - 14th International Conference on Optical Fiber Sensors **Proc. SPIE 4185**, 17–20 (2000).

[9] J-N.Jang, S.Y.Kim, S.-W. Kim and M-S.Kim: "Temperature insensitive long-period fibre gratings". Electronics letters **35**, 2134–2136 (1999).

[10] V. Bathia, D.K.Campbell, D.Dherr, T.G.D′Alberto, G.A.T.Eych, K.A.Murphy and R.O.Claus: "Temperature-insensitive and strain-insensitive long-period fiber grating sensors for smart structures". Optical Engineering **37**, 1872–1875 (1997).

[11] C-C.Yang and C-H.Hsia: "A low-cost temperature sensor based on long period fiber gratings with linear wavelength transmission characteristics". SPIE **3420**, 221–235 (1998).

[12] W. Zhao and R.O. Claus: "Long-period grating fiber sensor with fiber Bragg grating demodulation". SPIE **3330**, 231–236 (1998).

[13] R.W.Fallon, L.Zhang, L.A.Everall, J.A.R.Williams and I.Bennion: "All-fibre optical sensing system:Bragg grating sensor interrogated by a long-period grating". Measurement Science and Technology **9**, 1969–1973 (1998).

[14] H.J. Patrick and S.T.Vohra: "Fiber Bragg grating with long period fiber grating superstructure for simultaneous strain and temperature measurement". SPIE **3483**, 264–267 (1998).

[15] B.A.L. Gwandu, X.W.Shu, Y.Liu, W.Zhang, , L.Zhang and I.Bennion: "Simultaneous measurement of strain and curvature using superstructure fibre Bragg gratings". Sensors and Actuators A **96**, 133–139 (2002).

[16] B-O.Guan, H-Y.Tam, X-M.Tao and X-Y.Dong: "Simultaneous strain and temperature measurements using a superstructure fibre Bragg grating". IEEE Photonics Technology Letters **12**, 675–677 (2000).

[17] K.Iwatsuki, H.Okamura and M.Satuwatari: "Wavelength tunable single-frequency and single polarisation Er-doped fiber ring-laser with 1.4 khz linewidth". Electronic Letters **22**, 2033–2035 (1990).

[18] N.Park, J.W.Dawson, K.J.Vahala and C.Miller: "All fiber, low threshold tunable single-frequency, erbium-doped fiber ring laser with a tandem Fabry-Perot filter". Appl. Phys. Lett. **59**, 420–422 (1991).

[19] F.J.McAleavey, J.O′Gorman, J.F.Donegan, B.D.MacCraith, J.Hegarty and G.Mazé : "Narrow linewidth, tunable Tm^{3+}-doped fluoride fiber laser for optical -based hydrocarbon gas sensing".

IEEE Journal of selected topics in quantum electronics **3**, 1103–1111 (1997).

[20] G.A.Ball and W.W.Morey: "Continuously tunable single-mode erbium fiber laser". Optics Letters **17**, 420–2 (1992).

[21] S.V.Chernikov, J.R.Raylor and R.Kashyap: "Coupled-cavity erbium fiber lasers incorporating fiber grating reflectors". Optics letters **18**, 2023–2025 (1993).

[22] J.T. Kringlebotn, P.R.Morkel, L.Reekie, J.-L.Archambault and D.N.Payne: "Efficient diode-pumped single-frequency erbium:ytterbium fiber laser". IEEE Photonics Technology Letters **5**, 1162–1164 (1993).

[23] M.Sejka, P.Varming, J. Hübner and M.Kristensen: "Distributed feedback Er^{3+}-doped fibre laser". Electronics letters **31**, 1445–1446 (1995).

[24] W.H.Loh, R.I.Laming and : "1.55 μm phase-shifted distributed feedback fiber laser". Electronics Letters **31**, 1440–1442 (1995).

[25] J.T. Kringlebotn, J.-L.Archmabault, L.Reekie and D.N.Payne: "Er^{3+}:Yb^{3+}- codoped fiber distributed-feedback laser". Optics Letters **19**, 2101–2103 (1994).

[26] L.Dong, W.H.Loh, J.E.Caplen, J.D.Minelly, K.Hsu and L.Reekie: "Efficient singel-frequency fiber lasers with novel photosensitive Er/Yb optical fibers". Optics letters **22**, 694–696 (1997).

[27] L.Dong, W.H.Loh, J.E.Caplen, K.Hsu, J.D.Minelly and L.Reekie: "Photosensitive Er/Yb optical fibers for efficient single-frequency fiber lasers". OFC′97 Technical Digest pages TuH2, 29–30 (1997).

[28] O. Hadeler, E. Rønnekleiv and R. I. Laming: "Polarimetric distributed feedback fibre laser sensor for simultaneous strain and temperature measurements". Applied optics **38**, 1953–1958 (1999).

[29] J.T. Kringlebotn, W.H.Loh and R.I.Laming: "Polarimetric Er^{3+} - doped fiber distributed-feedback laser sensor for differential pressure and force measurements". Optics Letters **21**, 1869–1871 (1996).

[30] S.W. Løvseth, J.T. Kringlebotn, E. Rønnekleiv and K.Bløtekjær: "Fiber distibuted-feedback lasers used as acoustic sensors in air". Applied Optics **38**, 4821–4830 (1999).

[31] P. Varming. *Optical Fiber Lasers.* PhD thesis Technical University of Denmark. COM 1997.

[32] M.Sejka, J. Hübner, P.Varming, M.Nissov and M.Kristensen: "Fiber distributed feedback lasers for high speed wavelength division multiplexed networks". OFC′96 Technical Digest page TuJ2 (1996).

[33] E.T. Wetjen, D.M. Sonnenfroh, M.G. Allen and T.F. Morse: "Demonstration of a rapidly tuned Er^{3+}-doped fiber laser for sensitive gas detection". Applied Optics **38**, 3370–3375 (1999).

[34] G.A.Ball and W.W.Morey: "Compression-tuned single-frequency Bragg grating fiber laser". Optics Letters **19**, 1979–1981 (1994).

[35] J.J. Pan, Y.Shi and T.Zhu: "Continuously tunable high power fiber lasers with 11 nm tunability". www.e-tek.com/products/whitepaters/ofc99/ofc99.html.

[36] H.G.Limberger, N.H.Ky, D.M.Costantini, R.P.Salath, C.A.P.Muller and G.R.Fox: "Efficient miniature fibre-optic tunable filter based on intracore Bragg grating and electrically resistive coating". IEEE Photonics Technology Letters **10**, 361–363 (1998).

[37] H. Simonsen, J.Henningsen and S. Søgaard: "DFB fiber lasers as optical wavelength standards in the 1.5 μm region". Transactions on Instrumentation and Measurement **50**, 482–485 (2001).

[38] D. P. Hand and P. St.J. Russell: "Photoinduced refractive-index change in germanosilicate fibers". Optics letters **15**, 102–104 (1990).

[39] M.Kristensen: "Ultraviolet-light-induced processes in germanium-doped silica". Physical review B **64**, 144201–12 (2001).

[40] B. Poumellec, I. Riant, P. Niay, P. Bernage and J. F. Bayon: "UV induced densification during Bragg grating inscription in Ge:SiO_2 performs: Interferometric microscopy investigation". Optical Materials **4**, 404–409 (1995).

[41] P.J.Lemaire, R.M.Atkins, V.Mizarahi and W.A.Reeds: "High-pressure H_2 loading as a technique for achieving ultrahigh UV photosensitivity and thermal sensitivity in GeO_2 doped optical fibres". Electronics Letters **29**, 1192–1193 (1993).

[42] V.Mizrahi, P.J.Lemaire, T.Erdogan, W.A.Reed and D.J.DiGiovanni: "Ultraviolet laser fabrication of ultrastrong optical fiber gratings and

of germania-doped channel waveguides". Applied Physics Letters **63**, 1727–1729 (1993).

[43] R.M. Atkins, V. Mizrahi and T. Erdogan: "248-nm induced vacuum uv spectral changes in opticla fibre preform cores: Support for a colour center model of photosencitivity". Electronic Letters **29**, 385–387 (1993).

[44] G. Meltz, W.W. Morey and W.H. Glenn: "Formation of bragg gratings in optical fibers by a transverse holographic method". Optics Letters **14**, 823–825 (1989).

[45] J. Hübner. *Index engeneering with excimer light.* PhD thesis Technical University of Denmark. MIC 1998.

[46] G. Meltz and W.W. Morey: "Bragg grating formation and germanosilicate fiber photosensitivity". SPIE **1516**, 185–199 (1991).

[47] H. Limberger, D. Varelas, R.P. Slatahe and G. Kotrotsios: "Mechanical degradation of optical fibers induced by uv light". SPIE **2841**, 84–93 (1996).

[48] H.Kogelnik: "Filter response of nonuniform almost periodic structures". The Bell System Technical J. **55**, 109–126 (1976).

[49] T. Erdogan: "Fibre grating spectra". Journal of lightwave technology **15**, 1277–1294 (1997).

[50] J. Rathje. *Thermal stability and practical applications of UV induced index changes in silica glasses.* PhD thesis Technical University of Denmark. 2000.

[51] T. Erdogan: "Cladding-mode resonances in short- and long-period fiber grating filters". J. Opt. Soc. Amer. A **14**, 1760–1773 (1997).

[52] M. Ibsen, J. Hübner, J.E. Pedersen, R. Kromann, L.-U. A. Andersen and M.Kristensen: "30 db sampled gratings in germanosilicate planar waveguides". Electronic Letters **32**, 2233–2235 (1996).

[53] G.A.Ball, W.W.Morey and W.H.Glenn: "Standing wave monomode erbium fiber laser". IEEE Photonics Technology Letters **3**, 613–615 (1991).

[54] E. Desurvire : *Erbium doped Fiber Amplifiers, principles and Applications.* John Wiley & Sons Inc. (1994).

[55] V.V.Steblina, J.D.Love, R.H.Stolen and J.-S.Wang: "Cladding mode degeneracy in bent w-fibres beyond cuttoff". Optics Communications **156**, 271 (1998).

[56] Dubbel, W.Beitz and H.K.Grote: *Taschenbuch für den Maschinenbau.* Springer Verlag 19 edition (1997). Pages= A20 and C20.

[57] J. Michael Hollas: *Modern Spectroscopy.* Wiley 3.rd edition (1996). ISBN = 0-471-96523-5.

[58] M. Kusaba and J. Henningsen: "The $\nu_1+\nu_3$ and the $\nu_1+\nu_2+\nu_4^1+\nu_5^{-1}$ combination bands of $^{13}C_2H_2$. Linestrengths, broadening parameters and pressure shifts". Journal of Molecular Spectroscopy **209**, 216–227 (2001).

[59] W. Demtröder: *Laser Spectroscopy. Basic consepts and instrumentation.* Springer 2.nd edition (1996).

[60] F.L. Walls and D.W.Allan: "Measurements of frequency stability". Proc. IEEE **74**, 162–168 (1986).

[61] J. Henningsen and H.Simonsen: "The (22^01-00^00) band of CO_2 at 6348 cm^{-1}. Line strengths, broadening parameters and pressure shifts". Journal of Molecular Spectroscopy **203**, 16–27 (2000).

[62] J. Henningsen and H.Simonsen: "Quantitative wavelength-modulation spectroscopy without certified gas mixtures". Applied Physics B **70**, 627–633 (2000).

[63] Optical interfaces for multichannel systems with optical amplifiers. International Telecommunication Union, ITU-T Recommendation G.692 oct. 1998.

[64] B. J. Eggleton , J. A. Pogers and P. Kuo: "Temperature stabilised operation of tunable fibre grating devices that use distributed on fibre thin film heaters". Conference on Optical, Fiber Communication, Technical Digest Series, IEEE, C pages 115–117 (2000).

[65] A. K. Ahuja, P. E. Steinvurzel, B. J. Eggleton and J. A. Rogers: "Tunable single phase-shifted and superstructure gratings using microfabricated on-fiber thin film heaters". Optics Communications **184**, 119–125 (2000).

[66] J. A. Rogers, B. J. Eggleton, J. R. Pedrazzani and T. A. Strasser: "Distributed on-fiber thin film heaters for bragg gratings with adjustable chirp". Applied Physics Letters **74**, 3131–3 (1999).

[67] S.Søgaard and J.Henningsen: "Fibre laser modulation by integrated thin film resistive heating". Optical Fibre Measurement Conference Proceedings pages 251–254 (2001).

[68] J. A. Rogers, P. Kuo, A. Ahuja, B. J. Eggleton and R. J. Jackman: "Characteristics of heat flow in optical fibre devices that use intergrated thin-film heaters". Applied Optics **39**, 5109–5116 (2000).

[69] T. R. Salamon, J. A. Rogers and B. J. Eggleton: "Analysis of heat flow in optical fiber devices that use microfabricated thin film heaters". Sensors and Actuators A **95**, 8–16 (2001).

[70] M. N. Őzisik: *Heat Transfer: a Basic Approach.* McGraw-Hill, New York (1985).

[71] H. S. Carslaw and J. C. Jaeger: *Conduction of Heat in Solids. 2nd edition, C.* Oxford U. Press, London (1959).